Voltage effects in poly and single-crystal 3*d* ferromagnetic metal/MgO systems AMIT KUMAR SHUKLA SEPTEMBER 2018

Voltage effects in poly and single-crystal 3*d* ferromagnetic metal/MgO systems

AMIT KUMAR SHUKLA

SEPTEMBER 2018

Voltage effects in poly and single-crystal 3*d* ferromagnetic metal/MgO systems

A dissertation submitted to

The GRADUATE SCHOOL OF ENGINEERING SCIENCE

OSAKA UNIVERSITY

in partial fulfillment of the requirements for the degree of

DOCTOR OF PHILOSOPHY IN SCIENCE

BY

AMIT KUMAR SHUKLA

SEPTEMBER 2018

ABSTRACT

Spintronics is a rapidly emerging and immensely promising research field. It enables us to develop future technology devices by exploiting the spin of the electron. A MgO-based magnetic tunnel junction (MTJ) is of great interest as a non-volatile memory because of their application in magnetic random memories and a magnetic sensor. Different successful approaches have been used to control the magnetization of MTJ, such as a current induced magnetic field and spin transfer torque. Although, these techniques still require Joule heating that remains too large to ignore. Voltage control of magnetization direction can expect a further reduction in power consumption in MTJ. The external voltage across ferromagnetic and MgO layers controls the interfacial magnetic anisotropy of the ferromagnetic material called a voltage-controlled magnetic anisotropy (VCMA). Althouthough, VCMA effect is observed on the different ferromagnetic material, yet we have observed voltage effect in poly and single-crystal 3*d* ferromagnetic metal/MgO systems using different measurement technique.

I studied the dependence of VCMA on post-annealing temperatures on (1) poly deposited Ta/CoFeB/MgO/CoFeB system using static magnetoresistance measurement and (2) VCMA and voltage-controlled Dzyaloshinskii–Moriya Interaction (VCDMI) at single-crystal $Fe_{1-x}Co_x$/Pd/MgO interface using magneto-static surface spin wave

Chapter 2 describes the estimation of the VCMA using magneto-static measurement. Here, I derive the anisotropy energy and voltage controlled magnetic anisotropy energy from magneto-static resistance at a different applied voltage

In chapter 3, I investigate VCMA on post-annealing temperatures on poly deposited different annealing temperatures, Ta(5 nm)/Ru(20 nm)/Ta(5 nm)/CoFeB(1.1 nm)/MgO(1.9 nm)/CoFeB(5 nm)/Ta(5 nm)/Ru(5 nm) layers were deposited on a Si/SiO_2 substrate in a magnetron sputter system and an MTJ was fabricated in hexagonal shape with conventional microfabrication technique. Samples have been annealed at different temperatures after microfabrication: 200 $^{\circ}$C, 250 $^{\circ}$C, 300 $^{\circ}$C, 350 $^{\circ}$C for 1 hour. Tunnel magnetoresistance (TMR) measurements were carried out using a conventional two-terminal technique under an in-plane magnetic field. VCMA has been characterized by bias-voltage dependence under a perpendicular magnetic field. Voltage controlled magnetic anisotropy and TMR in magnetic tunnel junctions with different annealing temperature have been investigated. We found that TMR and VCMA are increasing with

increasing post-annealing temperature from 200 ˚C to 300 ˚C and resistance of the MTJ layer is decreasing with increasing post-annealing temperature. Maximum VCMA and TMR of Ta/ CoFeB/ MgO sample are achieved 33fJ/Vm and 62%, respectively at 300 ˚C annealed sample.

Chapter 4 describes the dynamics of spin waves. By applying magnetic field normal to the spin-wave propagation direction, I excited magnetostatic surface spin waves. I derive a dispersion relation of MSSW from the basic electromagnetics and Landau-Lifshitz equation. I drive the resonance frequency; a voltage-controlled magnetic anisotropy and voltage-controlled interfacial Dzyaloshinskii-Moriya interaction relation with resonant frequency shifting by the applied voltage.

In chapter 5,6, I investigate VCMA and VCDMI at $Fe_{1-x}Co_x$/Pd/MgO interface, we grow single-crystal 3d ferromagnetic metal/MgO epitaxial multilayers of MgO (5 nm)/V (20 nm)/Fe (20 nm)/$Fe_{1-x}Co_x$ (0.3 nm)/Pd (0.2 nm)/MgO (5 nm) were deposited on a fcc-MgO(001) substrate using electron beam deposition under ultrahigh vacuum. An ultrathin $Fe_{1-x}Co_x$ layer was prepared by alternately depositing Fe and Co onto the bcc-Fe (001) layer**.** The surface crystal structure of $Fe_{1-x}Co_x$ was characterized *in situ* by reflection high-energy electron diffraction (RHEED) and similar patterns were obtained for all three regions (i.e., x = 0, 0.5, 1). Subsequently, 50-nm-SiO_2 was added as an additional insulating layer by sputtering. The scanning transmission electron microscopy (STEM) and EDS energy-dispersive spectroscopy analysis of the sample have been done. The film was patterned into 100 × 400 μm^2 rectangles. The longer edge of the rectangle is parallel to both Fe [100] and MgO [110] directions. Micro-sized antennas and an intermediate gate were fabricated with Cr (5 nm)/Au (200 nm) by a conventional microfabrication technique using electron beam lithography. We study the spin-wave property by measuring the scattering (S) parameter by a vector network analyzer by applying a dc voltage to the sample. Spin-wave spectroscopy has studied the influence of ultrathin $Fe_{1-x}Co_x$/Pd insertion between Fe and MgO interface on the interfacial magnetic anisotropy and its voltage-induced change. We found that the origin of VCMA and the origin of the interfacial anisotropy are not the same. First-principles calculations would be helpful to study the origin of the observed behavior.

Table of content

1 Introduction

A tremendous progress has been made in memory technology in complementary metal-oxide-semiconductor (CMOS) industry from last few decades. The smallest basic unit of CMOS memory is a transistor that was developed in late 1950 in Bell laboratory. In transistor (Field Effect Transistor), the electrical charge is flowing in a channel between two electrodes because of the potential difference between them. The conductance (resistance) of the channel can be controlled by a third terminal (Gate). The co-founder of Intel Gordon E. Moore observed a trend that the number of transistors built on a wafer would double in every eighteen months. It was called Moore's law. The density of CMOS memory (such as static random access memory (SRAM), dynamic random access memory (DRAM), NOR-flash memory and NAND-flash memory) is increasing with Moore's law as shown in Fig. 1.1.

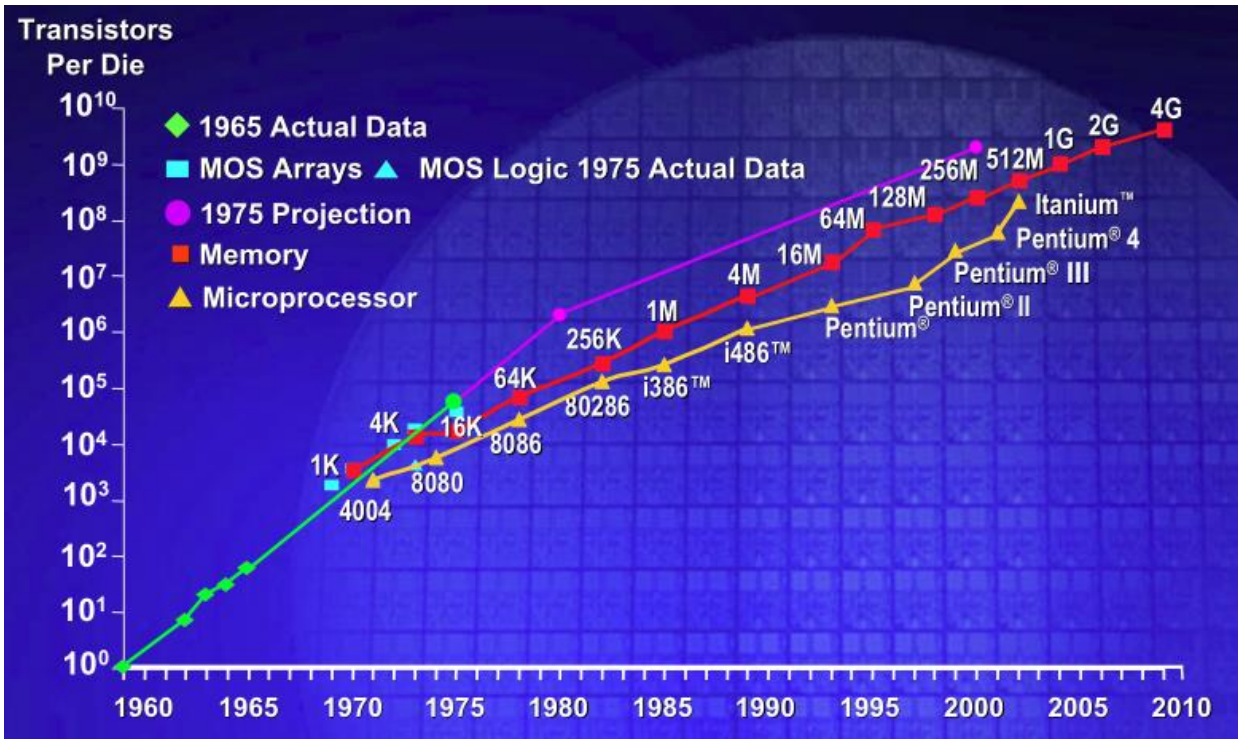

Figure 1.1. Moore's law for memory chips plotted on a semi-logarithmic scale.
(The purple curve is the Moore projection based on data up to 1975 [Source: Intel Corporation])

This scaling in dimension goes with additional benefits like high speed, low cost, more functionalities per memory unit, etc. However, as the size of the transistor is reduced, serious

problems like increased power consumption and loss of gate control arise. Now furthermore reduction in CMOS device size is very difficult. For more density and low power application, spintronics provides a powerful solution for memory application in recent year.

In CMOS, the charge of an electron plays a very crucial role. The electron has another fundamental property, i.e. called as Spin. It is a form of angular momentum carried by an electron. In 1988, a large change in conductance (resistance) was measured in the ferromagnetic material (FM) / non-ferromagnetic material / ferromagnetic material stack under a magnetic field. It was called giant magnetoresistance (GMR) [1,2]. The discovery of GMR further boosted this field of spintronics. Another spintronics device, magnetic tunnel junction (MTJ) [3,4,5,6] has the potential to replace the conventional CMOS memory. Nowadays, MTJ based magnetic random access memory (MRAM) is used as a memory unit.

1.1 Background

Sir J. J. Thomson discovered a subatomic particle electron in 1897. It acquires a specific mass and charge. The flow of electron generates an electric current in metal and semiconductors. The electrical charge is flowing in a channel between two electrodes (cathode and anode) in devices because of potential difference. The control of an electron (hole) charge flow between the electrode (Source and Drain) and it is controlled by an external voltage at a third terminal (Gate), is field effect transistor (FET). It is a basic unit of integrated industry and CMOS memory unit.

Two consecutive observations appeared in 1920 that shows that electron has another intrinsic property such as charge. These observations were:

1) The Stern - Gerlach experiment demonstrated when a single beam of the silver atom was passing through an inhomogeneous magnetic field, it was spat into two beams. It indicates the quantization of spatial orientation of angular momentum. This observation revealed that the electron has intrinsic angular momentum other that its change. It was known as electron spin. There is two kinds of angular momentum of an electron in an atom: Orbital angular momentum (L) and Spin angular momentum (S).

2) The hydrogen atom fine structure: a high-resolution system showed a double line spectrum in place of one spectrum. It is explained as Interaction of spin and orbital angular momentum (SOI) splits the hydrogen atom spectrum.

The Stern - Gerlach experiment indicates that electron spin is quantized as spin-up (+1/2) and spin down (−1/2). A golden time started in physics and microelectronics industry after evaluation of another intrinsic property (Spin). These investigations show a way to use of the spin intrinsic property with charge, for the realization of new era devices. The present conventional microelectronics devices are based on the charge of the electron in integrated circuits. Figure 1.1 indicates that Moore's law has almost reached its saturation point. It indicates that it would be too difficult to reduce the size of conventional devices. Therefore, we are looking for some alternative to the existing semiconductor technology which could be used for beyond Moore's device. Certain research and development are going on in the world such as silicon heterostructure, FinFET, III-V devices (GaN), carbon nanotubes and spintronics, etc. Spintronics is a spin-based electronics which utilize its spin property. It adds magnetism features (spin-based property). Spintronics devices may offer multi-functionality such as data storage device, sensors and spin oscillators, etc. In spintronics devices, we can utilize the electron's spin in various kind of memory applications similar to electron's charge in conventional devices.

1) The data are stored in binary bit by positive charge or negative charge in conventional electronics devices. Similarly, the data can be stored in binary bit by up spin or down spin in spintronics devices.

2) The flow of charge carries the information in conventional electronics (transistor). Similarly, the flow of spin can also carry information.

3) There is one interesting property in ferromagnetic material that when we apply the magnetic field in a certain direction, the ferromagnetic material's spin has aligned in that direction. However, we remove the magnetic field ferromagnetic material contains few spin still aligned in that direction. This remittance aligned spin can be used as a non-volatile application. Memory does not need the power to retain its data.

The evolution of spintronics memory field is started around 1980 when the field of spintronics devices merged with conventional devices. Some of the pioneering works in this direction are listed as below:

a) 1975: Magnetic Tunnel Junctions [3],
b) 1982: Electron tunneling in ferromagnetic films [7],

c) 1985: Spin injection phenomenon in a nonmagnetic (NM) metal from a ferromagnetic (FM) metal [8],
d) 1988: Giant magnetoresistance phenomenon was discovered independently by A. Fert [1] and Peter Gurnberg [2]
e) 1990: Datta and Das proposed the use of the semiconductors for spintronics in a spin field-effect-transistor [9].

By using the spin property, we can also fabricate as spintronics sensor, spin oscillators, spin field effect transistor, spin light emitting diode, spin resonant tunneling diode, quantum computers and telecommunication [9-15]. In this, most important applications include nonvolatile memory device with higher density, faster reading, faster writing, lesser power consumption, better retention and endurance. Magnetoresistance devices such as GMR and MTJ are promising devices for memory application. MRAM and read-head sensors were realized in spintronics field.

1.2 Magnetoresistance (MR)

The basic principle of the magnetoresistance (MR) is the variation of resistivity (conductivity) of a ferromagnetic material (FM) in a magnetic field. There is a different kind of effects that can be called magnetoresistance: some occurs in bulk magnetic metals (anisotropic magnetoresistance) and geometrical magnetoresistance (Giant magnetoresistance and Tunnel magnetoresistance).

1.2.1 Anisotropic magnetoresistance (AMR)

An FM which resistance depends on the angle between electrical current and magnetization is called as the anisotropic magnetoresistance (AMR). W. Thomson discovered the phenomenon in 1857.

1.2.2 Giant magnetoresistance (GMR) in Spin Valve

A spin valve is a device where FM was separated by ultrathin nonmagnetic material as shown in Fig. 1.2. The upper FM easily changes its magnetization direction is called free layer and the lower FM is pinned in a certain direction, is called fixed layer. The resistance of spin valve is lesser when the magnetization of both FMs are parallel (parallel configuration) and the resistance of spin valve is larger when the magnetization of both FMs are antiparallel (antiparallel configuration). The magnetoresistance of spin valve is called as Giant magnetoresistance (GMR). The GMR depends on the angle between the magnetization direction of both ferromagnetic materials. First time in 1988, Albert Fert and Peter Gurnberg [1,2] observed GMR in Fe/Cr/Fe sample as shown in Fig. 1.3. They were awarded jointly with the Nobel prize in Physics area in 2005.

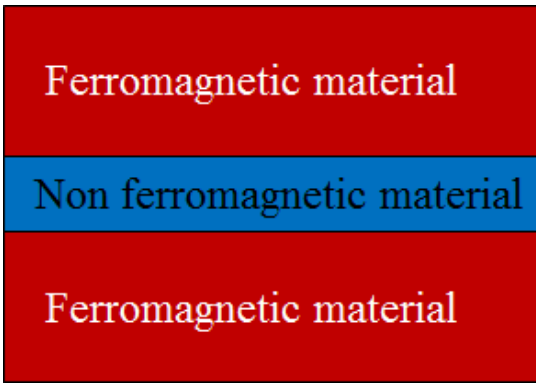

Figure 1.2 Schematic of GMR.

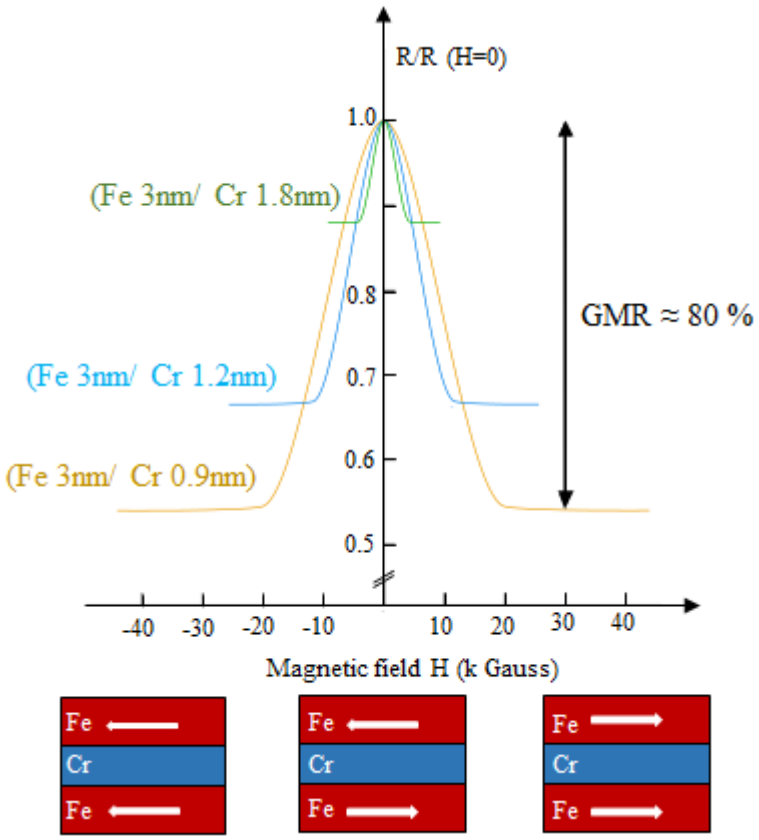

Figure 1.3. GMR: Result of Albert Fert and Peter Grunberg in 1988

GMR depends on the magnetization direction of FM. Magnetization depends on the density of state of *d*-band electron around Fermi level. In FM, the density of state of spin-up (+1/2) and spin down (−1/2) is different at Fermi energy level. Higher (lower) spin density at Fermi level is known as majority (minority) spin. Resistance (conductance) of spin-up (+1/2) and spin down (−1/2) electrons are modeled as resistance (conductance) channel in a ferromagnetic material Fig. 1.4. and Fig. 1.5 Let us assume that spin-up (+1/2) electron is in majority state and spin down (−1/2) are in minority state. (It can be reversed.) If the magnetization orientation in two FM layers is parallel in the spin valve, an electron from majority state with spin-up electrons of FM1 flow easily in majority state with spin-up of FM2 through spin-up the channel. Similarly, electron minority state with spin-down electrons of FM1 flow easily in minority state with spin-down of FM2 through spin down channel. However, an electron from a minority state with spin-down of FM1 is

strongly scattered in majority state with spin-up of FM2. Similarly, an electron from majority state with spin-down of FM1 is strongly scattered in minority state with spin-up of FM2.

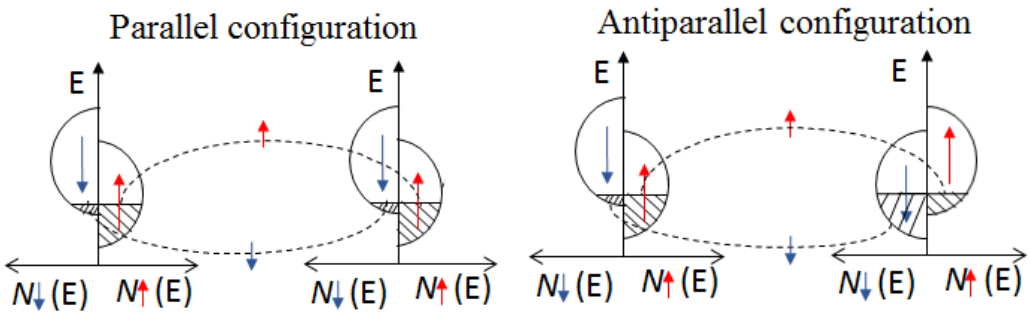

Figure 1.4. Schematic of ferromagnetic material in GMR: (a) Parallel configuration (b) Antiparallel configuration

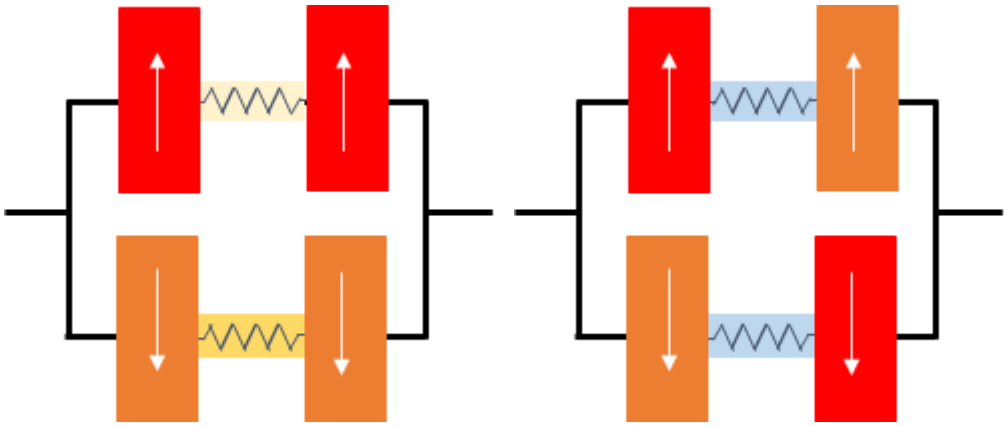

Figure 1.5. Schematic conductance of GMR (a) Parallel configuration (b) Antiparallel configuration

In this condition, the resistance of spin-valve is R_P. If the magnetization orientation in two FM layers is antiparallel in the spin valve, majority and minority carrier changes its magnetic orientation. The electron from majority state with spin-up electrons of FM1 flow easily in minority state with spin-up of FM2 through the spin-up the channel. Similarly, electron minority state with spin-down electrons of FM1 flow easily in majority state with spin-down of FM2 through spin down channel. However, an electron from a minority state with spin-down of FM1 is strongly scattered in minority state with spin-up of FM2. Similarly, an electron from majority state with

spin-up of FM1 is strongly scattered in majority state with spin-down of FM2. In this condition, the resistance of spin-valve is R_{AP}.

In the case of the parallel configuration, the majority of parallel electron travels easily hence resistance is small (conductivity is large). In the case of the anti-parallel configuration, the majority anti-parallel electron is scattered. Hence resistance is large (conductivity is small). Depending on the magnetic orientation of the ferromagnetic layers, the resistance is the device is varying.

Spin-dependent transport phenomena, GMR is defined as GMR= $(R_{AP}-R_P)/R_P$.

Maximum GMR in spin valve devices is reported up to 20%, that is not sufficient for most of the practical application. If we substitute the ultrathin nonmagnetic material in spin valve device with an insulator layer, the MR ratio of the device is increasing. This new device is called a magnetic tunnel junction (MTJ).

1.2.3 Tunnel magnetoresistance (TMR) in Magnetic tunnel junction (MTJ)

Similar to the spin valve-GMR device, an MTJ is having two FM layer separated by ultra-thin insulator (tunnel) barrier as shown in Fig. 1.6. Tunneling probability of electron through an insulator depends exponentially on its barrier thickness. Therefore, we select an ultrathin insulator barrier. The magnetoresistance of MTJ, i.e., TMR depends on the relative orientation of the magnetization of the magnetic layer, which can be changed by applying the external magnetic field. However, Julliere [1] observed first TMR on MTJ in 1975. Still, this research could not move faster because of fabricating ultrathin insulating barrier. The reported TMR ratio was very small, or it was almost zero at room temperature [16]. TMR up to 70% was achieved using Al_2O_3 as an insulator layer.

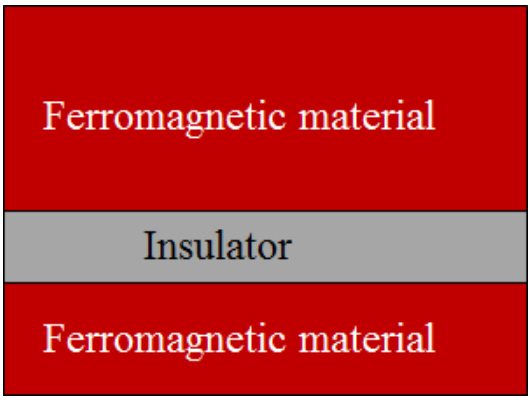

Figure 1.6 Magnetic tunnel junction (MTJ)

The initial investigations related to MTJ devices utilized amorphous Al_2O_3 as the tunnel barrier, which offered relatively smaller TMR ratios up to 70% at RT [4,5]. However, this TMR ratio was

not sufficient enough for most of the practical device applications. For the practical purpose of the memory application, larger TMR is required. Therefore, the research started to achieve larger TMR

Earlier researcher started to use the larger spin-polarized material to achieve it. Example: 100% spin-polarized CrO_2 was used as a ferromagnetic layer. Because of CrO_2 material's metastable nature, fabrication of MTJ was very difficult. After that, researchers started to look for another option.

1.3 MgO based magnetic tunnel junction

In 2001, theoretical physicist predicated to achieve 1000% TMR with crystalline MgO junction in epitaxially grown MTJ. Further in 2004, two groups independently reported the discovery of large TMR ratios up to 200% at room temperature with crystalline MgO barrier in epitaxially grown MTJ. It was a milestone in spintronics memory devices. A higher value of TMR would help for deep learning of spin-dependent tunneling through crystalline MgO barrier. Coherent tunneling of the electrons achieves it through crystalline MgO(001). A crystalline MgO(001) tunnel junction can be easily grown on a bcc Fe(001) FM layer. The lattice mismatch of MgO(001) and bcc Fe(001) FM layer is very less. [6]. Thus, Fe(001)/MgO(001)/Fe(001) MTJ was expected to have a high value of TMR. They would be useful for practical application of HDD read heads and high-density MRAM. Initially, Fe(001)/MgO(001)/Fe(001) MTJs were studied extensively [17,18], however the maximum achieved TMR was 30%. It was less than the maximum TMR value of amorphous Al_2O_3 junction (70%). The problem associated with this fabrication was that Fe was getting oxidized at MgO interface that scatters spin at the interface. However, in theoretical analysis coherent tunneling of spin was predicated. Scattering at the interface decreases the TMR of MTJ devices. For higher TMR, it was necessary to fabricate a better Fe/MgO. In 2004 two noticeable breakthroughs were reported by Yuasa and group [19] and Parkin and group [20]. Yussa and group grow epitaxial Fe(001)/MgO(001)/Fe(001) MTJs under ultra-high vacuum. They achieved a TMR valve of 188% at RT. It was quite larger than all previous TMR valve. Parkin and group grow epitaxial FeCo(001)/MgO(001)/FeCo(001) MTJs ultra-high vacuum. They achieved a TMR valve of 220% at RT. It was quite larger than all previous TMR value. Thus a well-controlled epitaxial deposition technique is mandatory for achieving high TMR ratios. TMR valve has been achieved ratios up to 1000% in MgO-based MTJs [21,22].

To overcome this epitaxial deposition related issue, a new CoFeB/MgO/CoFeB MTJ was sputtered by using the sputtering technique [23] in 2005. Transmission electron microscopy image revealed that CoFeB layers are amorphous and MgO is forming (001) polycrystalline texture [6].

When we anneal this structure the boron from CoFeB diffuses in Ta, and CoFeB forms polycrystalline structure at MgO interface. At annealing of 360 °C, TMR value of 230% at RT was achieved in this device. TMR value have been achieved ratios up to 1000% in CoFeB/MgO/CoFeB MTJs [22,24]. Post-annealing of MTJ and selection of the proper thickness of buffer layer influences the TMR value of the MTJ.

This MTJ structure CoFeB/MgO/CoFeB MTJs are fabricated by the sputtering fabrication technique at RT. After that, it is post annealed externally. This technique makes possible to fabricate MTJs on a large substrate. It is a favorable technique for industrial purpose.

1.4 Magnetization switching method

MTJ are promising devices for memory application. When the magnetization direction of both the FM in parallel or antiparallel direction, it can be considered as binary bit 0 or 1. For magnetic writing the data in MRAM, there are some successful magnetization approaches:

1-Electric-current based magnetization switching

a-current-induced magnetic field switching

b- spin-transfer torque induced switching

2- Voltage–controlled magnetization switching

1.4.1 Electric-current controlled magnetization switching

a-Current induced magnetic field switching

In MTJ, there are two FM layers as shown in Fig. 1.2. By apply external the current, we can induce the magnetic field as shown in Fig. 1.7(a). By changing the current direction, we can change the magnetic field direction. In this way, the magnetic domains in adjacent FM layers can be

manipulated controllably between stable parallel and antiparallel configurations by applying current pulses of the appropriate sign. It needs high power to change the magnetic bit. Therefore, it is not used nowadays in magnetic memory devices.

b-Spin-transfer torque induced switching

In MTJ, there are two FM layers as shown in Fig.1.6. One of the FM layers is usually thicker or made fixed by exchange bias so that it can be polarized in a certain direction with rest to another FM layer. It is known as a fixed layer. Other FM layer is considered as a free layer. In MTJ, the free layer changes the magnetization direction. Therefore, free layer magnetization direction can be parallel or antiparallel to fixed layer direction. When the electrons flow from the fixed layer, they are polarized in the fixed layer direction. If these electrons go in the free layer, they provide torque on free layer and rotate the magnetization in fixed layer direction, shown in Fig. 1.7(b). If electrons flow from free layer to fixed layer, they got scattered from fixed layer; they got magnetized in antiparallel to fixed layer. After that those electrons change the magnetization direction of the free layer in antiparallel to fixed layer. Therefore, by changing the direction of the current, we can switch the magnetization direction.

The first time, quantitative calculation of spin-transfer torque in GMR is given by Slonczewski [25] $\tau_{other} = g(\theta)\frac{\gamma\hbar \mathrm{I}}{\mathrm{e}V_{free}M_{s,free}}\mathrm{m}_{free}\times(\mathrm{m}_{free}\times\mathrm{m}_{fix})$

where, m_{free} and m_{fixed} is unit magnetization vector of the free FM layer and fixed FM layer. $g(\theta)$ is the spin transfer efficiency, I is the current and e is electron charge. V_{free} is the volume of the free FM layer and $\mathrm{M}_{s,free}$ is the saturation magnetization of the free FM layer. Now, there would be an additional term spin transfer torque in LLG equation

$$\frac{d}{dt}\mathrm{M} = -\gamma M\times\mathrm{H}_{eff} + \alpha\frac{M}{M_s}\times\frac{d}{dt}\mathrm{M} + g(\theta(\frac{\gamma\hbar \mathrm{I}}{\mathrm{e}V_{free}M_{s,free}}\mathrm{m}_{free}\times(\mathrm{m}_{free}\times\mathrm{m}_{fix})$$

This equation shows when electrons from the fixed layer to the free layer, they stabilize the free layer and this starts precession around the easy axis direction. Because of the damping parameter, it becomes parallel to fixed FM layer direction. Similarly, the opposite flow of electrons switches the free layer in an antiparallel direction.

Spin transfer torqued induced switching manipulates the magnetization direction of free FM layer in MTJ. It is a promising candidate for a magnetic memory writing. This technique reduces the writing power with respect to current induced magnetization induced switching. However, spin

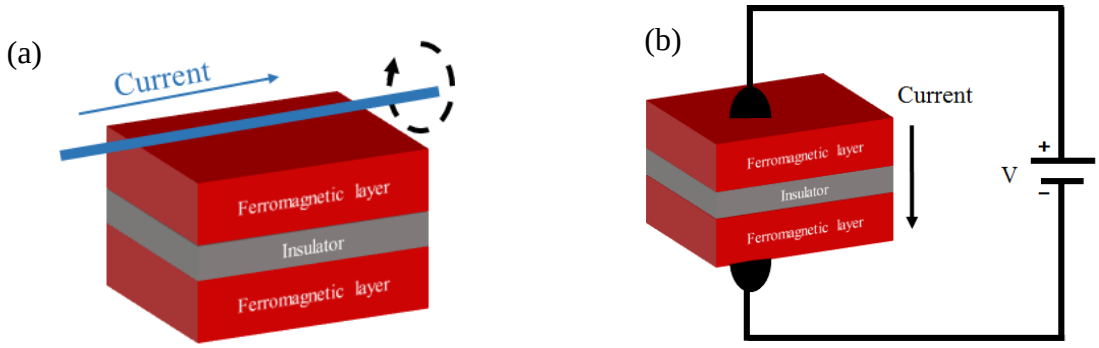

Figure 1.7 Schematic of electric current induced magnetization switching

(a) External magnetic field (b) Spin-current

transfer torque induced magnetization switching [25,26] still consumes higher energy than the stabilization energy for a single bit information. Therefore, voltage–controlled magnetization switching is expected as a promising and ideal method for future magnetic writing the data in MRAM.

1.4.2 Voltage–controlled magnetization switching

The perpendicular electric field on 3 *d* ferromagnetic material such as Fe, Co, Ni and their alloy, has been attracted great interest and exciting research by its physics and enormous potential in magnetization switching. In principle, the perpendicular electric field is screened by an accumulation of *d* band-electron at the interface of ferromagnetic materials as shown in Fig. 1.8. This modified interfacial *d* band electron changes the interfacial magnetic anisotropy. It is called a voltage –controlled magnetic anisotropy (VCMA).

First principle calculation originally expects this VCMA in FM. Nakamura [27] calculated the band dispersion by the applied electric field at an atomic layer of Fe/ MgO (001) interface. The $d_{x^2-y^2}$ and $d_{xy,yz}$ band cross the Fermi energy at around $\overline{\mathrm{M}}$. By applying the perpendicular electric

field, the d band electron density changes at Fermi level in $d_{x^2-x^2}$ and $d_{xy,yz}$ band. Since this modification in occupancy of d band electrons near Fermi level causes VCMA.

A pioneer work is done by Weisheit and group [28] in 2007. By applying an electric field, they reported coercively change in 4.5% in Pt(Pd)/FePt(FePd)/ liquid electrolyte. They used the high electric field at the FM interface, that is not good for practical application. After that in 2009, Our group showed a change in magnetization curvature under different applied voltage in Au/Fe/MgO junction [29]. They suggested that the origin of VCMA is a change of occupancy in 3*d* electron. They change orbital angular momentum. However, the interface condition of FM/MgO is controlled by hybridization, oxidation, interdiffusion and roughness, etc. Therefore, there are different theoretical and experimental studies have been observed. Still, we achieved VCMA in range of hundred fJ/V.m. Bawer and group [30] achieved >1000 fJ/V.m value of VCMA by magneto ionic control – oxidation state method. Here, applied voltage controls the oxidation state. It is the slow mechanism. It does not respond at a higher frequency. Therefore, it is not used for memory application. The microscopic origin of the VCMA effect at the interface of ferromagnetic materials can be understood as follows. In the case of 3*d*-ferromagnetic materials such as Co, it has been experimentally reported that electric-field-induced changes of the orbital magnetic moment predominantly contribute to the VCMA effect [31]. Moreover, in the case of 5*d*-materials with proximity-induced spin polarization, such as Pt, the magnetic dipole T_z term was reported to be significant in determining the VCMA effect [32]. This term corresponds to the electric quadrupole present in atoms. This study indicates that the occupancy of the interfacial *d*-band in a ferromagnetic material is correlated to the VCMA effect. However, to the best of our knowledge,

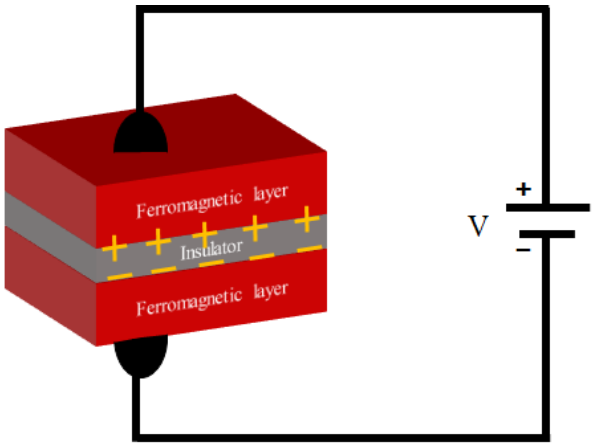

Figure 1.8 Voltage induced charge

the dependency of VCMA and interfacial anisotropy energy on the occupancy of *d*-band electron orbitals of ferromagnetic material has not been studied.

1.5 Dzyaloshinskii–Moriya Interaction

The Dzyaloshinskii−Moriya interaction (DMI) is induced because of the lack or breaking of inversion symmetry in lattices. The origin of DMI is in multiferroic oxides. The DMI is an antisymmetric exchange interaction which plays a decisive role in the formation of exotic magnetic structures. It appears in the absence of spatial inversion symmetry incorporating a spin-orbit interaction At ultrathin magnetic film; interfacial DMI have been predicted where two atomic the spins $\vec{S}_1$ and $\vec{S}_2$ with a neighboring atom having a large spin-orbit coupling. The voltage-induced magnetic property change, I was interested in an *interfacial* DMI.

Dzyaloshinskii−Moriya interaction (DMI) is described as,

$$\mathrm{E}_{\mathrm{DMI}} = (S_1^x, S_1^y, S_1^z)\begin{pmatrix} 0 & D^x & -D^y \\ -D^z & 0 & D^x \\ D^y & -D^x & 0 \end{pmatrix}\begin{pmatrix} S_1^x \\ S_1^y \\ S_1^z \end{pmatrix} = \vec{D}_{12}\cdot(\vec{S}_1 \times \vec{S}_2) \text{ ----------(2.24)}$$

where, $\vec{D}_{12}$ is the Dzyaloshinskii−Moriya vector. It is perpendicular to asymmetry direction and the vector $\vec{r}_{12}$ between the spins $\vec{S}_1$ and $\vec{S}_2$. The Dzyalsinskii−Moriya interaction (DMI) is induced because of the lack or breaking of inversion symmetry in lattices and at the interface of magnetic films, respectively For the ultrathin magnetic film, interfacial DMI have been predicted where two atomic the spins $\vec{S}_1$ and $\vec{S}_2$ with a neighboring atom having a large spin-orbit coupling.

1.6 Purpose of our study

From last one decade, magnetic tunnel junction (MTJ) [24,34] was the center of extensive studies. A MgO-based MTJ polycrystalline [22-24] and single-crystal [19,20] MTJ have 1000% because of coherent tunneling through a MgO(001) tunnel junction TMR ratio that is of great interest as a non-volatile. For magnetic writing the memory, different successful approaches have been used to control the magnetization of MTJ, such as current induced magnetic field and spin transfer torque [25,26]. These techniques require Joule heating that remain too large to ignore. Voltage control of

magnetization direction can expect a further reduction in power consumption in MTJ. The external voltage across ferromagnetic and MgO layers controls the interfacial magnetic anisotropy of the ferromagnetic material [27,28,29,35,36] Voltage controlled magnetization switching [37] in MTJ gives an impulse in low power nonvolatile memory technology.

The sputtering deposition method is an ideal technique for industrial purpose. When we anneal this structure the boron from CoFeB diffuses in Ta, and CoFeB forms polycrystalline structure at MgO interface. The coherent tunneling through Ta/CoFeB/MgO/CoFeB/Ta MTJ is changing because of the polycrystalline structure of CoFeB at MgO interface. It is changing with post-annealing temperature. At annealing of 360 °C, TMR value of 230% at RT was achieved in this device. TMR value have been achieved ratios up to 1000% in CoFeB/MgO/CoFeB MTJs [22-24]. Therefore, Ta/CoFeB/MgO/CoFeB/Ta MTJ is a good candidate for MRAM. The voltage induced magnetization is an ideal method in MRAM application. VCMA is an interfacial phenomenon. The TMR and VCMA of CoFeB/MgO/CoFeB are changing with annealing temperature. The dependence of VCMA on post-annealing temperatures on CoFeB/MgO with different buffers have been studied [38]. However, the dependence of VCMA on post-annealing temperatures on Ta/CoFeB/MgO/CoFeB system has not been clarified yet. Therefore, I studied VCMA on post-annealing temperatures on Ta/CoFeB/MgO/CoFeB system. In this way the first part of the dissertation, we studied “Voltage effects in poly 3*d* ferromagnetic metal/MgO systems”.

We need a high VCMA at a higher frequency for MRAM application. From the microscopic origin of the VCMA effect at the interface of ferromagnetic materials, it can be understood as the sum of (1) electric-field-induced changes of the orbital magnetic moment predominantly contribute to the VCMA effect [31]. (2) proximity-induced spin polarization the magnetic dipole T_z term. This study indicates that the occupancy of the interfacial *d*-band in a ferromagnetic material is correlated to the VCMA effect. By changing the chemical ordering, the ferromagnetic material, I can change the occupancy of *d* band electron and VCMA value. Best of our knowledge, the dependency of VCMA on the occupancy of *d*-band electron orbitals of ferromagnetic material has not been studied. Therefore, I studied dependency of VCMA on of *d*-band electron orbitals of a single crystalline FM/ MgO interface. In this way, the second part of my dissertation, I discussed on voltage effect on single crystal/ MgO interface.

2 Voltage-controlled magnetic anisotropy and its measurement method

2.1 Tunnel magnetoresistance (TMR) in magnetic tunnel junction (MTJ)

The current density through MTJ depends on the magnetization direction of both the ferromagnetic material. Under parallel configuration (both the FM layer are magnetized in the same direction), the current density is because of majority to majority and minority to minority band tunneling. It is defined as:

$$J_P = J_\uparrow + J_\downarrow = (G^{++} + G^{--})V = G_P V \text{ ----(2.1)}$$

G^{++} (G^{--}) is the conductance because of majority to majority (minority to minority) band tunneling. The G_P is the conductance of MTJ under parallel configuration.

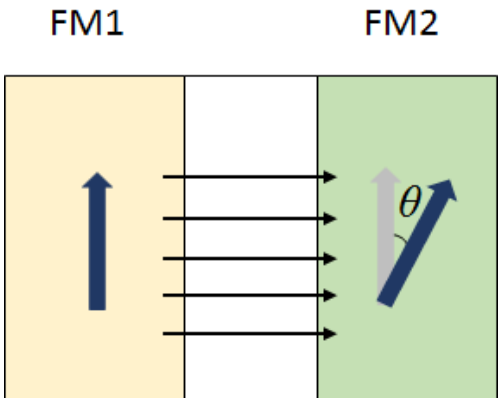

Figure 2.1. Conductance of MTJ. The arrow indicates the magnetization direction.

Similarly, the current density through MTJ under antiparallel configuration is because of majority to minority and minority to majority band tunneling. It is defined as:

$$J_{AP} = J_\uparrow + J_\downarrow = (G^{+-} + G^{-+})V = G_{AP} V \text{ ----(2.2)}$$

G^{+-} (G^{-+}) is the conductance of MTJ because of majority to minority (minority to majority) band tunneling. The G_{AP} is the conductance under antiparallel configuration.

From the above eq^n (2.1) and eq^n (2.2), when ferromagnetic films are magnetized at an angle θ as shown in Fig. 2.1., the current density through MTJ is defined as

$$J = \left[(G^{++} + G^{--}) \cos^2\left(\frac{\theta}{2}\right) + (G^{+-} + G^{-+}) \sin^2\left(\frac{\theta}{2}\right) \right] V \text{ ------(2.3)}$$

In this way, the majority of parallel electron travels easily, and hence the conductance is large in the parallel configuration. In the case of the anti-parallel configuration, the majority anti-parallel

electron is scattered, and hence conductance is small. Depending on the magnetic orientation of ferromagnetic layers, the conductance in the device is varying. The magneto-static conductance of MTJ $G(\theta), G(\theta) = \frac{1}{2}(G_P + G_{AP}) + \frac{1}{2}(G_P - G_{AP})\cos(\theta)$ ----(2.4)

The spin-dependent transport phenomena, tunnel magnetoresistance (TMR) of the magnetic tunnel junction (MTJ) is defined as TMR= (G_P−G_{AP})/ G_{AP}.

2.2 Estimation of anisotropy energy by measuring magneto-static resistance (conductance)

The anisotropy energy of the ferromagnetic material is measured by measuring the static resistance (conductance) of MTJ under magnetic field. The magneto-static conductance $G(\theta_{relative})$ (eq^n (2.4)) of MTJ is defined as $G(\theta_{relative}) = \frac{1}{2}(G_P + G_{AP}) + \frac{1}{2}(G_P - G_{AP})\cos(\theta_{relative})$ ------(2.5)

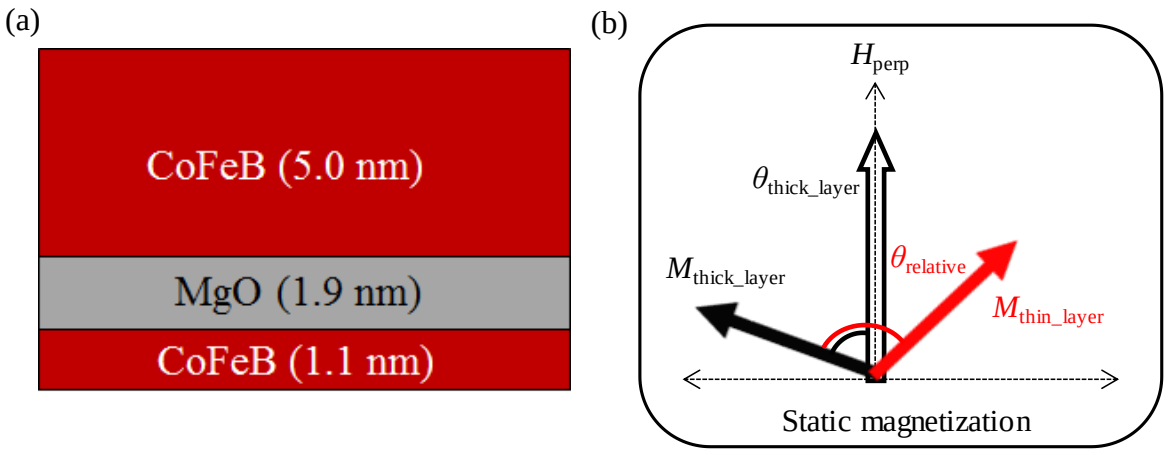

Figure 2.2. (a) The schematic of MTJ (b) Schematic of magnetization direction the 1.1-nm-CoFeB (M_{thin_layer}) and the 5-nm-CoFeB (M_{thick_layer}). The $\theta_{relative}$ is the angle between both magnetizations. The θ_{thick_layer} is the angle between the magnetization of the thick layer and perpendicular magnetic field (H_{perp}).

In this study, an MTJ with ferromagnetic materials thickness with 1.1-nm-CoFeB (thin ferromagnetic layer) and 5-nm-CoFeB(thick ferromagnetic layer) separated by 1.1nm-MgO is shown in Fig. 2.2(a). This MTJ is an elliptical shape and both FM layers are in in-plane direction

(experimentally, it is shown in next chapter). The magnetization of both ferromagnetic films ($M_{\text{thin\_layer}}$ and $M_{\text{thick\_layer}}$) are having the θ_{relative} angle between them as shown in Fig. 2.2(b). A perpendicular H_{perp} is applied perpendicular to the film surface. Under the perpendicular magnetic field (H_{perp}), the thick layer is forming $\theta_{\text{thick\_layer}}$ $\left(=\cos^{-1}\left(\frac{H_{\text{perp}}}{H_{\text{s,thick}}}\right)\right)$ from the perpendicular direction. Therefore, the magnetization of the thin layer is at ($\theta_{\text{relative}}-\theta_{\text{thick\_layer}}$) angle from the perpendicular direction.

The anisotropy energy of the system is defined as work done by an external source (H_{perp}) by changing the direction of magnetization of FM layers from an in-plane direction to a perpendicular-plane direction. The anisotropy energy per unit volume (E_{an}) is defined as:

$$E_{\text{an}} = -\int_0^{M_s} \vec{H}.d\vec{M} \text{ -------(2.6)}$$

Eq$^{\text{n}}$ (2.6) can be written as $E_{\text{an}} = -\int_0^{M_s} H_{\text{perp}} dM_{\text{perp}}$ ------(2.7)

where, M_{perp} and M_{s} are the perpendicular component of the magnetization and the saturation magnetization of the thin ferromagnetic material, respectively. By changing the variable, Eq$^{\text{n}}$ (2.7) can be written $E_{\text{an}} = -\int_0^{H_{\text{s,thin}}} \mu_0\left(1-\frac{M_{\text{perp}}}{M_{\text{s}}}\right) dH_{\text{perp}}$ -------(2.8)

$H_{\text{s,thin}}$ is the minimum perpendicular magnetic field where the magnetization of the thin layer becomes parallel to H_{perp}. From the schematic graph in Fig. 2.2(b), normalized perpendicular component, of a thin layer (M_{perp} / M_{s}) is estimated from ($\theta_{\text{relative}}-\theta_{\text{thick\_layer}}$).

$$\frac{M_{\text{perp}}}{M_{\text{S}}} = \cos\left(\theta_{\text{relative}} - \theta_{\text{thick\_layer}}\right) \text{------(2.9)}$$

From eq$^{\text{n}}$ (2.5) and $\theta_{\text{thick\_layer}}$, the $\frac{M_{\text{perp}}}{M_{\text{S}}} = \cos\left(\cos^{-1}\left(\frac{2G-\left(G_{\text{P}}+G_{\text{AP}}\right)}{\left(G_{\text{P}}-G_{\text{AP}}\right)}\right) - \cos^{-1}\left(\frac{H_{\text{perp}}}{H_{\text{s,thick}}}\right)\right)$ ------(2.10)

The MTJ is an elliptical shape. Its demagnetization field (H_d=$-M_s$ from supplementary, the eq$^{\text{n}}$ (34)) and lies in out of plane direction. Shape anisotropy energy is defined (from supplementary,

the eq^{n} 36) as $-\mu_0 M_s^{\,2}/2$ per unit volume and assume the easy axis lies in-plane direction. The uniaxial anisotropy energy per unit volume is defined as K_u. Because of symmetrical breaking, there is interfacial anisotropy energy at CoFeB/MgO interface. The interfacial anisotropy energy per unit area is K_s. Therefore, total magnetic anisotropy energy per unit area

$$E_{an} \times d = \left(-\frac{1}{2}\mu_0 M_s^{\,2} + K_u \right) d + K_s \text{ --------(2.11)}$$

where, d is the ultrathin FM thickness. (That is 1.1 nm in my research).

2.3 Estimation of voltage-controlled magnetic anisotropy energy from measuring magneto-static resistance (conductance)

Because of symmetrical breaking, there is a perpendicular magnetic anisotropy (PMA) energy at CoFeB/MgO interface. It is the interfacial property of the *d*-band electron of ferromagnetic material. The applied voltage across the MTJ applied a perpendicular electric field at the ferromagnetic material as shown in Fig.2.3. The perpendicular component of the electric field at ferromagnetic material changes the *d*-band electron density [28] in ferromagnetic material. The changed the *d*-band electron changes the magnetic property such as conductance of MTJ and PMA [28-29] of the ferromagnetic material. The perpendicular component of the electric field changes the PMA of the ultrathin ferromagnetic material interface is called voltage-controlled magnetic anisotropy (VCMA) change.

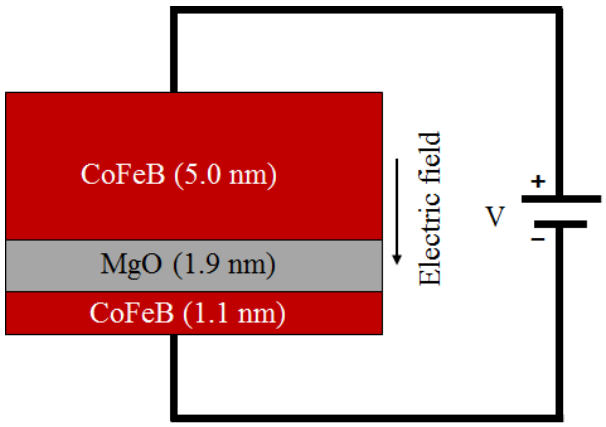

Figure 2.3. Voltage across the MTJ

The conductance of MTJ is:

$$G(\theta_{relative}, V) = \frac{1}{2}\left(G_P(V) + G_{AP}(V)\right) + \frac{1}{2}\left(G_P(V) - G_{AP}(V)\right)\cos(\theta_{relative}) \text{ ----(2.12)}$$

The conductance of MTJ in parallel G_{P} (antiparallel G_{AP}) configuration is changing with applied voltage. The anisotropy energy under different voltage is defined as:

$$E_{\mathrm{an}}(V) = -\int_{0}^{H_{\mathrm{s,thin}}} \mu_0 \left(1 - \frac{M_{\mathrm{perp}}(V)}{M_{\mathrm{s}}}\right) dH_{\mathrm{perp}} \text{ -----(2.13)}$$

The resistance of MTJ (magneto-resistance) has been measured at different bias voltage at the perpendicular magnetic field. The normalized perpendicular component, of a thin layer ($M_{\mathrm{perp}} / M_{\mathrm{s}}$) is extracted from the magneto-resistance curve.

$$\frac{M_{\mathrm{perp}}(V)}{M_{\mathrm{S}}} = \cos\left(\cos^{-1}\left(\frac{2G(V) - \left(G_{\mathrm{P}}(V) + G_{\mathrm{AP}}(V)\right)}{\left(G_{\mathrm{P}}(V) - G_{\mathrm{AP}}(V)\right)}\right) - \cos^{-1}\left(\frac{H_{\mathrm{perp}}}{H_{\mathrm{s,thick}}}\right)\right) \text{-----(2.14)}$$

The magnetic anisotropy energy per unit area

$$E_{\mathrm{an}}(V) \times d = \left(-\frac{1}{2}\mu_0 M_{\mathrm{s}}{}^2 + K_{\mathrm{u}}\right) d + K_{\mathrm{s}} + \Delta K_{\mathrm{s}}(V) \text{ ------(2.15)}$$

$\Delta K_{\mathrm{s}}(V)$ is PMA change by applied perpendicular electric field. It is VCMA effect of MTJ.

3 Voltage-controlled magnetic anisotropy with different annealed Ta/CoFeB/MgO system

3.1 Introduction

From last one decade, magnetic tunnel junction (MTJ) [33,34] has been extensively studied. A MgO-based MTJ is of great interest as a non-volatile memory because of its application in magnetic random memory. Different successful approaches have been used to control the magnetization of MTJ, such as current induced magnetic field and spin transfer torque [25,26]. These techniques require Joule heating that remain too large to ignore. Voltage control of magnetization direction can expect a further reduction in power consumption in MTJ. External voltage across ferromagnetic and MgO layers controls the interfacial magnetic anisotropy of ferromagnetic material called voltage-controlled magnetic anisotropy (VCMA) [27,28,29,35,36]. Many different experimental trials have reported the voltage control of magnetic properties in several materials and stacking structures. These include multilayered stacks with piezoelectric materials [39,40], ferromagnetic semiconductors, [41] single-phase multiferroic materials [42,43], heterostructures consisting of artificial ferroelectric/ferromagnetic layers [44-47], transition of the magnetic state at metal surfaces [48], the Curie temperature [49,50] exchange bias [51], the Dzyaloshinskii–Moriya interaction [52] and the exchange interaction [53-55]. Most importantly, high-frequency magnetization switching has contributed to a new class of VCMA-driven MgO-based MTJ memory devices [56-59].

In one multilayer system, Ta/CoFeB/MgO, the CoFeB layer has a perpendicular anisotropy. It has been employed in MgO-based MTJs because of its high tunnel magnetoresistance (TMR) as well as VCMA. High TMR ratio can be obtained when the MgO barrier was sandwiched in between amorphous CoFeB ferromagnetic electrodes. Microstructures reveal that the MgO layer was textured in the (001) plane on an amorphous layer. At annealing temperature, the boron (B) diffuses in the Ta layer, and CoFeB forms a polycrystalline structure on MgO(001) plane [60]. The dependence of VCMA on post-annealing temperatures on CoFeB/MgO with different buffers have been studied [38]. However, the dependence of VCMA on post-annealing temperatures on Ta/CoFeB/MgO/CoFeB system has not been clarified yet.

3.2 Experiment section

3.2.1 The process flow of fabrication

In order to investigate VCMA with different annealing temperatures, an MTJ structure Ta (5 nm)/Ru (20 nm)/Ta (5 nm)/CoFeB (1.1 nm)/MgO (1.9 nm)/CoFeB (5 nm)/Ta (5 nm)/Ru (5 nm) was deposited on a Si/SiO_2 substrate in a magnetron sputter system with base pressure < 10^{-7} Pa. Cr(5 nm)/Au(10 nm) were deposited by an electron beam evaporator system to provide proper adhesion for photoresist. All the layers were deposited at RT as shown in Fig. 3.1(a). MTJ were fabricated with 10 μm^2 junction area in a hexagonal shape as shown in Fig.3.1(b) by conventional microfabrication technique with photolithography, Ar-ion milling and lift-off processes. There are different fabrication steps. These steps are listed as. **(A) Bottom electrode (B) MTJ pillar (C) Top electrode**

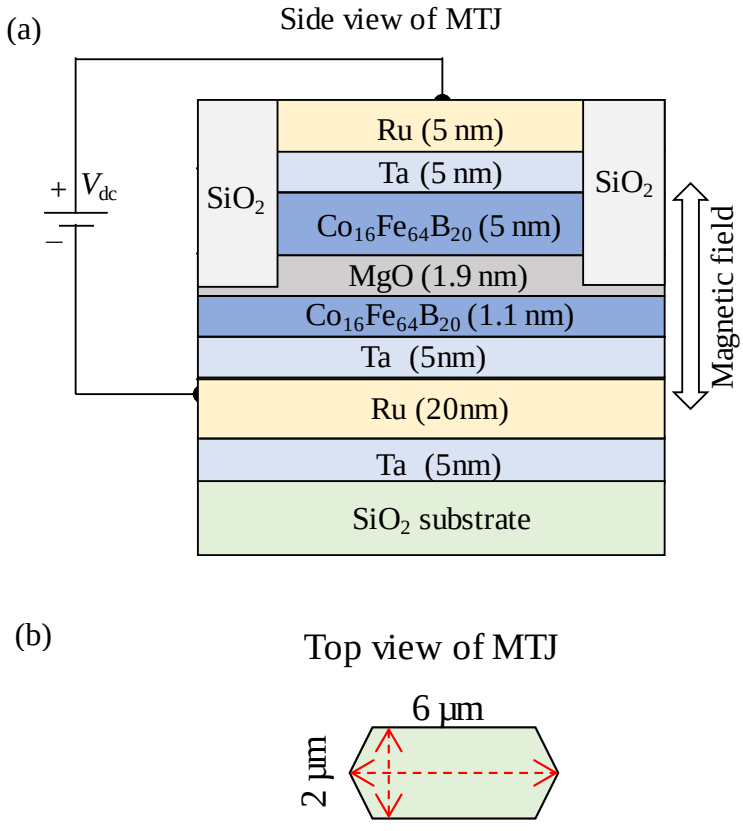

Figure 3.1. Schematic of MTJ (a) side view with film thickness (b) top view of MTJ

A) Bottom electrode

Schematic of the bottom electrode is shown in Fig. 3.2(a). Fabrication steps are listed in table 3.1.

(a)

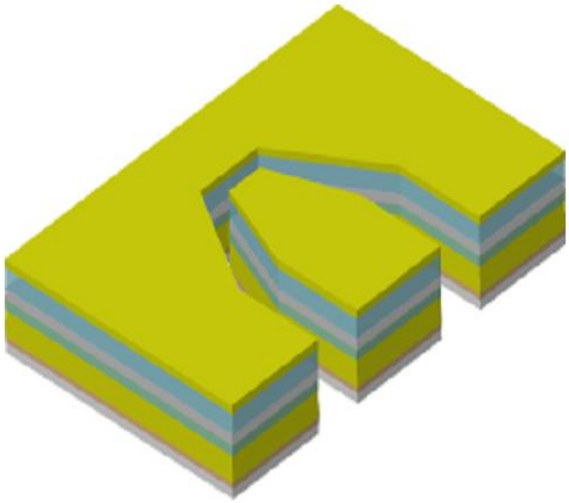

(b)

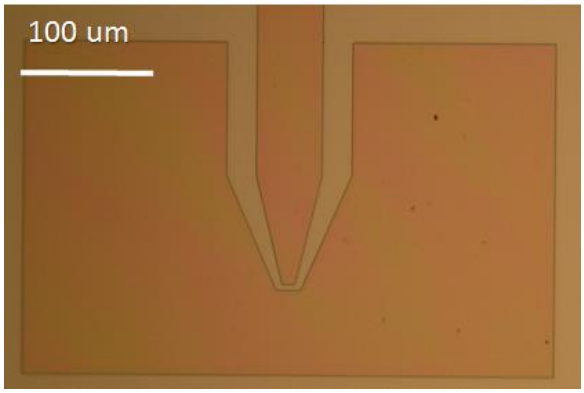

(c)

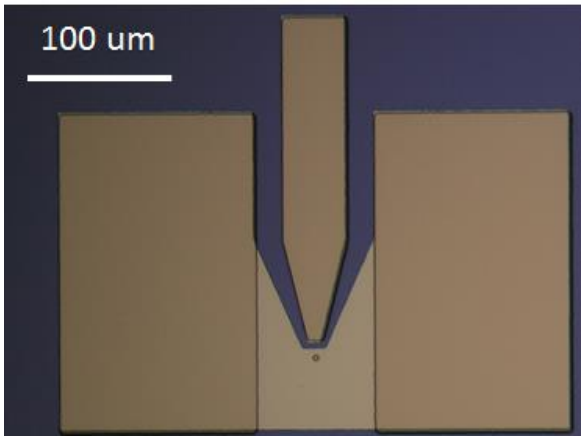

Figure 3.2. Bottom electrode (a) Schematic (b) after lithography (c) after etching

After sample deposition, cleaning of the sample was done in acetone followed by IPA in the sonicator at mild vibration. After that, promotor was coated as adhesion for positive photoresist. Optical lithography was done on contact mode, and the sample was developed to resist developer.

Sample cleaning		Chemical	Time (sec)	
		Acetone	60	
		IPA	60	
I_{st} level resist spinning	Promoter Spinning	Cycle	Speed (rpm)	Time(sec)
		Spread cycle	1000	3
		Main Cycle	4000	60
	Promoter heating	Temperature=70 °C		Time= 5×60 sec
	AZP 1350	Cycle	Speed (rpm)	Time(sec)
		Spread cycle	1000	3
		Main Cycle	4000	60
	Preheat	Temperature=100 °C		Time= 15×60 sec
Bottom electrode	Lithography	Mode	Contact mode	
		Dose	8 count	
Develop 1_{st} lithography	AZP Developer	AZP developer for 30 sec, Clean in DI water		
Observation	Microscopic observation	Take image .(shown in Fig. 3.2 (b))		
Dry Etching	Ar-ion milling	Base pressure: $2\times10^{-4} - 7\times10^{-4}$ Pa, Argon flow rate=8 sccm		

Resist removal		Chemical	Time (sec)
		Acetone	60
		IPA	60
Observation	Microscopic observation	Take Image .(shown in Fig. 3.2(c))	

Table 3.1 Fabrication steps of bottom electrode

Microscopic image of the sample is shown after lithography in Fig 3.2(b). Ar-ion milling etches the sample. After cleaning the sample in acetone and IPA, it is shown in Fig 3.2(c).

B) MTJ pillar

(a)

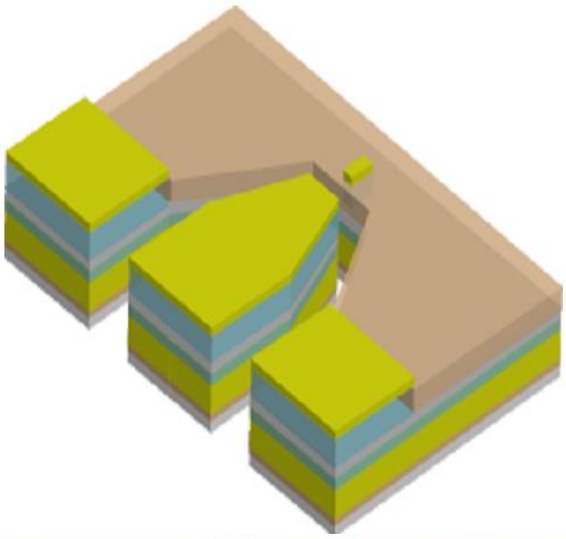

(b)

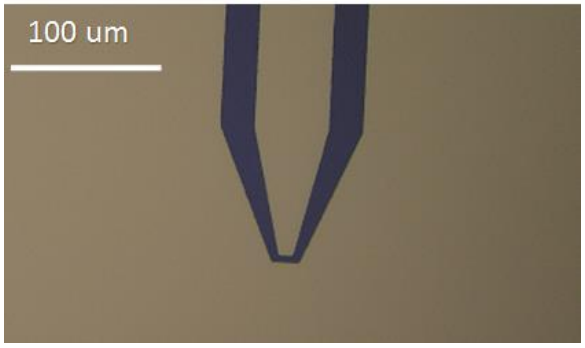

(c)

Figure 3.3. MTJ pillar (a) Schematic (b) after lithography (c) after etching

After the first lithography, cleaning of the sample was done in acetone followed by IPA in the sonicator. After that, the photoresist was coated. Optical lithography was done on contact mode with different exposure dose as mentioned in Table 3.2 and sample was developed to resist developer. Microscopic image of the sample is shown in Fig 3.2(b). The sample is etched by Ar-

ion milling after that isolation material SiO_2 was sputtered. Cleaning of the sample in acetone and IPA was done; it is shown in Fig. 3.3(c).

Sample cleaning		Chemical	Time (sec)	
		Acetone	60	
		IPA	60	
MTJ pillar	AZ5214E	Cycle	Speed (rpm)	Time(sec)
		Main Cycle	2500	30
	Preheat_1	Temperature=100 °C		60
	Lithography	Mode	contact mode	
		Dose	8 counts	
	Preheat_2	Temperature=140 °C		20
	Flood Exposure	Dose	90 counts	
Developer 2_{nd} lithography	AZ MIF Developer	AZMIF developer for 90 sec, Clean in DI water		
Dry etching	Ar-ion milling	Base pressure: $2\times10^{-4} - 7\times10^{-4}$ Pa	Argon flow rate=8 sccm	
Isolation	SiO_2 deposition		Argon flow rate=20 sccm, Process pressure=0.2 Pa	
Observation	Microscopic observation	Take Image		

Table 3.2 Fabrication steps of MTJ pillar electrode

C) Top electrode

(a)

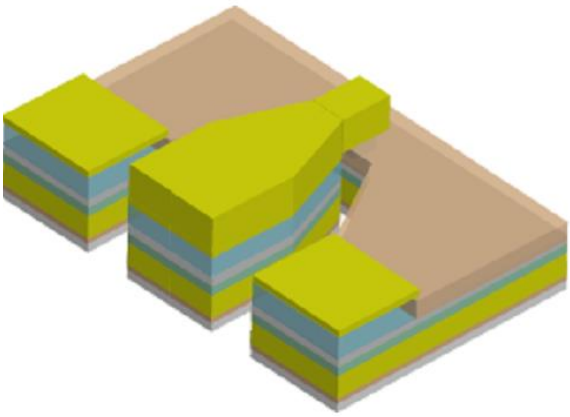

(b)

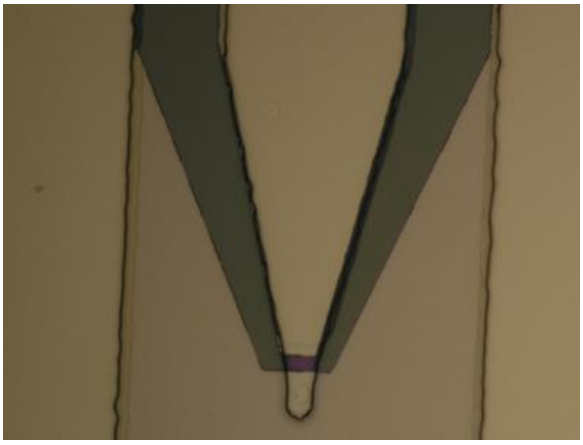

Figure 3.4. Top electrode (a) schematic (b) fabricated magnetic tunnel junction

Schematic of the bottom electrode are shown in Fig. 3.4(a). Fabrication steps are shown in table 3.3. After the second lithography, cleaning of the sample was done in acetone followed by IPA in the sonicator. After that, the photoresist coating was coated Optical lithography was done on contact mode with different exposure dose as mentioned in Table 3.3 and sample was developed to resist developer. Microscopic image of the sample is shown in Fig 3.4 (b).

Sample cleaning		Chemical	Time (sec)
		Acetone	60
		IPA	60

Top electrode	AZ5214E	Cycle	Speed (rpm)	Time(sec)
		Main Cycle	2500	30
	Preheat_1	Temperature=100 °C		60
	Lithography	Mode	contact mode	
		Dose	8 counts	
	Preheat_2	Temperature=140c		20
	Flood Exposure	Dose	90 counts	
Developer 3rd lithography	AZ MIF Developer	AZP developer for 90 sec, Clean in DI water		

Table 3.3 Fabrication steps of Top electrode

The resistance of different MTJ samples has been measured. After that, the samples have been annealed with different temperatures after microfabrication: 200 ˚C, 250 ˚C, 300 ˚C, 350 ˚C for 1 hour and one MTJ sample is without annealing. The sign of the bias voltage is defined with respect to the top CoFeB electrode.

3.2.2 Measurement

The TMR measurements were carried out using a conventional two-terminal technique in the magnetic field. All the measurements were performed at RT. Figure 3.5 shows that the magneto-

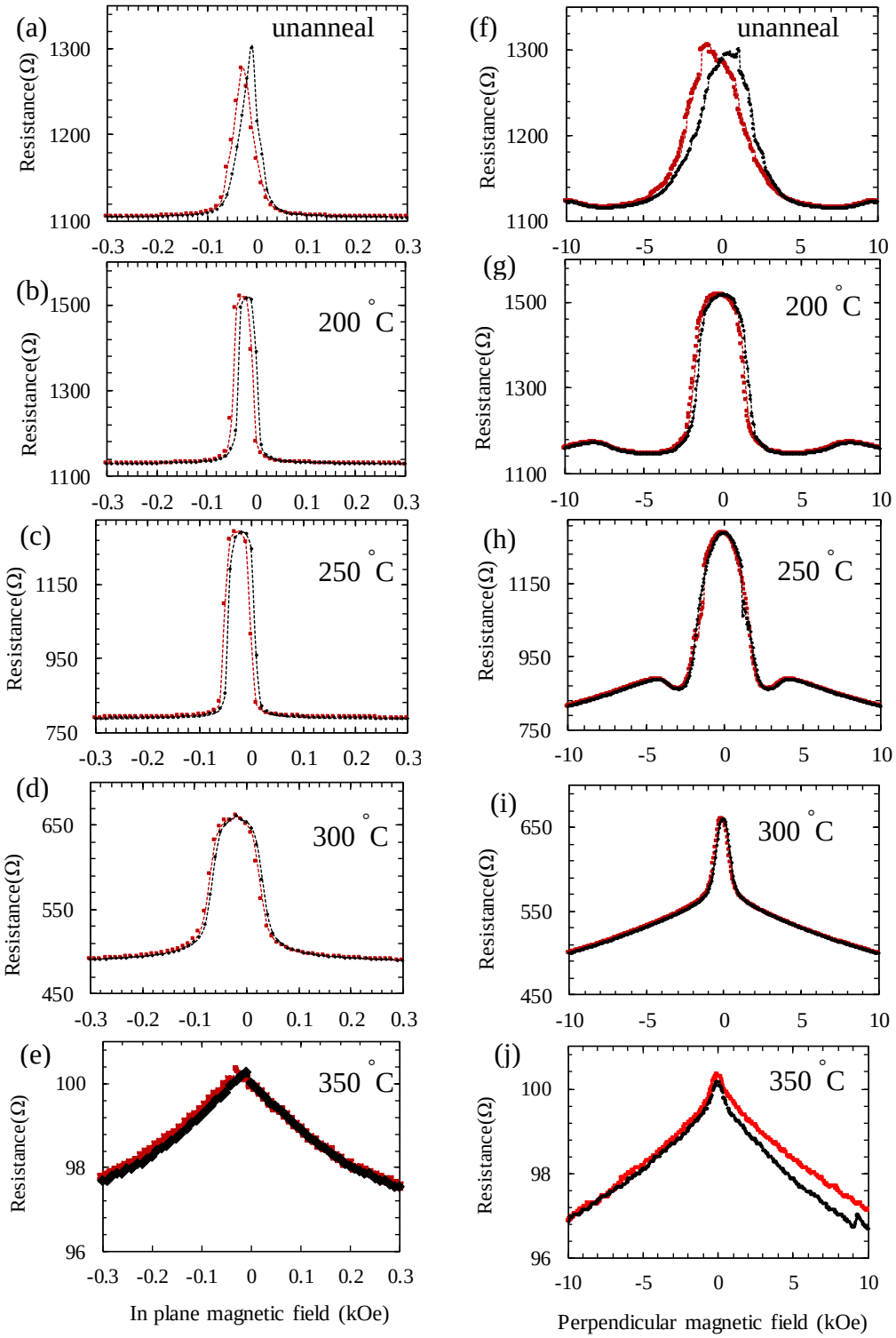

Figure 3.5. Magneto-resistance curves of the MTJ with different annealing temperature (a)-(e) under in-plane magnetic field (f)-(j) under a perpendicular magnetic field

resistance curves of MTJ with different annealed MTJ sample (a)-(e) in an in-plane magnetic field and (f)-(j) in a perpendicular magnetic field. It shows the thin film of the ferromagnetic layer in an in-plane direction.

Different annealed MTJ samples were measured in the bias voltage range from −1000 mV to +1000 mV. At 1 Volt bias voltage, the current through MTJ barrier is between 6μA−60μA and the current density through MTJ barrier is between 6 ×10 ^{7}A/m^{2} −6 ×10 ^{8}A/m^{2} with different annealed temperature samples. It is because of the large resistance area product (RA). The influence of current induced magnetic field and spin-transfer torque, because of current through and current density through the barrier layer, respectively is very negligible.

From eq^{n} (2.12), the conductance of MTJ in a perpendicular magnetic field $G(\theta_{\text{relative}},V)=\frac{1}{2}(G_{\text{P}}(V)+G_{\text{AP}}(V))+\frac{1}{2}(G_{\text{P}}(V)-G_{\text{AP}}(V))\cos(\theta_{\text{relative}})$. It is changing with the relative angle between the magnetization of the thick and thin ferromagnetic layer of the MTJ sample as shown in Fig. 3.6. The G_{P} (G_{AP}) is conductance of MTJ in parallel (antiparallel) state of magnetization of FM layer.

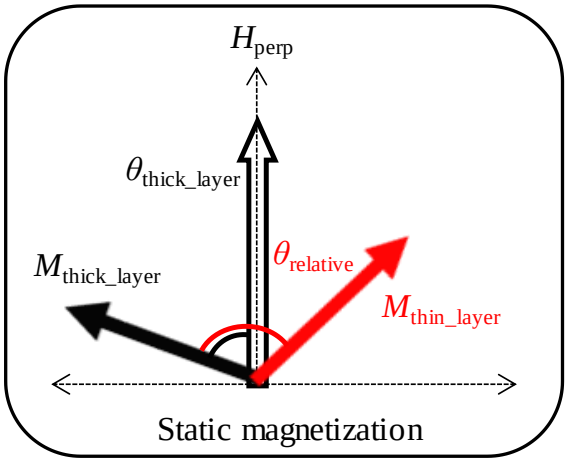

Figure 3.6. Schematic of magnetization of the thin and thick layer.

$M_{\text{thin\_layer}}$ and $M_{\text{thick\_layer}}$, respectively. The θ_{relative} is the angle between both magnetizations. The $\theta_{\text{thick\_layer}}$ is the angle between the magnetization of the thick layer and perpendicular magnetic field (H_{perp}).

The perpendicular component, M_{perp} of thin CoFeB layer is estimated from relative angle of the thin ferromagnetic layer with respect to the thick ferromagnetic layer in a perpendicular magnetic field. M_{perp}/ M_s is estimated from the TMR curves by following eq^n (2.14)

$$\frac{M_{perp}(V)}{M_S} = \cos\left(\cos^{-1}\left(\frac{2G(V) - \left(G_P(V) + G_{AP}(V)\right)}{\left(G_P(V) - G_{AP}(V)\right)} \right) - \cos^{-1}\left(\frac{H_{perp}}{H_{s,thick}} \right) \right)$$

where $\mu_0 M_s$ (1.44 T) is saturation magnetization of thin FM layer and $H_{s,thick}$ is a minimum perpendicular magnetic field at which magnetization of thick FM layer becomes parallel to $H_{perp.}$

Red rectangle, black circle and purple triangle represent bias voltage −800mV, +50 mV, +800 mV in (a)–(d) and these dots represent bias voltage −500mV, +50 mV, +500 mV in (e) respectively. The annealing temperature is mentioned in the graph.

The perpendicular magnetic anisotropy per unit volume, E_{perp}, of the thin ferromagnetic material was estimated from Fig. 3.7(a)−(e) under different bias voltage by eq^n (2.13).

$$E_{an}(V) = -\int_0^{H_{s,thin}} \left(1 - \frac{M_{perp}(V)}{M_s}\right) dH_{perp}$$

If the thin ferromagnetic layer possesses uniaxial crystalline anisotropy $K_{u,}$ surface anisotropy K_s and voltage-induced surface anisotropy ΔK_s (V), the E_{an} can be expressed as eq^n (2.15)

$$E_{an}(V) \times d = \left(-\frac{1}{2}\mu_0 {M_s}^2 + K_u \right) d + K_s + \Delta K_s(V)$$

The voltage-controlled magnetic anisotropy energy E_{an} versus electric field is plotted in Figs. 3.7(f)−(j).

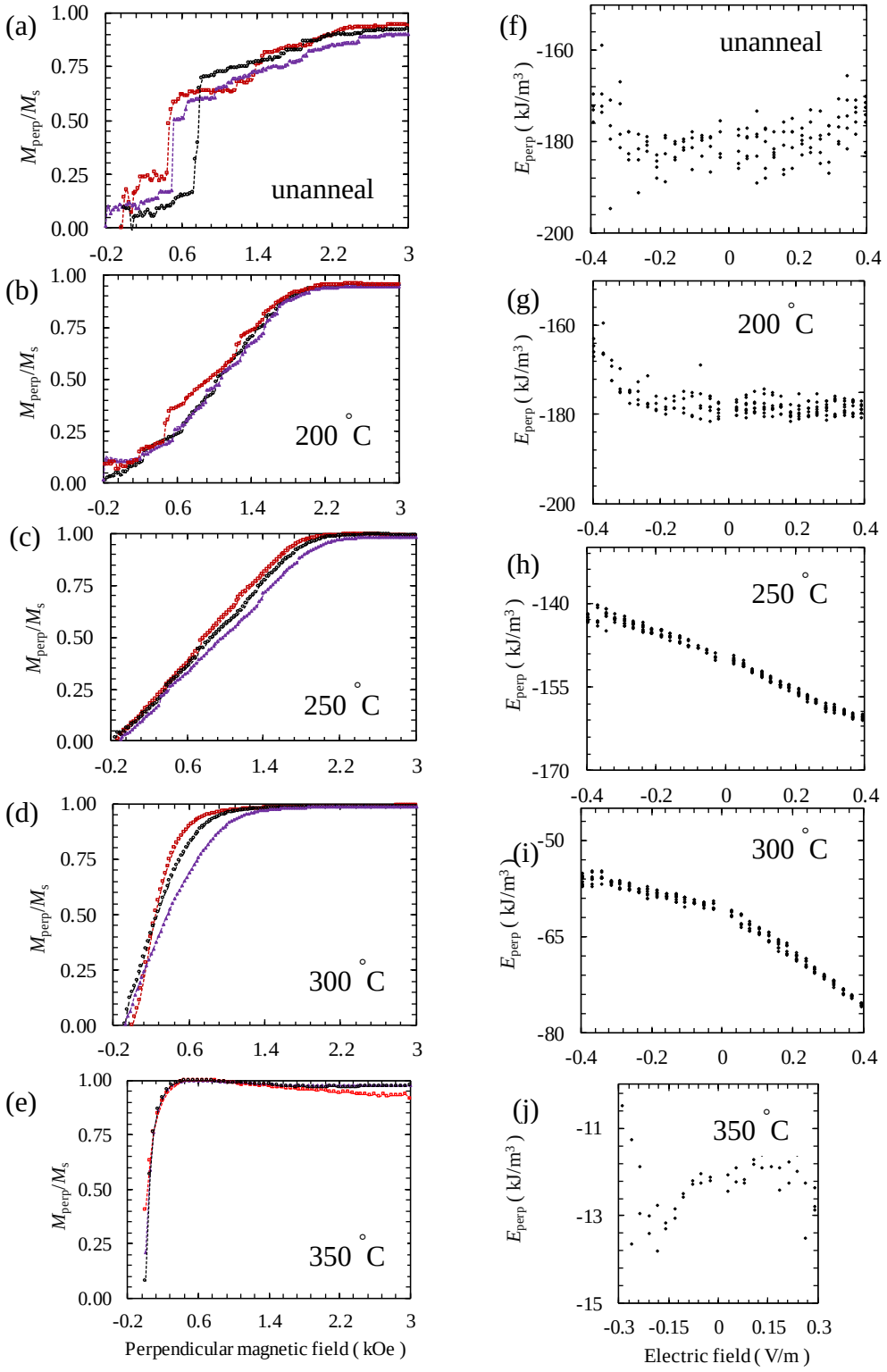
(a)
unanneal
(b)
200 °C
(c)
250 °C
(d)
300 °C
(e)
350 °C
M_{perp}/M_s
Perpendicular magnetic field (kOe)
(f)
unanneal
(g)
200 °C
(h)
250 °C
(i)
300 °C
(j)
350 °C
E_{perp} (kJ/m^3)
Electric field (V/m)

3.3 Result and discussion

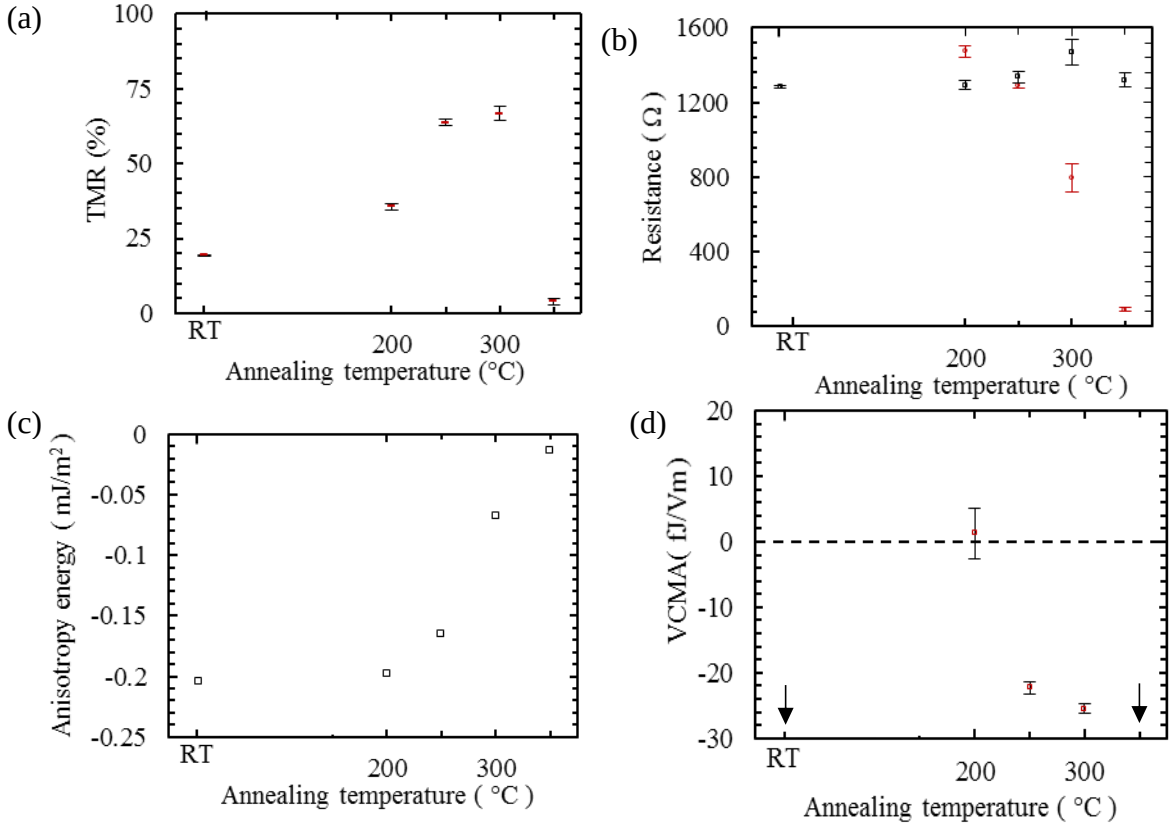

Figure 3.7. Post-annealing temperature dependence (without annealed sample is shown at 27 ˚C (RT) on annealing temperature axis) (a) Red rectangle with error bar shows average TMR ratio of some selected MTJ devices with these devices' standard-deviation in-plane magnetic field (b) Red and black square with error bar shows the average resistance with their standard deviation of same selected MTJ devices as shown in Fig. 3.8(a) before and after the annealing, respectively, (c) Anisotropy energy (one device selected from each annealing temperature devices near averaged TMR region in all selected devices in Figs. 3.8(a) & 3.8(b)) in perpendicular magnetic field and (d) the VCMA with standard deviation, of same device selected in Fig. 3.8(c), has been characterized by bias-voltage dependence in a perpendicular magnetic field from lower bias voltage. Red rectangle shows it with error bar, and black downside arrow shows an annealing temperature at which VCMA has not been evaluated.

The TMR ratio increases with annealing temperatures until around 300 ˚C because of an increase in crystallinity in the ferromagnetic CoFeB layer of MTJ as shown in Fig. 3.8(a). The

resistance of MTJ is almost similar after annealing at 200 °C and 250 °C as shown in Fig. 3.8(b). However, The TMR ratio and the post-annealing resistance decrease sharply after 300 °C's annealing as shown in Fig. 3.8(a) and Fig. 3.8(b), respectively. These are because of leakage either at junction boundary or in MgO barrier. The RA value of MTJ samples was around 15 $k\Omega\mu m^2$ before annealing the samples. Perpendicular magnetic anisotropy energy of MTJ samples was estimated in Fig. 3.8(c). The VCMA was evaluated from a lower bias voltage of −0.1 V to +0.1 V as shown in Fig. 3.8(d). The ferromagnetic layer is amorphous in unannealed MTJ. In the unannealed MTJ, the magnetization of the amorphous ferromagnetic layer is changing abruptly under a perpendicular magnetic field. In the 350 °C annealed sample, there is leakage either at junction boundary or in MgO barrier. Because of these reasons, quantitative evaluation of VCMA of both samples is not possible. Between 200 °C to 300 °C annealing, this work shows that maximum VCMA and maximum TMR ratio of Ta/CoFeB/MgO/CoFeB/Ta /Ru MTJ are achieved with 300 °C annealing.

3.4 Conclusion

The voltage-controlled magnetic anisotropy and the tunnel magnetoresistance in magnetic tunnel junctions with different annealing temperature have been investigated. We found that TMR and VCMA are increasing with increasing post-annealing temperature between 200 °C to 300 °C. The resistance of the MTJ layer is decreasing with increasing post-annealing temperature. The maximum VCMA and TMR of Ta/ CoFeB/ MgO sample are achieved 28 fJ/Vm and 62%, respectively with 300 °C annealed sample. Therefore, this work indicates that 300 °C annealing is a good candidate for better TMR and VCMA in Ta/CoFeB/MgO system between 200 °C to 300 °C annealing.

4 Spin waves dynamics

4.1 Magnetostatic surface spin wave

The spin waves are propagating disturbance in a group of spins of magnetic materials. These collective excitations occur in magnetic lattices with continuous symmetry. It is called magneto-static surface spin wave (MSSW). The MSSW can be excited by applying a fluctuating magnetic field in the film plane, and it propagates to the normal direction of in-plane magnetic field direction. The fluctuating magnetic field generates precession in each spin. Each spin in MSSW has a particular phase difference. The spin wave propagates at a particular wavelength. The spin wave carries the different magnetic properties. The magnetic anisotropy in the *x*-direction can be measured under the

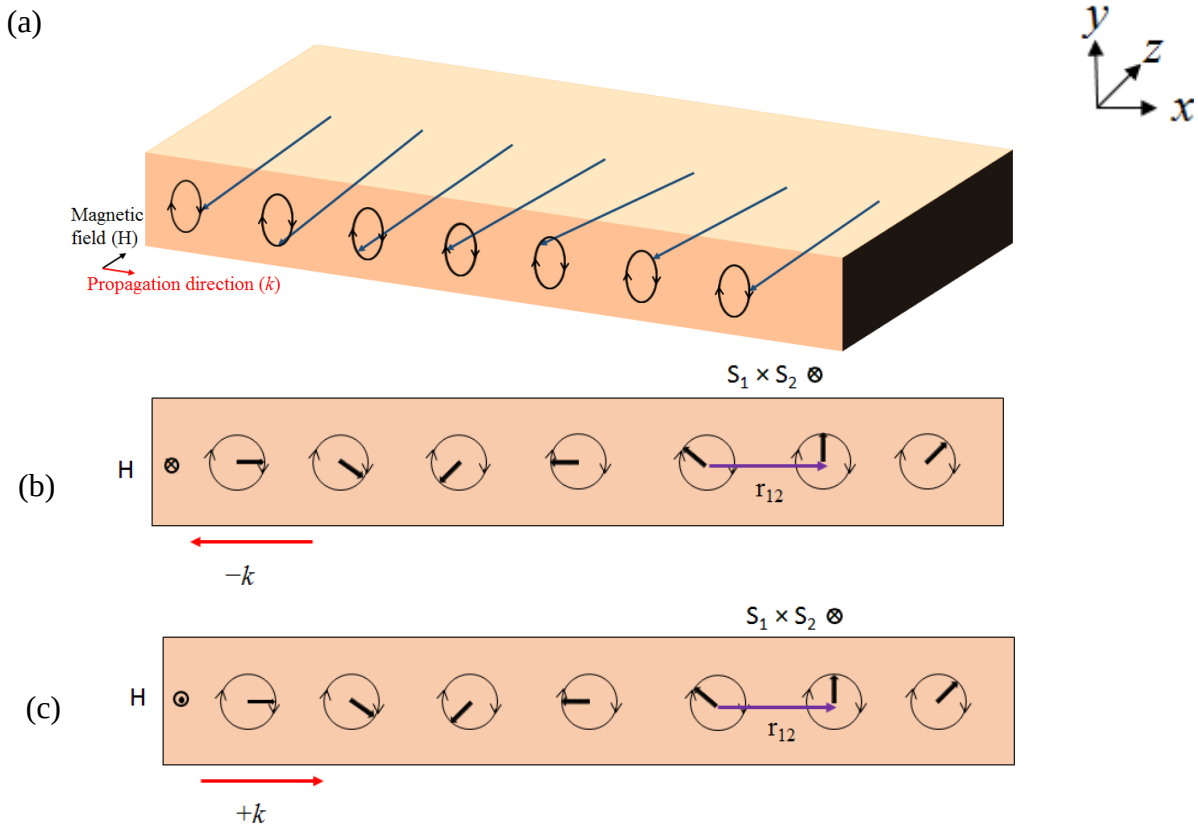

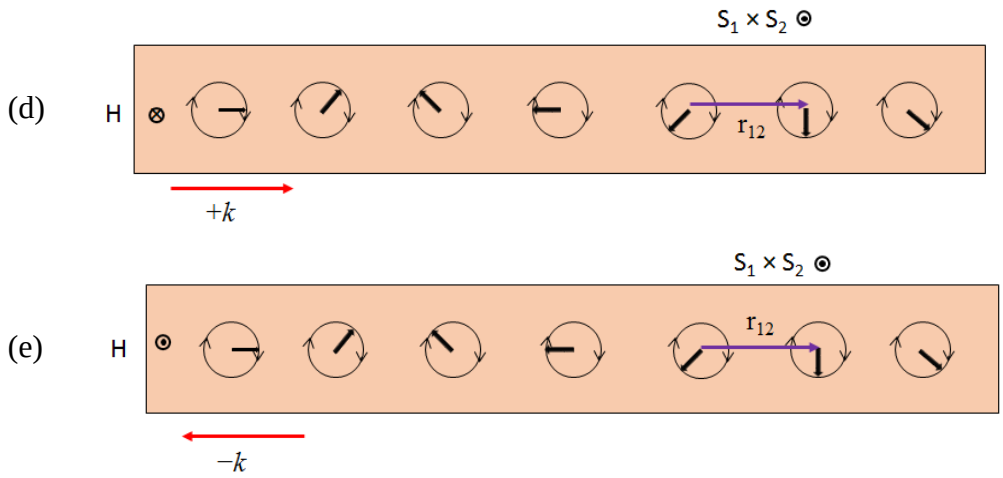

Figure 4.1.Schematic diagram of spin wave propagation and chirality relation

(a) The MSSW propagation in ferromagnetic material

(b) –(e) The projection of each spin-dynamics in *x*-*z* plane. The magnetic field direction H, propagation vector r_{12} and $S_1 \times S_2$ are shown for each configuration.

in-plane plane magnetized magnetic film. Chirality is another merit of a spin wave. In the above Fig 4.1(b)-(e), the projection of spins of Fig. 4.1(a) are depicted. Fig. 4.1(b)-(c) show the $S_1 \times S_2$ direction downward under +ve(-ve) magnetic field and wave propagation in $+x(-x)$ direction and Fig. 4.1(e)-(f) show the $S_1 \times S_2$ direction upward under +ve(-ve) magnetic field and wave propagation in $+x(-x)$ direction. These interactions imply that the chirality of the MSSWs depends on magnetic direction and spin wave propagation direction. MSSW equation can investigate the chirality dependent magnetic property S1 × S2, DMI. MSSW equation can be walker-equation.

4.2 Walker equation

The Walker-equation derives the magneto-static surface spin wave, is derived from Landau Lifshitz equation and Maxwell equation.

The schematic of the ferromagnetic material (FM) slab is shown in Fig. 4.2. Here, static magnetization M_o and the external magnetic field H_o are applied in the z-direction. The $\hat{k}$ is a unit vector in z-direction The spin wave with wave number k is propagating The spin wave propagating

vector k_p is defined as $k_p = (k_x, k_z) = k_p(\sin\phi, \cos\phi)$, where ϕ is the angle between magnetization and k_p. The FM slab thickness $t_{Fe,}$ with surface $y = \pm t_{Fe}/2$.

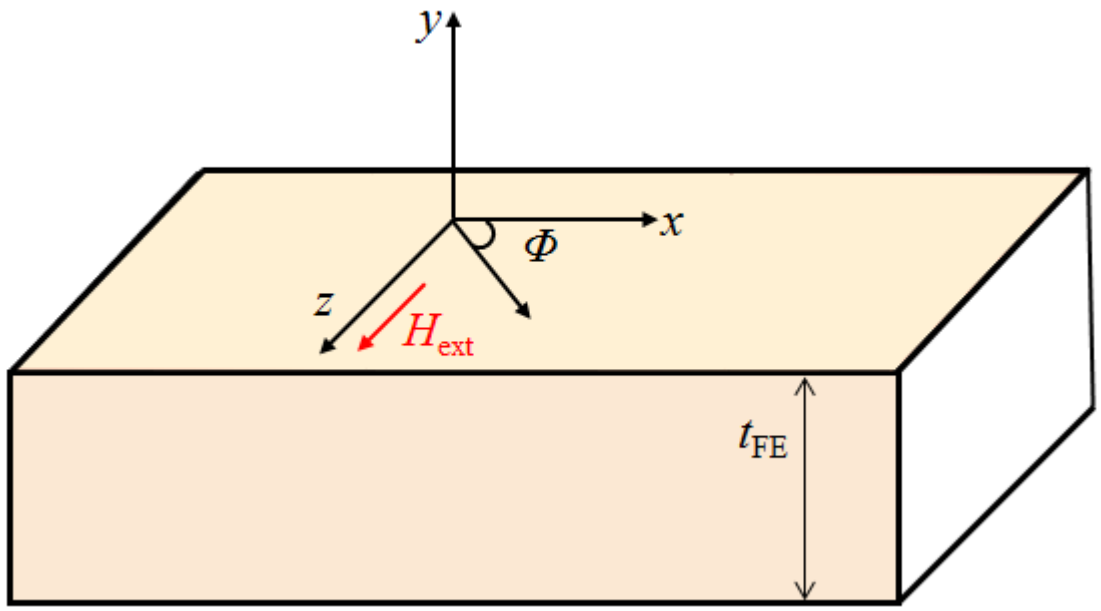

Figure 4.2. The geometry in FM slab for estimating of MSSW.

In the magneto-static surface wave region, the wavelength of MSSW is very large compared to the lattice spacing, and a continuum approximation for the FM would be valid. Here, the effective magnetic field is an only the external magnetic field.

So Landau Lifshitz equation (from supplementary eq^n (11))

$$\frac{1}{\gamma}\frac{d}{dt}\vec{M} = -\mu_0 \vec{M} \times \vec{H} \text{ ----------(4.1)}$$

A static magnetic field is applied in the *z*-direction with an electromagnetic part at frequency ω at FM slab.

$$\vec{M} = M_S \hat{k} + \vec{m}(\vec{r}) \exp(-i\omega t) \text{ ---------(4.2)}$$

$$\vec{H} = H_{ext} \hat{k} + \vec{h}(\vec{r}) \exp(-i\omega t) \text{ ---------(4.3)}$$

The fluctuating magnetic field *h* causes the fluctuating magnetization *m* with frequency ω. Here, we use that the effective magnetic field is only Zeeman field. From eq^n (4.2), eq^n (4.3) into and eq^n (4.1).

$$\frac{1}{\gamma}\frac{\mathrm{d}}{\mathrm{dt}}(M_S\hat{k}+\vec{m}(\vec{r})\exp(-i\omega t))=-\mu_0\left[(M_S\hat{k}+\vec{m}(\vec{r})\exp(-i\omega t))\times(H_{ext}\hat{k}+\vec{h}(\vec{r})\exp(-i\omega t))\right]\text{------(4.4)}$$

Neglecting the small terms and making the usual linear approximation of eq^n (4.4), the result is

$$-i\omega\vec{m}(\vec{r})=-\mu_0\gamma\hat{k}\times[M_S\vec{h}(\vec{r})-H_{ext}\vec{m}(\vec{r})]\text{--------(4.5)}$$

This eq^n (4.5) can be expressed as a susceptibility relation involving the *x* and *y* component of the fluctuation magnetization field and magnetic fields, $\vec{m}=\bar{\chi}\vec{h}$

$$\begin{pmatrix}m_x\\m_y\end{pmatrix}=\begin{pmatrix}\chi & i\kappa\\-i\kappa & \chi\end{pmatrix}\begin{pmatrix}h_x\\h_y\end{pmatrix}\text{------(4.6)}$$

where, $\chi=\dfrac{\omega_m\omega_0}{(\omega_0^2-\omega^2)}$, $\kappa=\dfrac{\omega_m\omega}{(\omega_0^2-\omega^2)}$

where, $\omega_m=\gamma\mu_o M_s$ and $\omega_0=\gamma\mu_o H_{ext}$

From Maxwell's equation, $\vec{h}(\vec{r})$ is satisfying

$$\nabla\times\vec{h}(\vec{r})=0\text{------(4.7)}$$

This eq^n (4.7) will satisfy

$$\vec{h}(\vec{r})=-\nabla\psi\text{-----(4.8)}$$

where, ψ is called scalar magneto-static potential.

From another part of Maxwell's equation, $\vec{m}(\vec{r})$ and $\vec{h}(\vec{r})$ are satisfying

$$\nabla\bullet[\vec{h}(\vec{r})+\vec{m}(\vec{r})]=0\text{------(4.9)}$$

From eq^n (4.8) and eq^n (4.9),

$$(1+\chi)\left(\frac{\partial^2\psi}{\partial x^2}+\frac{\partial^2\psi}{\partial y^2}\right)+\frac{\partial^2\psi}{\partial z^2}=0\text{------(4.10)}$$

It is called Walker equation inside the FM sab. This equation is simply $\nabla^2\psi=0$ outside the FM slab.

4.3 Dispersion relation of spin wave

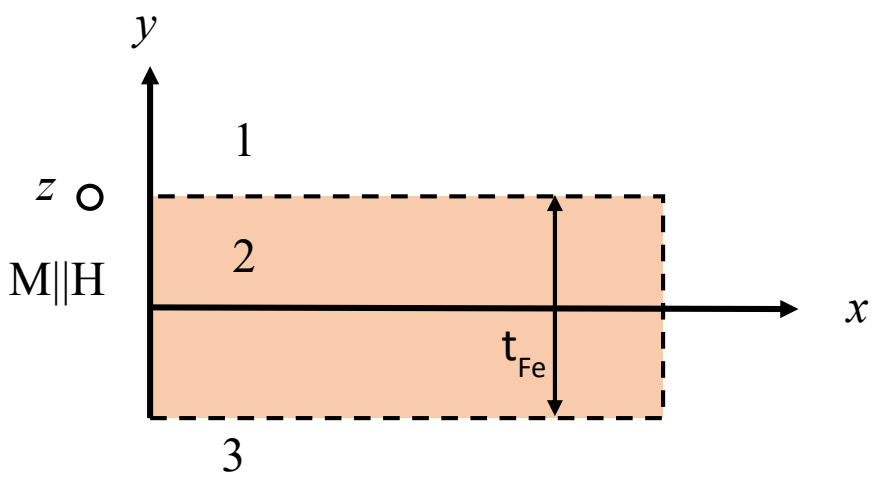

Figure 4.3. Side view of FM slab. Magnetization is saturated in the z-direction, and the wave is propagating in the y-direction.

In this subsection, MSSW is derived in the region 1,3 and region 2 as shown in Fig. 4.3. The wave number is the same for *x* and *y*-direction in region 1,3, and it is different for region 2. We assumed the wave number (k_p) k_1(k_2) in region 1,3 and k_x (k_y) in region 2 for *x* (*y*) direction. Then from Walker equation and boundary condition,

$\psi_{1,3} = \psi_a e^{(iv(k_1 x \pm k_2 y))}$ (in the region 1,3) ------(4.11)

$\psi_2 = \psi_b e^{(iv(k_x x \pm k_y y))}$ (in the region 2) ------(4.12)

where ψ_a (ψ_b) is the scalar potential in the region 1,3 (2) and *v* represents propagation direction in +*x*(-*x*) direction *v* =+1(-1). In the case of Fe FM, there are different anisotropy such as crystalline, shape and interfacial anisotropy. However, for the simple case, we are neglecting it, and we are assuming the ferromagnetic material as isotropic material. Therefore, k_x =k_y in eq^n (4.12),

then from Walker equation, eq^n (4.10) in region 2

$(1+\chi)(k_x^2 + k_y^2) = 0$ ------(4.13)

From the above equation, there are two solutions. First, $(1+\chi)=0$, this happened only a specific frequency $\omega=\gamma\mu_o H_{\text{ext}}$. Second, $(k_x{}^2+k_y{}^2)=0$, this happens only when the wave propagates only at the surface in the y-direction. $k_x{}^2=-k_y{}^2$. The k_y is having imaginary value. Therefore it attenuates in the *x*-direction. So we can write MSSW wave as $\psi_2=(\mathrm{a}e^{k_x y}+\mathrm{b}e^{-k_x y})e^{ivk_x x}$ ------(4.14)

Then, we apply the boundary conditions at $y = \pm t_{Fe}/2$, for the scalar potential.

$$\psi_1 e^{-k_1\frac{t_{Fe}}{2}}=(\mathrm{a}e^{k_1\frac{tFe}{2}}+\mathrm{b}e^{-k_1\frac{t_{Fe}}{2}})\text{------(4.15)}$$

$$\psi_3 e^{-k_1\frac{t_{Fe}}{2}}=(\mathrm{a}e^{-k_1\frac{tFe}{2}}+\mathrm{b}e^{k_1\frac{t_{Fe}}{2}})\text{------(4.16)}$$

where, $k_1=k_x$ is needed for *y* direction-boundary condition. The magnetic flux density for the *x*-axis must be continuous. The magnetic flux density for the *x*-axis is given as follows,

$$b_{y(1)}=\nabla_y\psi_1\text{--------(4.17)}$$

$$b_{y(2)}=i\kappa\nabla_x\psi+(1+\chi)\nabla_y\psi\text{--------(4.18)}$$

Then the needed conditions for the magnetic flux density is obtained from eq^n (4.15), (4.16), (4.17) and (4.18) as follows,

$$\psi_1 e^{-k_1\frac{t_{Fe}}{2}}=\kappa v(\mathrm{a}e^{k_1\frac{tFe}{2}}+\mathrm{b}e^{-k_1\frac{t_{Fe}}{2}})-(1+\chi)(\mathrm{a}e^{k_1\frac{tFe}{2}}+\mathrm{b}e^{-k_1\frac{t_{Fe}}{2}})\text{------(4.19)}$$

$$\psi_3 e^{k_1\frac{t_{Fe}}{2}}=-\kappa v(\mathrm{a}e^{k_1\frac{tFe}{2}}+\mathrm{b}e^{-k_1\frac{t_{Fe}}{2}})+(1+\chi)(\mathrm{a}e^{k_1\frac{tFe}{2}}-\mathrm{b}e^{-k_1\frac{t_{Fe}}{2}})\text{------(4.20)}$$

To obtain a trivial solution from these 4 boundary conditions, the determinant of following matrix must be zero as following,

$$\det\begin{bmatrix}(\chi+2-v\kappa)e^{k_1\frac{t_{Fe}}{2}} & -(\chi+v\kappa)e^{-k_1\frac{t_{Fe}}{2}}\\ -(\chi-v\kappa)e^{-k_1\frac{t_{Fe}}{2}} & (\chi+2+v\kappa)e^{k_1\frac{t_{Fe}}{2}}\end{bmatrix}\text{------(4.21)}$$

Then, by using above eq., following basic dispersion relation of MSSW is obtained,

$$\omega^2=\omega_0(\omega_0+\omega_0)+\frac{\omega_M{}^2}{4}\left[1-e^{-2k_1t_{Fe}}\right]\text{------(4.22)}$$

By using eq^{n} (4.21), the scalar potential for each region eq^{n} (4.10) and (4.11) can be obtained as follows,

$$\psi_1 = a(\mathrm{e}^{k_1 t_{Fe}} + p(v))\mathrm{e}^{k_1 x - iv k_1 y} \text{ ------(4.23)}$$

$$\psi_2 = (\mathrm{ae}^{k_1 \frac{x}{2}} + p(v)\mathrm{e}^{-k_1 \frac{x}{2}})\mathrm{e}^{iv k_1 y} \text{ ------(4.24)}$$

$$\psi_3 = a(1 + p(v)\mathrm{e}^{k_1 t_{Fe}})\mathrm{e}^{k_1 x + iv k_1 y} \text{ ------(4.25)}$$

Where $p(v)$ satisfies the following relation,

$$p(v) = \frac{b}{a} = \frac{(\chi - v\kappa)}{(\chi + 2 + v\kappa)}\mathrm{e}^{k_1 t_{Fe}} = \frac{(\chi + 2 - v\kappa)}{(\chi + v\kappa)}\mathrm{e}^{-k_1 t_{Fe}} \text{ ------(4.26)}$$

The dispersion relation of the MSSW becomes a different formula for the single crystalline FM because of anisotropies. When the ferromagnetic material has cubic and uniaxial anisotropy, its expanded dispersion relation is derived. Here, I consider the ultra-thin single crystalline FM. Therefore, crystalline anisotropy (H_{cry}), interfacial anisotropy (H_{int}) and shape anisotropy (M_{s}) should be considered.

The anisotropy energy of FM slab is defined as,

$$E_{\mathrm{Pre}} = \frac{\mu_0}{2}\vec{m}e^{-i\omega t}\begin{pmatrix} h_{cry} \\ h_{cry} + M_o + h_{\mathrm{int}} \end{pmatrix} \text{------(4.27)}$$

Each spin of FM feels this anisotropy energy during precession. Therefore, the effective magnetic field is estimated from eq^{n} (4.3) and (4.27) as,

$$H_{\mathrm{effective}} = H_o\hat{k} + \frac{\mu_0}{2}\begin{pmatrix} H_{cry} \\ H_{cry} + M_o - H_{\mathrm{int}} \end{pmatrix}\vec{m}e^{-i\omega t} + \vec{h}e^{-i\omega t} \text{ ------(4.28)}$$

As we know that $\vec{m} = \overline{\chi}\vec{h}$

$$\begin{pmatrix} m_x \\ m_y \end{pmatrix} = \begin{pmatrix} \omega_y & -i\omega \\ -i\omega & \omega_x \end{pmatrix}\begin{pmatrix} h_x \\ h_y \end{pmatrix} \text{------(4.29)}$$

The susceptibility of FM slab is defined from eq^{n} (4.29),

$$\bar{\chi} = \begin{pmatrix} \omega_y & -i\omega \\ -i\omega & \omega_x \end{pmatrix} \text{------(4.30)}$$

Where $\omega_x = \gamma\mu_o((|H_{\text{ext}}| + H_{\text{cry}})$ and $\omega_y = \gamma\mu_o(|H_{\text{ext}}| + M_{\text{S}} + H_{\text{cry}} - H_{\text{int}})$.-----(4.31)

Then the resonant frequency *f* of FM slab is defined as

$$\omega^2 = [\omega_0 - 2\gamma H_{cry})][\omega_0 + \omega_{\text{M}} - 2\gamma(H_{cry} - H_{\text{int}})] + \omega_{\text{M}}(\omega_0 - 2\gamma H_{\text{int}})\frac{1 - e^{-2k_1 t_{Fe}}}{4} \text{------(4.32)}$$

This equation from eq^{n} (4.32), can be written

$$f = -\frac{\gamma}{2\pi}\sqrt{(|H_{\text{ext}}| + H_{\text{cry}})(|H_{\text{ext}}| + M_{\text{S}} + H_{\text{cry}} - H_{\text{int}}) + \frac{M_{\text{S}}}{4}(M_{\text{S}} - H_{\text{int}})(1 - \exp(-2|k|t_{\text{Fe}}))} \text{------(4.33)}$$

4.4 The voltage-induced frequency shifts of MSSW

As we know, the interfacial magnetic property of FM changes under the perpendicular field is called a voltage effect. When a voltage is applied across the FM/MgO system, it modifies the interfacial anisotropy energy and *interfacial* DMI. Therefore, the resonant frequency is being shifted by applying voltage. In this subsection, for the case of a V|FM|MgO system, a mechanism of frequency shifts induced by voltage is shown.

An FM thin film is sandwiched by MgO and V (Buffer layer). We assume that the surface anisotropy appears only at the FM/MgO interface. Therefore, the averaged interface anisotropy energy exerted on the MSSW propagating toward the ± *x*-direction can be approximated by

$$\frac{\mu_0}{2} M_{\text{S}} H_{\text{int}}^{\mp} = K_u \frac{\int d^3\delta(y) e^{\mp k_y y}}{\int d^3 e^{\mp k_y y}} \text{------(4.34)}$$

where, $H_{\text{int}}^{\mp}$ is the averaged interfacial anisotropy field for the MSSW propagating toward the ± *x*-direction, K_{u} is the interfacial magnetic anisotropy energy and κ_{y} is the attenuation coefficient of the

MSSW. The voltage-induced interfacial anisotropy field change as $\delta H_{\text{int}}^{\mp}$ is estimated from eq^{n} (4.34), as.

$$\delta H_{\text{int}}^{\mp} = \frac{2\delta K_u}{\mu_0 M_S}\left[\frac{\mp k_y}{e^{\mp k_y y}-1}\right] \text{------(4.35)}$$

(a) – Without the interfacial DMI change

The frequency shift because of this anisotropy is estimated as,

$$\delta f = \frac{\gamma}{2\pi}\frac{|H_{\text{ext}}| + H_{\text{cry}} + \frac{M_S}{2}|k|t_{\text{Fe}}}{2f}\frac{2\delta K_u}{\mu_0 M_S}\left[\frac{\mp k_y}{e^{\mp k_y y}-1}\right] \text{------(4.36)}$$

This frequency shift includes the contribution of interfacial anisotropy changes to the voltage-induced chirality-dependent frequency shift. Here, we neglect the term depending on the interfacial DMI change and we divide this frequency shift into two components; one is the propagation direction independent shift δf_{sym}, and the other is propagation-direction-dependent shift δf_{asym}:

$$\delta f_{sym} = \frac{\gamma}{2\pi}\frac{|H_{\text{ext}}| + H_{\text{cry}} + \frac{M_S}{2}|k|t_{\text{Fe}}}{2f}\frac{2\delta K_u}{\mu_0 M_S}\frac{1}{t_{\text{Fe}}} \text{------(4.37)}$$

$$\delta f_{asym} = \frac{\gamma}{2\pi}\frac{|H_{\text{ext}}| + H_{\text{cry}} + \frac{M_S}{2}|k|t_{\text{Fe}}}{2f}\frac{2\delta K_u}{\mu_0 M_S}\frac{k_y}{2} \text{------(4.38)}$$

Here, I designed a spin wave spectroscopy structure. The ultrathin FM is deposited on Fe. I applied rf wave. Both antennas are used as trans-receiver. They excite and detect spin wave in FM sab

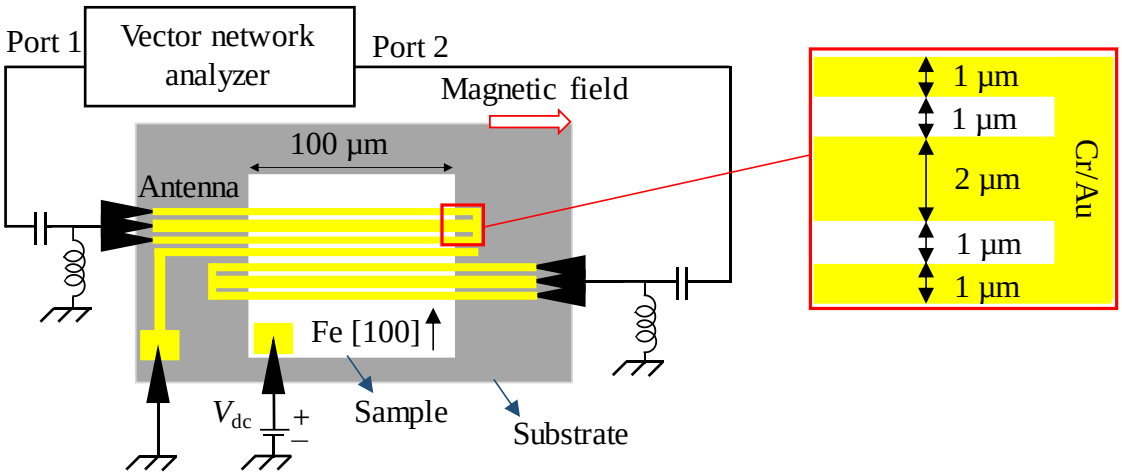

Figure 4.4. Schematic of the device structure and measurement setup. The black arrow shows the Fe [100] direction. The yellow color shows the antenna and gated contact pad. The black color shows the ground-signal-ground (GSG) probes. A dc voltage (V_{dc}) is applied to the sample.

From eq^{n} (4.37), eq^{n} (4.38) and designed parameter of our device in Fig. 4.4

(k_y =1.2/µm and t_{Fe} =20 nm)

$$\frac{\delta f_{asym}}{\delta f_{sym}} = \frac{k_y t_{Fe}}{2} = 1.2\% \text{ ------(4.39)}$$

Since, the asymmetric part is very small. Therefore, we can neglect the asymmetric term

The symmetrical part of the frequency shift is described as $\delta f_{sym} = \left(\frac{\delta f_{21} + \delta f_{12}}{2V_{dc}} \right)$ from my device design shown in Fig. 4.4. The f_{21} and f_{12} indicate resonant frequency from trans receiver 1 and 2 in my special fabricated device structure shown in Fig. 4.4. The symmetry terms (δf_{12}+δf_{21})/2V_{dc} are correlated to voltage controlled magnetic anisotropy (VCMA) because of 1 volt, and E_{MgO} is the perpendicular electric field because of 1 volt.

From eq^{n} (4.37) and symmetric part of frequency shift, the anisotropy energy change δK_u is described as

$$\delta K_u = \frac{-f\left(\frac{\delta f_{21}+\delta f_{12}}{2V_{dc}}\right)M_S\, t_{Fe}}{\left(\frac{\gamma}{2\pi}\right)^2\left(\left|H_{ext}\right|+H_{cry}+\frac{M_S}{4}\left(1-e^{-2|k|t_{Fe}}\right)\right)} \text{ ------(4.40)}$$

From eq^n (4.40), the voltage controlled anisotropy energy change (VCMA= δK_u /E_{MgO}) is described as

$$\text{VCMA} = \frac{-f\left(\frac{\delta f_{21}+\delta f_{12}}{2V_{dc}}\right)M_S\, t_{Fe}}{\left(\frac{\gamma}{2\pi}\right)^2\left(\left|H_{ext}\right|+H_{cry}+\frac{M_S}{4}\left(1-e^{-2|k|t_{Fe}}\right)\right)E_{MgO}} \text{ ------(4.41)}$$

(b) With the interfacial DMI change

Now, the resonant frequency *f* from eq^n (4.32), of FM slab by including DMI energy contribution is defined as

$$f = -\frac{\gamma}{2\pi}\sqrt{\left(\left|H_{ext}\right|+H_{cry}\right)\left(\left|H_{ext}\right|+M_S+H_{cry}-H_{int}\right)+\frac{M_S}{4}\left(M_S-H_{int}\right)\left(1-\exp\left(-2|k|t_{Fe}\right)\right)}-\frac{\gamma}{\pi M_S}Dk \text{ ------(4.42)}$$

where, *D* is the absolute value of **D** vector. The DMI parameter *D* depends on the spin-wave propagation direction. This DMI term can induce the propagation-direction dependent frequency shift, therefore by measuring propagation-direction dependent frequency shift in thin film, the *interfacial* DMI can be observed. Here, asymmetry part $(\delta f_{12}-\delta f_{21})/2V_{dc}$ is correlated to the voltage controlled magnetic anisotropy (VCMA) and voltage control *interfacial* Dzyaloshinskii–Moriya Interaction However, asymmetry part because of voltage is quite negligible as shown in eq^n (4.39). It means that asymmetry part $(\delta f_{12}-\delta f_{21})/2V_{dc}$ is correlated to voltage control *interfacial* Dzyaloshinskii–Moriya Interaction. Mathematically, from eq^n (4.42) and asymmetric part of frequency shift, the voltage controlled *interfacial* Dzyaloshinskii–Moriya interaction is described as

$$VCDMI = -\left(\frac{\delta f_{21}-\delta f_{12}}{2V_{dc}}\right)\left(\frac{\gamma}{2\pi}\right)\left(\frac{\pi M_S}{\gamma k}\right) \text{ ------(4.43)}$$

In the spin wave spectroscopy, as shown in Fig.4.4, we can find the resonance frequency by measuring the scattering parameter (S). Mathematically, resonance frequency *f* is described as eq^n

(4.32). From eq^{n} (4.32) and measured resonant frequency, we can extract crystalline anisotropy (H_{cry}) and interfacial anisotropy (H_{int}) of FM.

By estimating the symmetrical and asymmetrical part of MSSW frequency shift from measured data, VCMA and VCDMI are being calculated from eq^{n} (4.41) and eq^{n} (4.43), respectively.

5 Voltage-Controlled Magnetic Anisotropy at $Fe_{1-x}Co_x$/Pd/MgO Interfaces

5.1 Introduction

The control of magnetism using voltage is attracting great attention in the field of spintronics. It has significant effects in ultrathin ferromagnetic films due to its unique physics and has enormous potential for application in high-density low-power-consumption memory. Experimental and theoretical studies of the topic exist in the literature, including work involving voltage-controlled magnetic anisotropy (VCMA) [28,29,61,62,63], the Curie temperature [64,65] exchange bias [66], the Dzyaloshinskii–Moriya interaction [67] and the exchange interaction [68-70]. Especially, high-frequency magnetization switching has contributed to a new class of VCMA-driven memory devices [37,71,72,73].

The VCMA effect is induced by an accumulation of charge at the interface of ferromagnetic materials due to an applied electric field. The accumulated charge screens the electric field in the region within a few monatomic layers of the interface. Therefore, the interface of ferromagnetic materials is very important for VCMA. The microscopic origin of the VCMA effect at the interface of ferromagnetic materials can be understood as follows. In the case of 3*d*-ferromagnetic materials such as Co, it has been experimentally reported that electric-field-induced changes of the orbital magnetic moment predominantly contribute to the VCMA effect [31]. Moreover, in the case of 5*d*-materials with proximity-induced spin polarization, such as Pt, the magnetic dipole T_z term was reported to be significant in determining the VCMA effect [32]. This term corresponds to the electric quadrupole present in atoms. This study indicates that the occupancy of the interfacial *d*-band in a ferromagnetic material is correlated to the VCMA effect. However, to the best of our knowledge, the dependency of VCMA and interfacial anisotropy energy on the occupancy of *d*-band electron orbitals of ferromagnetic material has not been studied.

In this study, we demonstrated VCMA and an interfacial anisotropy field at the $Fe_{1-x}Co_x$/Pd/MgO system. The occupancy of the *d*-band electron in the $Fe_{1-x}Co_x$ alloy can be controlled as a function of the Co fraction *x*. Because the use of Pd at the Fe(Co) interface increases VCMA[74-77], 0.2-nm-Pd (corresponding to one monatomic layer of Pd) was inserted at the $Fe_{1-x}Co_x$/MgO interface.

In the first part of this letter, we characterize the crystal and layered structure of V/Fe/$Fe_{1-x}Co_x$/Pd/MgO by using reflection high-energy electron diffraction (RHEED) and high-angle annular dark-field scanning transmission electron microscopy (HAADF-STEM), and determine the position of the Co and Pd layers by using energy-dispersive X-ray spectroscopy (EDS). In the second part, we investigated the fourfold crystal anisotropy field, the interfacial anisotropy field, and VCMA at the $Fe_{1-x}Co_x$/Pd/MgO system.

5.2 Experiment

5.2.1 Epitaxial deposition

Epitaxial multilayers of MgO (5 nm)/V (20 nm)/Fe (20 nm)/$Fe_{1-x}Co_x$ (0.3 nm)/Pd (0.2 nm)/MgO (5 nm) were deposited on a fcc-MgO(001) substrate using electron beam deposition under ultrahigh vacuum. An ultrathin $Fe_{1-x}Co_x$ layer was prepared by alternately depositing Fe and Co at room temperature onto the bcc-Fe (001) layer that was annealed at 250°C and cooled down to the room temperature in advance, as shown in Fig. 5.1 (a). The surface crystal structure of $Fe_{1-x}Co_x$ was characterized *in situ* by RHEED and shown in Fig. 5.1 (b). Similar patterns were obtained for all three regions (i.e., x = 0, 0.5, 1). It indicated that the crystal structure was independent of the Co fraction (x). A 0.2-nm-Pd layer and 5-nm-MgO were then deposited on the $Fe_{1-x}Co_x$ layer at room temperature without annealing. Subsequently, 50-nm-SiO_2 was added as an additional insulating layer by sputtering at room temperature.

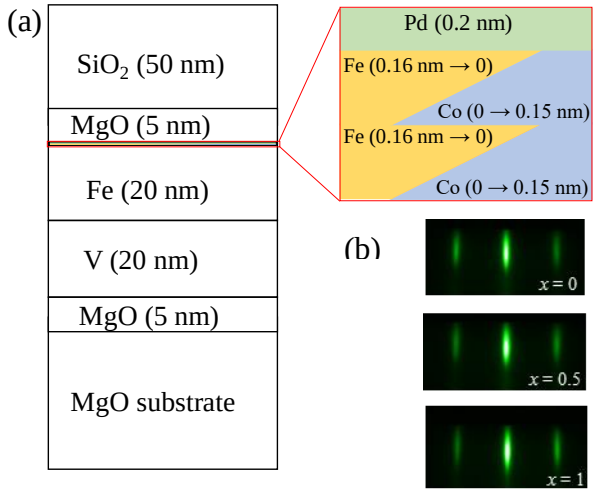

Figure 5.1. (a) Schematic of the film structure. (b) The RHEED patterns of the $Fe_{1-x}Co_x$ surface with x = 0, 0.5, 1. Electron beam//MgO [100]//Fe [110]. No change in lattice spacing suggests bcc-lattice formation in all area.

The HAADF-STEM image of the specimens taken from the x = 0 (Fe/Pd(0.2 nm)/MgO) region, Fig. 5.2(a), and that taken from the x = 1 (Fe/Co(0.3 nm)/Pd(0.2 nm)/MgO) region, Fig. 5.2(b), show layer stacking images with atomic resolution. The x=0 region shows rather a rough interface with the MgO layer. Roughness is not only caused by surface atomic steps but also significant lattice distortion as it can be seen from the atomic-resolution HAADF image. In contrast, x=1 region shows a flatter interface. In addition, Pd atomic columns are observable as brighter spots at the interface with MgO. The HAADF-STEM image (b) shows that the Pd layer possess a BCT structure (a=b=2.86 Ă, c=3.06 Ă). This BCT-Pd layer accommodates fully lattice coherency with neighboring FCC-MgO and

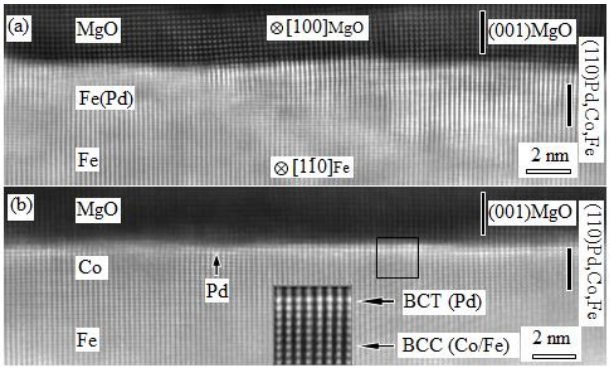

Figure 5.2 Wide area STEM image. (a) Area without Co content. (x=0). Rough interface with MgO is observed. (b) Pure Co area (x=1). Smoother interface with MgO is made. At interface, Pd atoms are observable as brighter spots.

BCC-Co/Fe layers, the orientation relationship is described as: $(110)[001]_{BCC\text{-}Co/Fe}$ // $(110)[001]_{BCT\text{-}Pd}$ // $(001)[010]_{FCC\text{-}MgO}$.

In Fig. 5.3(a, b), EDS images for x=0 and x=1 regions are shown. Diffusion of Pd into Fe layer is observed for x=0 region (Fig. 5.3(a)). From the line profile in Fig. 5.4(a), the diffusion length of

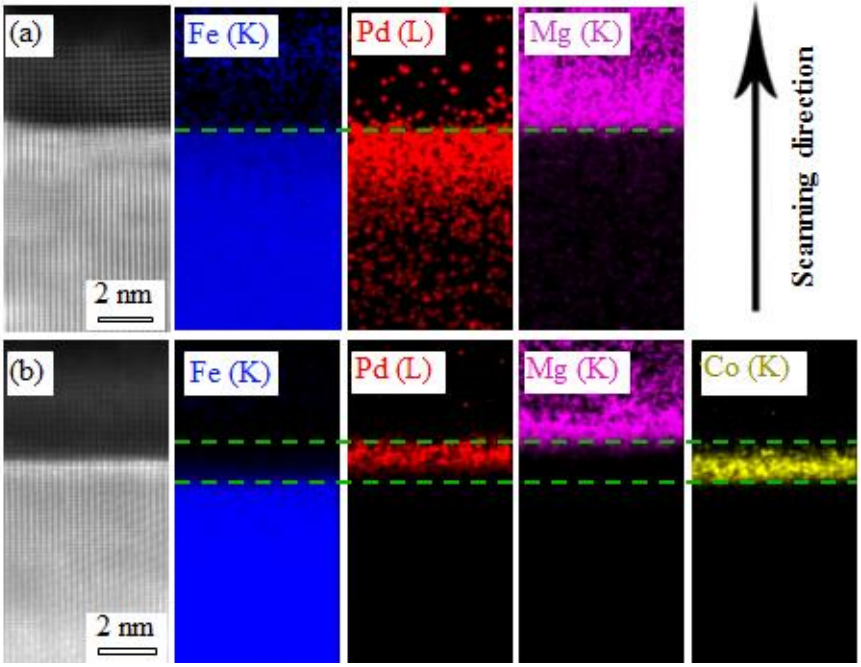

Figure 5.3. EDS images (a) For x=0 region. Diffusion of Pd into the Fe layer is observable. (b) For x=1 region. Pd layer is well separated Co layer. EDS line profile for x=0 region

Pd is estimated to be about 2 nm. Diffusion of Pd with different atomic diameter can distort the crystal lattice and rough interface.

The EDS image for the x = 1 region, Fig. 5.3 (b), shows that Pd is situated in between MgO and Co layers. Because of film roughness and the limited resolution of EDS, we cannot estimate the degree of mixing between the Pd and Co layers simply. The EDS line profile shows a 1.2 nm and 0.7 nm line width for the Co and Pd layers, respectively (Fig. 5.4(b)). These line width should be larger than the actual film thickness because of limited resolution and film roughness (0.3−0.4

nm). However, the peak positions in the concentration profiles indicate the position of the film center correctly. A distance of about 0.19 nm separates the highest peaks of the Co and Pd distribution signals. It indicates that the distance between the center positions of the Co and Pd layers is slightly smaller than the designed distance (0.24 nm). Since high-resolution HAADF-STEM images show distinct Pd atomic columns at the interface, this small deviation can be originated in the surface roughness caused by atomic steps and small physical mixing at the interface.

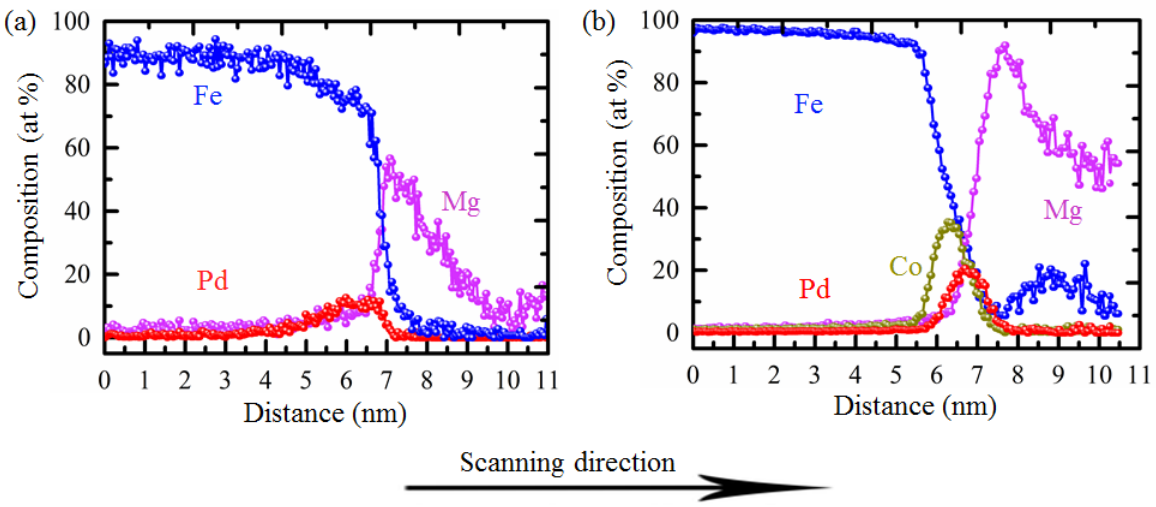

Figure 5.4. EDS line profile (a) *x*=0 region (b) *x*=1

5.2.2 Fabrication

The film was patterned into 100 × 400 μm^2 rectangles as shown in Fig. 5.10. The longer edge of the rectangle is parallel to both Fe [100] and MgO [110] directions. Micro-sized antennas and an intermediate gate were fabricated with Cr (5 nm)/Au (200 nm) by a conventional microfabrication technique using electron beam lithography and lift-off on the rectangular pattern. The antennas (short-circuited coplanar waveguides) were designed parallel to the shorter edge of the rectangular pattern. The signal line, ground line, and gap are 1, 2, and 1 μm thick, respectively. Both antennas are separated by 10 μm and a 2-μm-wide gate electrode is positioned between them. The antenna excites and detects spin-waves with a wavenumber of 1.2 μm^{-1}. A contact pad is fabricated by etching the rectangular pattern down to the Fe layer. The fabrication of device has been done in following steps. **(A) Registration (B) Wire (C) Edge (D) Hole (D) Antenna I and II**

(A) Registration

After sample deposition, cleaning of the sample was done in acetone followed by IPA in sonicator at mild vibration. After that, ZEP resist and Espacer coating were coated. Electron beam lithography was done for and the sample was developed to resist developer after that Cr/Au was deposited in an electron beam evaporator as mentioned in table 5.1. This step is for alignment to the next lithography steps.

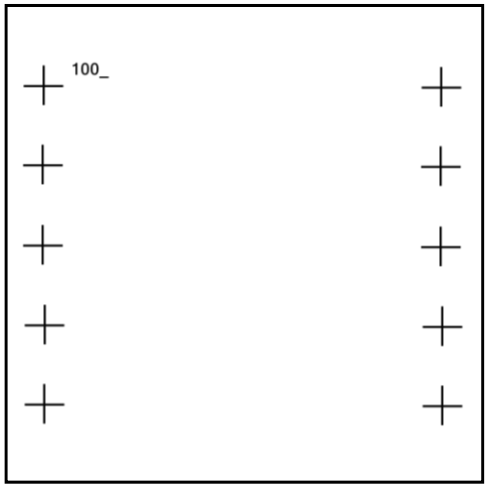

Figure 5.5. Schematic of registration layer (This is for alignment purpose).

Sample cleaning		Chemical	Time (sec)	
		Acetone	60	
		IPA	60	
Registration	ZEP resist	Cycle	Speed (rpm)	Time(sec)
		Main Cycle	4000	90
	Preheat_1	Temperature=180 °C		180
	Espacer coating	Cycle	Speed (rpm)	Time(sec)
		Main Cycle	2000	120
EB lithography		Current=1 nA, 1.6 μs/dot		
Developer lithography	Developer	DI water		90
		ZED-N50		90
		$(CH_3)_2CHCH_2C)CH_3$		30
Deposition	Cr/Au	5nm/50nm, Lift off		

Table 5.1 Fabrication steps of registration layer (allignment)

(B) Wire

After the registration step, cleaning of the sample was done in acetone followed by IPA in sonicator at mild vibration. After that, TGMR resists and Espacer coating are coated. The film was patterned into 100 × 400 μm^2 rectangles. The longer edge of the rectangle is parallel to both Fe [100] and MgO [110] directions as shown in Fig. 5.6. Electron beam lithography was done for, and the sample was developed to resist developer after that SiO_2 was sputtered as isolation as mentioned in table 5.2.

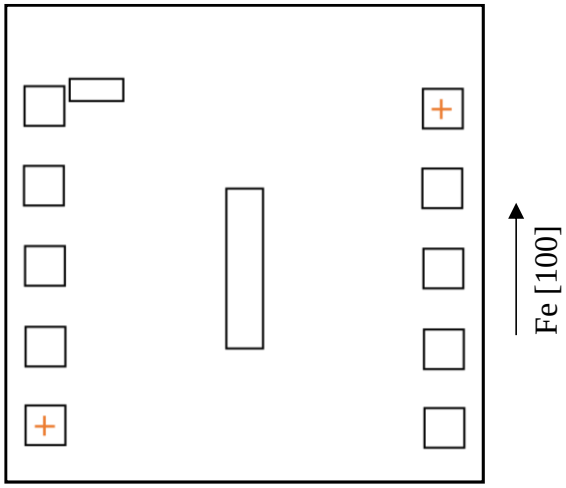

Figure 5.6. Schematic of rectangle pattern.

Sample cleaning		Chemical	Time (sec)	
		Acetone	60	
		IPA	60	
	TGMR coating	Cycle	Speed (rpm)	Time(sec)
		Main Cycle	4000	90
	Preheat_1	Temperature=130 °C		90
	Espacer coating	Cycle	Speed (rpm)	Time(sec)
		Main Cycle	2000	120
EB lithography		Current=300 pA, 0.4 μs/dot		

Developer lithography	Developer	DI water		90
		Baking	120 °C	90
		NMD_3		80
		DI		30
Dry etching	Ar-ion milling	Base pressure: $2\times10^{-4} - 7\times10^{-4}$ Pa	Argon flow rate=8 sccm	
Isolation	SiO_2 deposition		Argon flow rate=20 sccm, Process pressure=0.2 Pa Thickness= 20 nm	
Lift off		1min sonication × 10-15 time under microscopic observation		
SiO_2 sputtering	SiO_2 deposition	Base pressure: $2\times10^{-4} - 7\times10^{-4}$ Pa	Argon flow rate=20 sccm, Process pressure=0.2 Pa Thickness= 45 nm	

Table 5.2 Fabrication steps of rectangle pattern

(C) Edge

After pattering the sample, cleaning of the sample was done in acetone followed by IPA in sonicator at mild vibration. After that, ZEP resist, and Espacer were coated, and Electron beam lithography was done, and the sample was developed in resist developer, the edge of the rectangle was covered by Cr/Au as shown in Fig. 5.7 and mentioned in table 5.3.

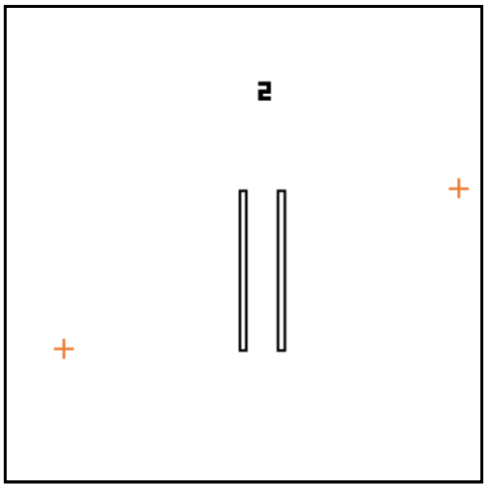

Figure 5.7. Schematic of edge covering.

Sample cleaning		Chemical	Time (sec)	
		Acetone	60	
		IPA	60	
Registration	ZEP resist	Cycle	Speed (rpm)	Time(sec)
		Main Cycle	4000	90
	Preheat_1	Temperature=180 °C		180
	Espacer coating	Cycle	Speed (rpm)	Time(sec)
		Main Cycle	2000	120
EB lithography		Current=1 nA, 1.6 μs/dot		
Developer lithography	Developer	DI water		90
		ZED-N50		90

		$(CH_3)_2CHCH_2C)CH_3$	30
Deposition	Cr/Au	Cr-5nm, Au-200 nm	
Lift off		ZD-Mac, 100 Hz sonication, 60 sec	

Table 5.3 Fabrication steps of Wire layer

(C) Hole

After edge steps, cleaning of the sample has been done in acetone and IPA in sonicator at mild vibration, respectively. After that, ZEP resist and Espacer were coated, and Electron beam lithography was done for and the sample was developed to resist developer shown in Fig. 5.8(a), contact on the patterned rectangle was etched as shown in Fig. 5.8(b) and mentioned in table 5.4.

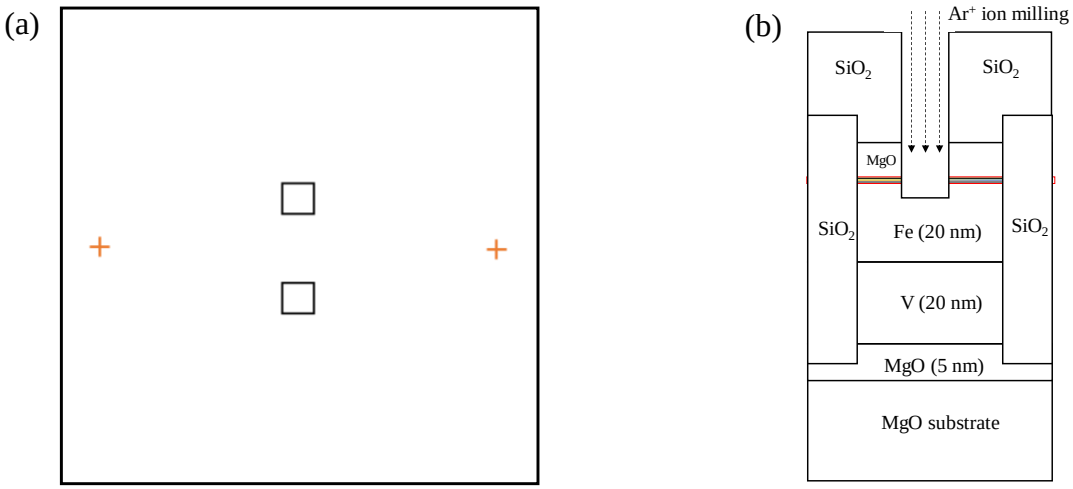

Figure 5.8. Schematic of contacting hole.

Sample cleaning		Chemical	Time (sec)	
		Acetone	60	
		IPA	60	
Registration	ZEP resist	Cycle	Speed (rpm)	Time(sec)
		Main Cycle	4000	90
	Preheat_1	Temperature=180 °C		180
	Espacer coating	Cycle	Speed (rpm)	Time(sec)
		Main Cycle	2000	120
EB lithography		Current=1 nA, 1.6 μs/dot		
Developer lithography	Developer	DI water		90
		ZED-N50		90
		$(CH_3)_2CHCH_2C)CH_3$		30
Dry etching	Ar-ion milling	Base pressure: $2\times10^{-4} - 7\times10^{-4}$ Pa	Argon flow rate=8 sccm	
Lift off		ZD-MAC, 100 Hz, 1min		

Table 5.4 Fabrication steps of contacting Hole.

(D) Antenna I and II

After edge steps, cleaning of the sample has been done in acetone and IPA in sonicator at mild vibration, respectively. After that, ZEP resist and Espacer were coated and electron beam lithography was done and the sample was developed to resist developer. The Cr (5 nm)/Au (200 nm) was deposited and lift off as shown in Fig. 5.9(a) and contact pad are shown in Fig. 5.9(b) and mentioned in table 5.5.

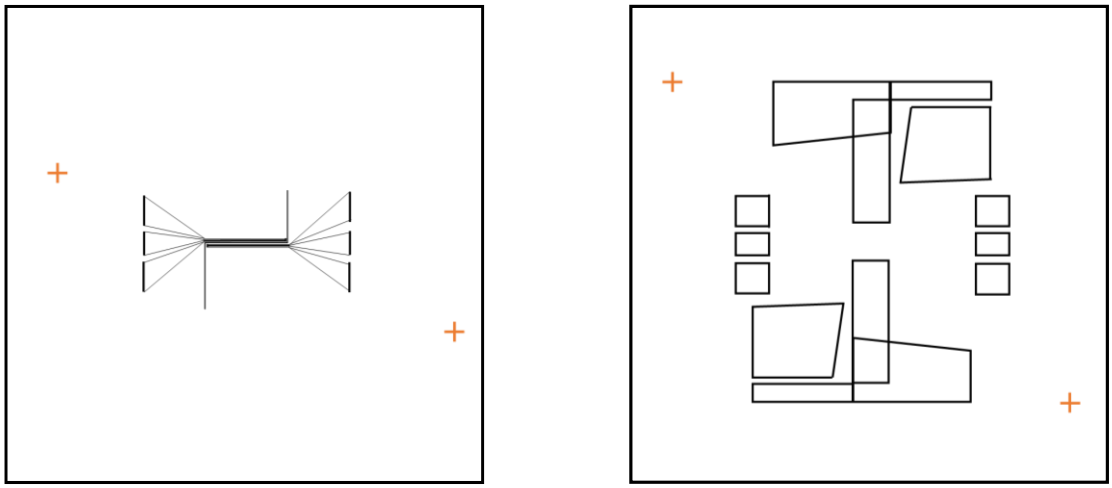

Figure 5.9. Schematic of antenna design.

Sample cleaning		Chemical	Time (sec)	
		Acetone	60	
		IPA	60	
Registration	ZEP resist	Cycle	Speed (rpm)	Time(sec)
		Main Cycle	4000	90
	Preheat_1	Temperature=180 °C		180

	Espacer coating	Cycle	Speed (rpm)	Time(sec)
		Main Cycle	2000	120
EB lithography		Current=1 nA, 1.6 μs/dot		
Developer lithography	Developer	DI water		90
		ZED-N50		90
		$(CH_3)_2CHCH_2C)CH_3$		30
Deposition	Cr/Au	Cr-5nm, Au-200 nm		
Lift off		ZD-Mac, 100 Hz sonication, 60 sec		

Table 5.5 Fabrication steps of Wire layer

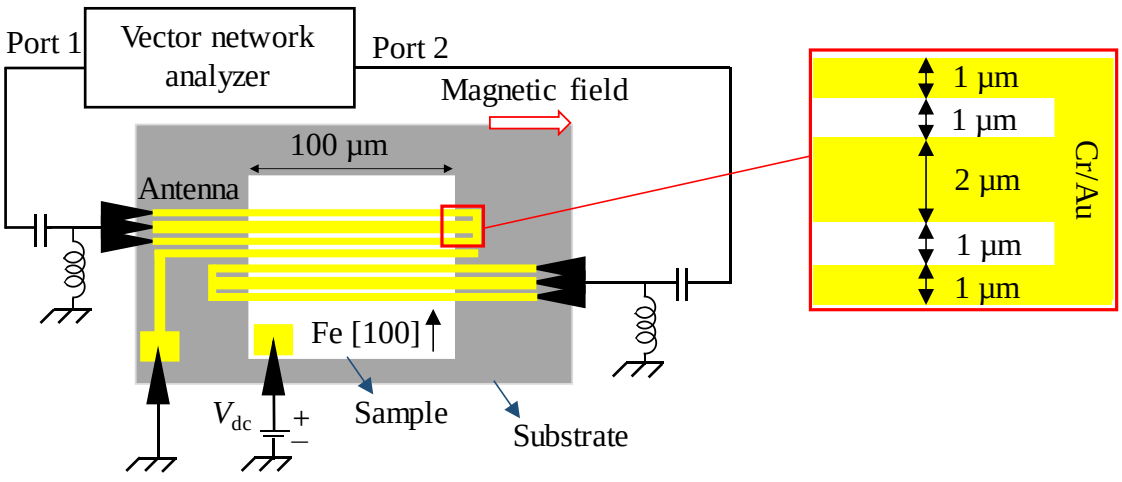

Figure 5.10. Schematic of the device structure and measurement setup. The black arrow shows the Fe [100] direction. The yellow color shows the antenna and gated contact pad. The black color shows the ground-signal-ground (GSG) probes. A dc voltage (V_{dc}) is applied to the sample.

The device was fabricated into 100 × 400 μm^2 rectangles. A dc bias voltage (V_{dc}) is applied between the contact pad and the intermediate gate. The bias-tee was inserted between a vector network analyzer (VNA) and the antenna. Figure 5.10 shows a schematic of the spin-wave device and measurement setup. We applied a static magnetic field in the in-plane direction (H_{ext}). Magnetostatic surface spin-waves (MSSWs) were excited by applying a radio frequency (rf) signal of −15 dBm (32 μW). MSSW is localized along the thickness of the ferromagnetic material when the ferromagnetic layer thickness is quite thick. In our case, spin-wave penetration depth ($\lambda \propto 1/k$, k=1.2 μm^{-1}) is around a few micrometers and is much larger than that of ferromagnetic layer thickness t_{Fe} of ~20 nm. The MSSW flows throughout the ferromagnetic layer (20-nm-Fe & 0.30-nm-FeCo) as shown in Fig. 5.11. The scattering (S) is the collective response of FM, was measured by the VNA. The resonant

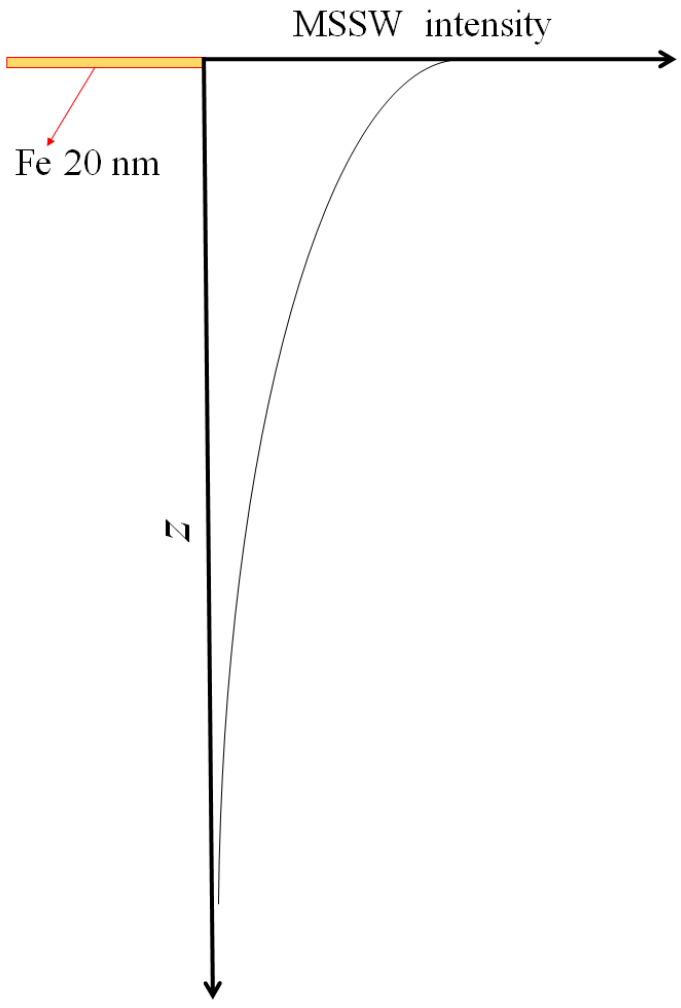

Figure 5.11 Schematic of "MSSW intensity versus FM thickness (z axis)" is shown.

frequency of the MSSW was extracted from the $|S'_{11}|$ $[S'_{11} = S_{11}(H_{ext}) - S_{11}(2700\,\text{Oe})]$ signals (Fig. 6.12(a)). The $|S'_{11}|$ signal for the x = 1 (Fe/Co(0.3 nm)/Pd(0.2 nm)/MgO) layer as measured by the VNA is shown in the inset of Fig. 5.12(a). The $S_{11}(2700\,\text{Oe})$ signal is considered a background signal. Similarly, $|S'_{11}|$ signals were measured in $Fe_{1-x}Co_x$/Pd for various x values.

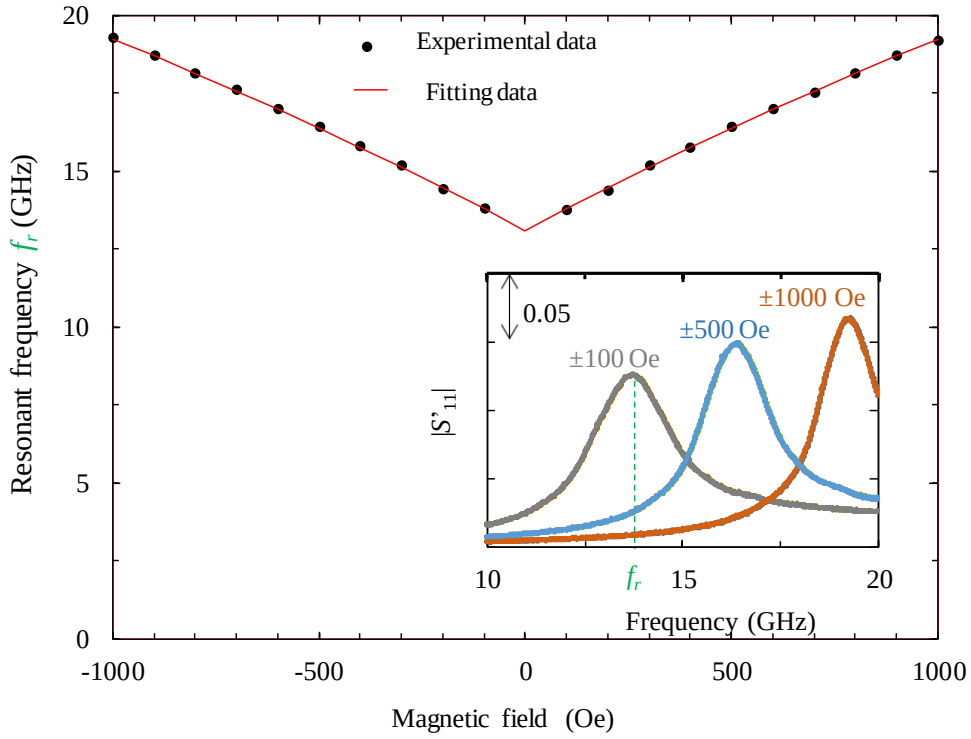

Figure 5.12. The typical resonant frequencies of MSSW of Fe/$Fe_{1-x}Co_x$/Pd/MgO with x = 1 (Fe/Co(0.3 nm)/Pd(0.2 nm)/MgO) under an in-plane magnetic field (H_{ext}).

The following eq^n (5.1) describes the resonant frequency. The black dot and red line show the experimental and fitting data using eq^n (5.1), respectively. Similarly, $|S'_{11}|$ signals were measured in $Fe_{1-x}Co_x$/Pd for various x values.

5.3 Result and discussion

The following equation describes the resonant frequency. (From eq^n (4.33))

$$f = -\frac{\gamma}{2\pi}\sqrt{\left(\left|H_{ext}\right| + H_{cry}\right)\left(\left|H_{ext}\right| + M_S + H_{cry} - H_{int}\right) + \frac{M_S}{4}\left(M_S - H_{int}\right)\left(1 - \exp\left(-2\left|k\right|t_{Fe}\right)\right)} \quad (5.1)$$

where $\gamma/2\pi$ (-2.94×10^{10} T^{-1} s^{-1}) is the gyromagnetic ratio, $\mu_0 M_s$ (2.16 T) (The MSSW flows throughout the ferromagnetic layer (20-nm-Fe & 0.30-nm-FeCo) as shown in Fig. 5.11. We employ ultrathin FeCo layer on 20 nm Fe. Because Co thickness is at most 1.5% in the ferromagnetic slab, we can use M_s value of Fe) is the saturation magnetization, k (1.2 μm^{-1}) is the wavenumber (estimated from antenna design), and t_{Fe} (20 nm) is the thickness of the bulk Fe layer. Here, H_{int} represents the interfacial magnetic anisotropy field and H_{cry} is the fourfold crystal anisotropy field of Fe/Fe$_{1-x}$Co$_x$/Pd. The values of H_{cry} and H_{int} are estimated by a least mean-square-error method, as shown in Fig. 5.13. The value of H_{cry} is 685 ±12 Oe, which is similar to the fourfold anisotropy field of bulk Fe, and the interfacial anisotropy field H_{int} is almost the same throughout the sample. It means that the interfacial anisotropy energy of the system is almost unchanged with the Co fraction x at the Fe/Fe$_{1-x}$Co$_x$/Pd/MgO interface. The dc bias voltage (V_{dc}) shifts Re[S_{21} (0 V)] (shown in Fig. 5.14(a)) by ΔRe[S_{21}] = Re[$S_{21}(V_{dc})$] – Re[S_{21}(0 V)]. It can be easily fitted as $\Delta \mathrm{Re}[S_{21}] = -\delta f_{21} \times d\,\mathrm{Re}[S_{21}(0\,\mathrm{V})]/df$. The δf_{21} represents the voltage-induced MSSW frequency shift, and it can be achieved by a least mean-square-error method. The experimental and fitted $\Delta \mathrm{Re}[S_{21}(4\,\mathrm{V})]$ in x = 1 (Fe/Co(0.3 nm)/Pd(0.2 nm)/MgO) are shown in Fig. 5.14(b) inset. Similarly, we have estimated δf_{12} from the $\mathrm{Re}[S_{12}]$ signal. The δf_{12} and δf_{21} versus bias voltage are shown in Fig. 5.14(b) in the x = 1 (Co/Pd/MgO) region. The slope of the linear fitting in Fig. 5.1(b) represents the voltage-induced MSSW frequency shifts per volt $\delta f_{12}/V_{dc}$ and $\delta f_{21}/V_{dc}$ in the x = 1 (Fe/Co(0.3 nm)/Pd(0.2 nm)/MgO) region. Similarly, $\delta f_{12}/V_{dc}$ and $\delta f_{21}/V_{dc}$ are determined in the

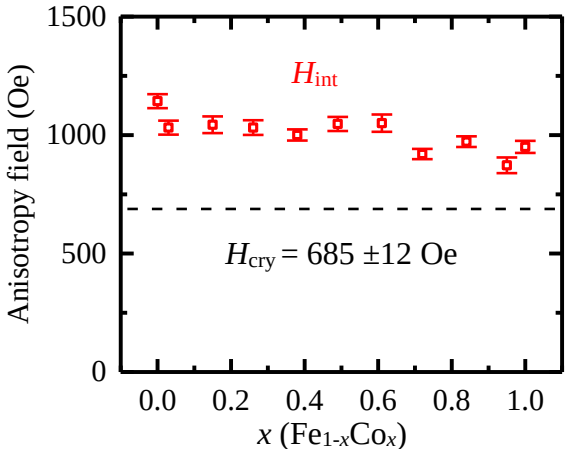

Figure 5.13. Interfacial (H_{int}) and crystalline (H_{cry}) magnetic field of the Fe/Fe$_{1-x}$Co$_x$/Pd. system.

$Fe_{1-x}Co_x$/Pd/MgO alloy. The symmetry terms $(\delta f_{12}+\delta f_{21})/2V_{dc}$ are correlated to VCMA shown in eq^n (5.2).

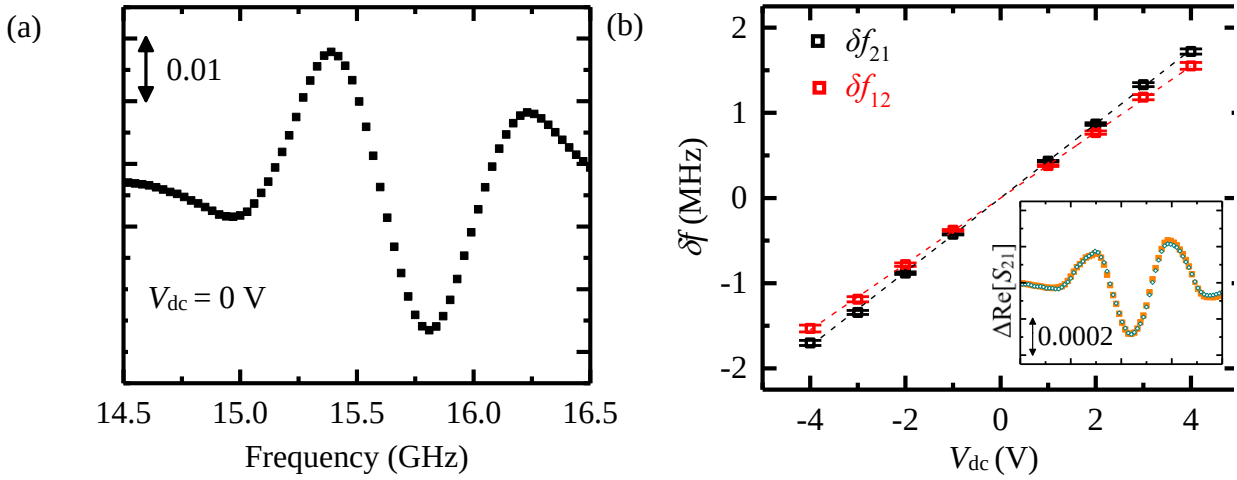

Figure 5.14. (a) Typical propagating spin wave signal. This is the real part of the MSSW signal without any bias voltage. (b) The voltage-induced resonant frequency shift of the propagating spin-waves(δf). The black (red) dots show the frequency change of Re[S_{21}] (Re[S_{12}]). The black (red) lines are fitting lines for the frequency shifts (δf_{12}, δf_{21}). The inset shows experimental (blue) and fitting data (red). The *x* axis of inset is indicating as frequency axis from 14.5 GHz to 16.5 GHz. The error bar indicates the standard deviation in the frequency shift obtained from the root mean-square-error. All the data in this figure correspond to the sample of $Fe_{1-x}Co_x$/Pd/MgO with x = 1, i.e., Fe/Co(0.3 nm)/Pd(0.2 nm)/MgO.

Mathematically, these are expressed by the following equation. (From eq^n (4.41))

$$\mathrm{VCMA} = \frac{-f\left(\frac{\delta f_{21}+\delta f_{12}}{2V_{dc}}\right) M_S\, t_{Fe}}{\left(\frac{\gamma}{2\pi}\right)^2 \left(|H_{ext}| + H_{cry} + \frac{M_S}{4}\left(1-e^{-2|k|t_{Fe}}\right)\right) E_{MgO}} \quad \text{----------(5.2)}$$

where, E_{MgO} represents the perpendicular electric field through the 5-nm-MgO. We modeled the sample as two parallel-plate capacitors a 50-nm-SiO_2 (ε= 3.9) and a 5-nm-MgO (ε = 9.6).

We observed the directional symmetry in the MSSW frequency shift δf. The MSSW frequency shift δf is because of VCMA. The δf_{12} and δf_{21} terms are shown in Fig. 5.14(b). They show a linear dependency on the voltage. The effect shows neither hysteresis nor aging effect. This means because the behavior is not due to magneto-ionic control[30,77,78]. The VCMA at $Fe_{1-x}Co_x$/Pd/MgO interface is estimated and shown in Fig. 5.15. It shows that VCMA enhances as the Co fraction x increases in the alloy. We achieved the VCMA around 250 fJ/Vm at Co/Pd/MgO interface.

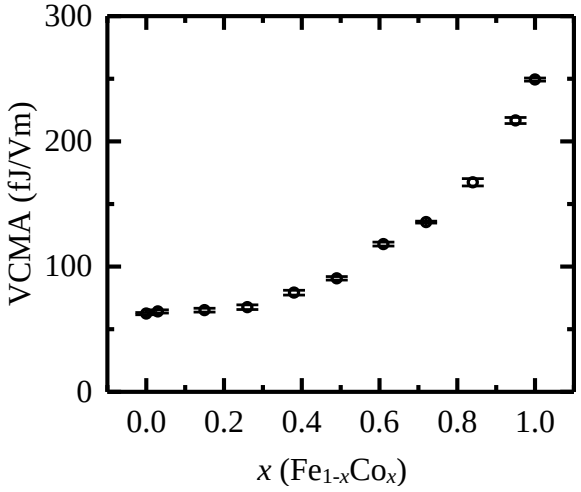

Figure 5.15. Voltage-controlled magnetic anisotropy at the $Fe_{1-x}Co_x$/Pd/MgO system.

The impact of Fe and Co on the composition dependence of VCMA at the $Fe_{1-x}Co_x$/Pd/MgO system was studied. VCMA increases around 300% from x=0 (Fe/Pd/MgO) region to x=1 (Co/Pd/MgO) region, while the interfacial anisotropy energy is changing around 30%. These two observations suggest that the origin of VCMA and the origin of the interfacial anisotropy are not the same. The STEM and EDS image show that in x = 1 (Co/Pd/MgO) region, Pd atoms are situated between MgO and Co layer, while we are getting larger VCMA value 250 fJ/Vm. From the observation of this experiment, there can be two possible origins of the large VCMA. One is x dependence on electron occupancy in the d orbital states in $Fe_{1-x}Co_x$ and the other is the existence of Pd atoms at the interface for x=1. It is difficult to determine the origin of the VCMA only with the experimental results; first-principle calculations would be helpful to study the origin of the observed behavior.

5.4 Conclusion

This is the first study to demonstrate a well-defined interfacial structure which alters *d*-band electron occupancy without changing their crystal. We investigate the VCMA and H_{int} at fully epitaxially grown V/Fe/$Fe_{1-x}Co_x$/Pd/MgO system. VCMA increases around 300% from x=0 (Fe/Pd/MgO) region to x=1 (Co/Pd/MgO) region. However, H_{int} is 30% changing throughout the sample. Therefore, VCMA and interfacial anisotropy energy are not directly correlated. A high VCMA of 250 fJ/Vm is achieved in the Co/Pd/MgO region, where Pd atoms are well situated in between MgO and Co layer.

6 Voltage Control of *interfacial* Dzyaloshinskii–Moriya Interaction at $Fe_{1-x}Co_x$/Pd/MgO system

6.1 Introduction

Broken inversion symmetry and spin-orbit interaction increase the *interfacial* Dzyaloshinskii–Moriya Interaction. On different bias voltage, Magnetostatic surface spin wave shows different propagation properties in the opposite direction in V/Fe/$Fe_{1-x}Co_x$/Pd/MgO system.

6.2 Experiment

6.2.1 Epitaxial deposition

Epitaxial multilayers of MgO (5 nm)/V (20 nm)/Fe (20 nm)/$Fe_{1-x}Co_x$ (0.3 nm)/Pd (0.2 nm)/MgO (5 nm) were deposited on a fcc-MgO(001) substrate using electron beam deposition under ultrahigh vacuum. The ultrathin $Fe_{1-x}Co_x$ layer was prepared by an alternate deposition of Fe one monolayer in wedge shape and one monolayer Co was in opposite wedge shape at room temperature onto the body-centered-cubic-(BCC)-Fe-(001) layer, which was, prior to the deposition, annealed at 250 °C and cooled down to room temperature. After that, similarly, we deposited again Fe one monolayer in a wedge shape and one monolayer Co was in opposite wedge shape. Schematic diagram of the deposited film is shown in Fig. 6.1(a). The surface crystal structure of $Fe_{1-x}Co_x$ was characterized *in situ* by RHEED and shown in Fig. 6.1 (b). Similar patterns were obtained for all three regions (i.e., x = 0, 0.5, 1). This indicated that the crystal structure was independent of the Co fraction (x). A 0.2-nm-Pd layer and 5-nm-MgO were then deposited on the $Fe_{1-x}Co_x$ layer at room temperature without annealing. Subsequently, 50-nm-SiO_2 was added as an additional insulating layer by sputtering at room temperature. We characterize the crystal and layered structure of V/Fe/$Fe_{1-x}Co_x$/Pd/MgO using reflection high-energy electron diffraction (RHEED) and high-angle annular-dark-field scanning transmission electron microscopy (HAADF-STEM), and determine the position of the Co and Pd layers using energy-dispersive X-ray spectroscopy (EDS) as shown in last chapter 5. (Fig 5.2-5.4)

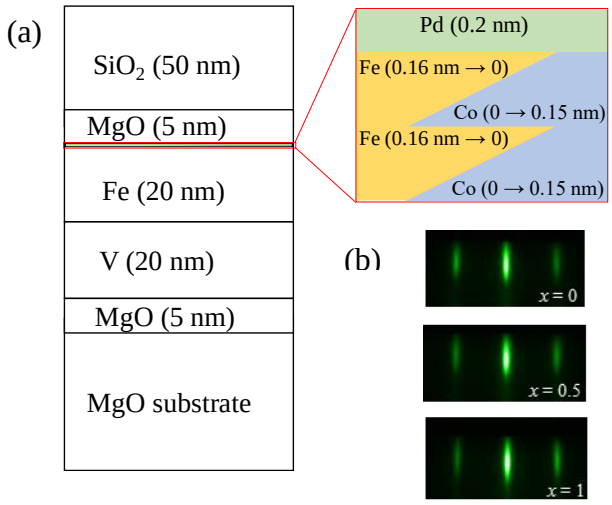

Figure 6.1**. (a)** Schematic of the film structure. **(b)** RHEED patterns of the $Fe_{1-x}Co_x$ surface for x = 0, 0.5, and 1; electron-beam//MgO [100]//Fe [110]; no change in lattice spacing was observed, which suggests a BCC-lattice formation in all regions. (shown in last chapter 5, Fig 5.1)

6.2.2 Fabrication

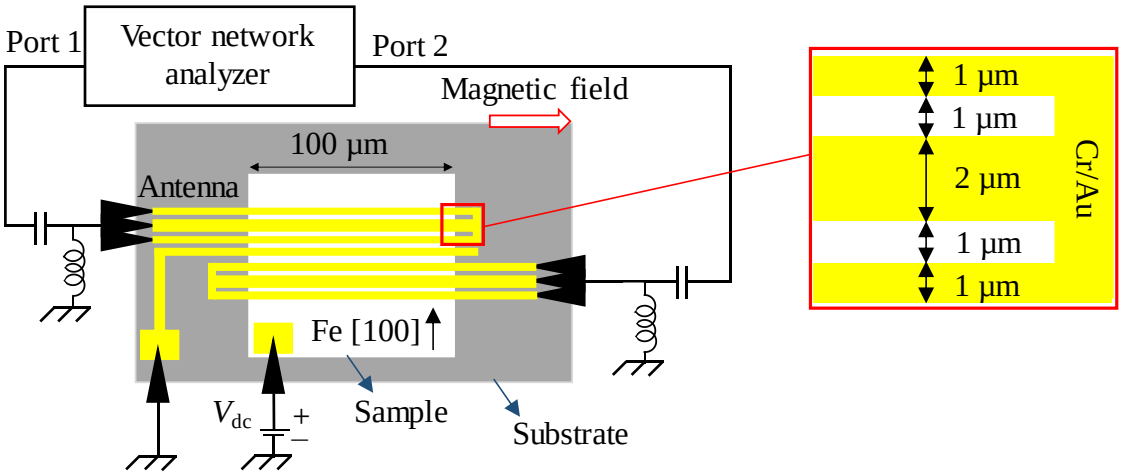

Figure 6.2 schematic of device. (shown in last chapter 5, Fig 5.10)

The film was patterned into 100 × 400 µm^2 rectangles. The longer edge of the rectangle is parallel to both Fe [100] and MgO [110] directions. Micro-sized antennas and an intermediate gate were fabricated with Cr (5 nm)/Au (200 nm) by a conventional microfabrication technique using electron beam lithography and lift-off on the rectangular pattern. The antennas (short-circuited coplanar waveguides) were designed parallel to the shorter edge of the rectangular pattern. The signal line, ground line, and gap are 1, 2, and 1 µm thick, respectively. Both antennas are separated

by 10 μm and a 2-μm-wide gate electrode is positioned between them. The antenna excites and detects spin-waves with a wavenumber of 1.2 μm^{-1}. A contact pad is fabricated by etching the rectangular pattern down to the Fe layer. Fabrication steps are mentioned in last chapter 5. (Fig 5.5-5.11)

6.2.3 Measurement

A dc bias voltage (V_{dc}) is applied between the contact pad and the intermediate gate. The bias-tee was inserted between a vector network analyzer (VNA) and the antenna. Figure 6.2 shows a schematic of the spin-wave device and measurement setup. We applied a static magnetic field in the in-plane direction (H_{ext}). Magnetostatic surface spin-waves (MSSWs) were excited by applying a radio frequency (rf) signal of −15 dBm (32 μW). The VNA measured the scattering (S) parameter. The resonant frequency of the MSSW was extracted from the $|S'_{11}|$ $[S'_{11} = S_{11}(H_{ext}) - S_{11}(2700\,\text{Oe})]$ signals (Fig. 6.3).

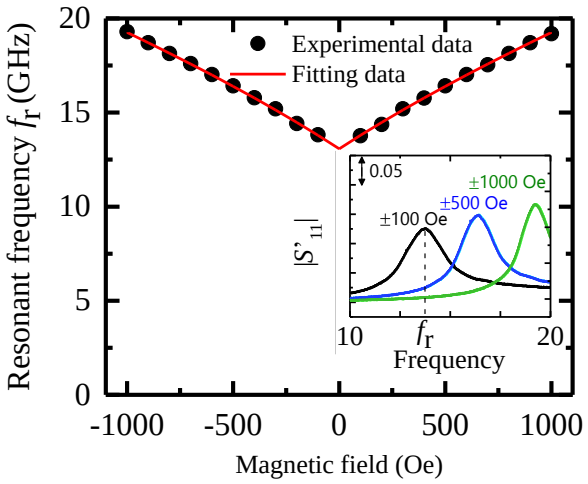

Figure 6.3 The typical resonant frequencies of MSSW of Fe/Fe$_{1-x}$Co$_x$/Pd/MgO with x = 1 (Fe/Co(0.3 nm)/Pd(0.2 nm)/MgO) under an in-plane magnetic field (H_{ext}). The black dot and red line show the experimental and fitting data using eq^n. 6.1, respectively

The $|S'_{11}|$ signal for the x = 1 (Fe/Co(0.3 nm)/Pd(0.2 nm)/MgO) layer as measured by the VNA is shown in the inset of Fig. 6.3. The $S_{11}(2700\,\text{Oe})$ signal is considered a background signal. Similarly, $|S'_{11}|$ signals were measured in Fe$_{1-x}$Co$_x$/Pd for various x values. The resonant frequency is described by the following equation (From eq^n (4.42))

$$f = -\frac{\gamma}{2\pi}\sqrt{\left(|H_{ext}| + H_{cry}\right)\left(|H_{ext}| + M_S + H_{cry} - H_{int}\right) + \frac{M_S}{4}\left(M_S - H_{int}\right)\left(1 - \exp\left(-2|k|t_{Fe}\right)\right)} - \frac{\gamma}{\pi M_S}Dk \quad \text{----(7.1)}$$

where, $\gamma/2\pi$ (−2.94 ×10^{10} T^{-1} s^{-1}) is the gyromagnetic ratio, $\mu_0 M_s$ (2.16 T) is the saturation magnetization, k (1.2 μm^{-1}) is the wavenumber (estimated from antenna design), and t_{Fe} (20 nm)

is the thickness of the bulk Fe layer. Here, H_{int} represents the interfacial magnetic anisotropy field and H_{cry} is the fourfold crystal anisotropy field of Fe/Fe$_{1-x}$Co$_x$/Pd. The values of H_{cry} and H_{int} are estimated by a least mean-square-error method. The value of H_{cry} is 685 ±12 Oe, which is similar to the fourfold anisotropy field of bulk Fe, and the interfacial anisotropy field H_{int} is almost the same throughout the sample shown in last chapter 5, Fig. 5.13. This means that the interfacial anisotropy energy of the system is almost unchanged with the Co fraction x at the Fe/Fe$_{1-x}$Co$_x$/Pd/MgO interface. The last term is because of *interfacial* Dzyaloshinskii–Moriya Interaction (DMI). It depends on k direction. The signal $|S'_{11}|$ which includes MSSW excitation for $\pm k$ but there is no splitting observed in the peak of $|S'_{11}|$ the signal's peak as shown in Fig. 6.3(a) inset. Same resonant frequency is observed in $S_{21}(+k)$ and $S_{12}(-k)$ signal. Therefore, the D value is estimated that is lower than resolution 0.5 mJ/m^2.

6.3 Result and discussion

Figure 6.4(a) shows the real part of the propagating spin-wave ($\mathrm{Re}[S_{21}]$) under H_{ext} = 400 Oe in x = 1 (Fe/Co(0.3 nm)/Pd(0.2 nm)/MgO). The dc bias voltage (V_{dc}) shifts Re[S_{21} (0 V)] by $\Delta\mathrm{Re}[S_{21}] = \mathrm{Re}[S_{21}(V_{dc})] - \mathrm{Re}[S_{21}(0\ \mathrm{V})]$. It can be easily fitted as $\Delta\,\mathrm{Re}[S_{21}] = -\delta f_{21} \times d\,\mathrm{Re}[S_{21}(0\,\mathrm{V})]/df$. The δf_{21} represents the voltage-induced MSSW frequency shift and it can be achieved by a least mean-square-error method. The experimental and fitted $\Delta\,\mathrm{Re}[S_{21}(4\,\mathrm{V})]$ in x = 1 (Fe/Co(0.3 nm)/Pd(0.2 nm)/MgO) are shown in Fig. 6.4(b)inset. Similarly, we have estimated δf_{12} from the $\mathrm{Re}[S_{12}]$ signal. The δf_{12} and δf_{21} versus bias voltage are shown in Fig. 5 (b) in the x = 1 (Co/Pd/MgO) region. The slope of the linear fitting in Fig. 6.4(b) represents the voltage-induced MSSW frequency shifts per volt $\delta f_{12}/V_{dc}$ and $\delta f_{21}/V_{dc}$ in the x = 1 (Fe/Co(0.3 nm)/Pd(0.2 nm)/MgO) region. Similarly, $\delta f_{12}/V_{dc}$ and $\delta f_{21}/V_{dc}$ are determined in the Fe$_{1-x}$Co$_x$/Pd/MgO alloy.

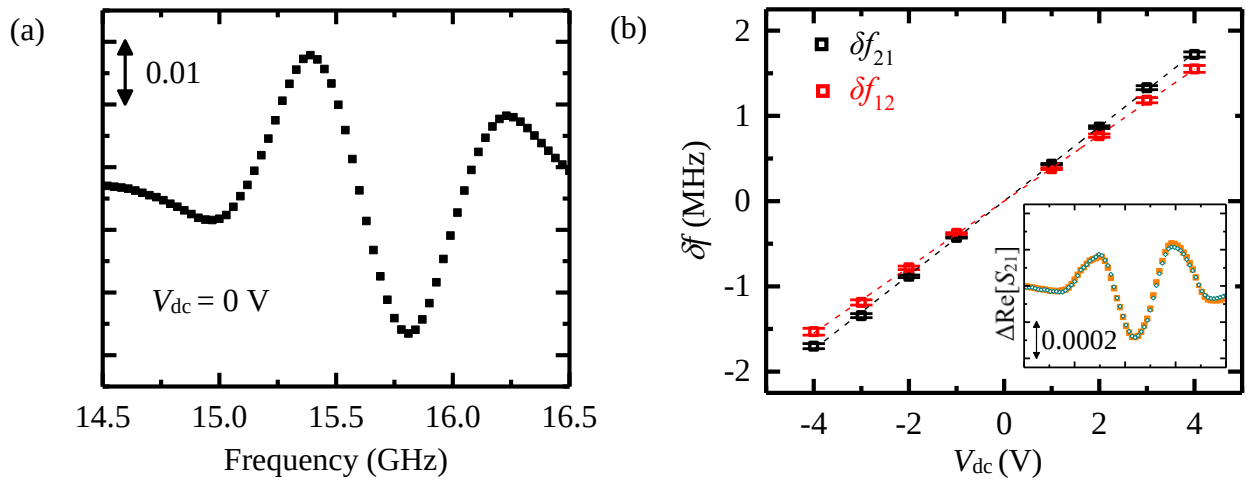

Figure 6.4. (a)Typical propagating spin wave signal. This is the real part of the MSSW signal without any bias voltage. **(b)** Voltage-induced resonant frequency shift of the propagating spin-waves(δf). The black (red) rectangular dots show the frequency change of Re[S_{21}] (Re[S_{12}]). The black (red) lines are fitting lines for the frequency shifts (δf_{12}, δf_{21}). The error bar indicates the standard deviation in the frequency shift obtained from the root mean-square-error. The inset shows experimental (solid rectangular yellow) and fitting data (open diamond green). The *x* axis of inset is indicating as frequency axis from 14.5 GHz to 16.5 GHz. All the data in this figure correspond to the sample of $Fe_{1-x}Co_x$/Pd/MgO with x = 1, i.e., Fe/Co(0.3 nm)/Pd(0.2 nm)/MgO.

The symmetry terms $(\delta f_{12}+\delta f_{21})/2V_{dc}$ (site our paper) and asymmetry part $(\delta f_{12}-\delta f_{21})/2V_{dc}$ are correlated to voltage controlled magnetic anisotropy (VCMA) and voltage control *interfacial* Dzyaloshinskii–Moriya Interaction (VCDMI) (Eq[n]. 6.2) Mathematically, VCDMI is expressed by the following equation (From eq[n] (4.43)).

$$\text{VCDMI} = -\left(\frac{\delta f_{21}-\delta f_{12}}{2V_{dc}}\right)\left(\frac{\gamma}{2\pi}\right)\left(\frac{\pi M_S}{\gamma k}\right) \qquad (6.2)$$

where E_{MgO} represents the perpendicular electric field in the 5-nm-MgO. We modeled the sample as two parallel-plate capacitors a 50-nm-SiO_2 (ε= 3.9) and a 5-nm-MgO (ε = 9.6).

We observed the directional symmetry in the MSSW frequency shift δf. The MSSW frequency shift δf is because of VCMA. The δf_{12} and δf_{21} terms are shown in Fig. 6.4(b). They show a linear dependency on the voltage. The effect shows neither hysteresis nor aging effect. This means because the behavior is not due to magneto-ionic control. The VCMA at $Fe_{1-x}Co_x$/Pd/MgO interface is estimated in the last chapter in Fig. 5.15. It shows that VCMA enhances as the Co

fraction *x* increases in the alloy. We achieved the VCMA around 250 fJ/Vm at Co/Pd/MgO interface. The VCDMI at $Fe_{1-x}Co_x$/Pd/MgO interface is estimated in Fig. 6.5. It shows that VCDMI does not enhance as the Co fraction *x* increases in the alloy. We achieved the VCDMI around 70 fJ/Vm at Co/Pd/MgO interface

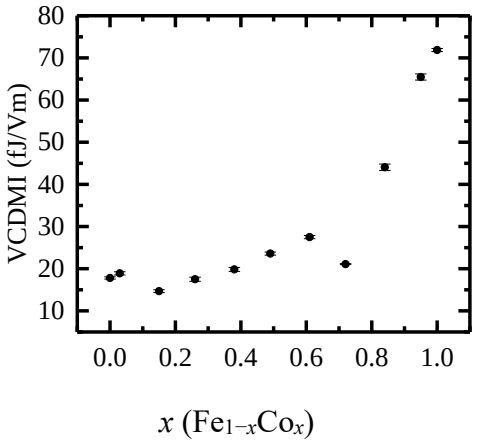

Figure 6.5 VCDMI in the $Fe_{1-x}Co_x$/Pd/MgO

The VCMA and the VCDMI increased by approximately 300% with the increase of *x* from 0 (Fe/Pd/MgO) to 1 (Co/Pd/MgO); however, H_{int} varied throughout the sample up to approximately 30%. The VCMA value increases continuously with Co fraction (*x*) as shown in the last chapter in Fig. 5.15, while VCDMI value is not continuously increasing with Co fraction (*x*) as shown in Fig. 6.5. Therefore, the VCMA, the VCDMI and interfacial anisotropy energy were not directly correlated. A high VCMA of 250 fJ/Vm and VCDMI of 70 fJ/Vm were achieved in the Co/Pd/MgO region.

6.4 Conclusion

This is the first study to demonstrate a well-defined interfacial structure which alters *d*-band electron occupancy without changing their crystal structure. We demonstrated Voltage controlled *interfacial* Dzyaloshinskii-Moriya interaction at $Fe_{1-x}Co_x$/Pd/MgO system by spin spectroscopy method. The propagation-direction dependent voltage-induced frequency shift. We estimated experimental results. However, it is challenging to determine the origin of the VCMA and VCDMI only with the experimental results; first-principle calculations would be helpful to study the origin of the observed behavior.

7 Summary and Conclusion

7.1 Summary

In the first part of the study, to investigate VCMA on polycrystalline FM layer, we deposited Ta/Ru/Ta/CoFeB/MgO/CoFeB system on a Si/SiO_2 substrate in a magnetron sputter system. The magnetic tunnel junction was fabricated with 10 μm^2 junction area in a hexagonal shape with conventional microfabrication technique with photolithography and with Ar-ion milling on this deposited sample. Samples have been annealed at different temperatures after microfabrication for 1 hour. The boron (B) diffuses in the Ta layer during annealing time and CoFeB forms a polycrystalline structure on MgO(001). The TMR measurements were carried out using a conventional two-terminal technique in the magnetic field. We observed that the magnetization of the amorphous ferromagnetic layer is changing abruptly under a perpendicular magnetic field in the unannealed MTJ. In the 350 $^{\circ}$C annealed sample, there is leakage either at junction boundary or in MgO barrier. Because of these reasons, quantitative evaluation of VCMA of both samples is not possible. Between 200 $^{\circ}$C to 300 $^{\circ}$C annealing, this work shows that maximum VCMA and maximum TMR ratio of Ta/CoFeB/MgO/CoFeB/Ta /Ru MTJ are achieved with 300 $^{\circ}$C annealing.

In the second part of the study, we epitaxially deposited well-defined $Fe_{1-x}Co_x$ (0.3 nm) single FM crystal structure. The RHEED pattern shows that the crystal structure of $Fe_{1-x}Co_x$ (0.3 nm) is independent of the Co fraction (x). Therefore, interfacial of this artificial FM structure which alters *d*-band electron occupancy without changing their crystal. We characterize the crystal and layered structure of $V/Fe/Fe_{1-x}Co_x/Pd/MgO$ using high-angle annular-dark-field scanning transmission electron microscopy (HAADF-STEM) and determine the position of the Co and Pd layers using energy-dispersive X-ray spectroscopy (EDS). We patterned the film into rectangles with dimensions of 100 × 400 μm^2. The longer edge of the rectangle is parallel to both Fe [100] and MgO [110] directions. Micro-sized antennas and intermediate gate were fabricated by a conventional microfabrication technique using electron-beam lithography and lift-off methods on the rectangular pattern. A DC bias voltage (V_{dc}) is applied between the contact pad and the intermediate gate. A bias-tee was inserted between a vector network analyzer (VNA) and antenna. Voltage-controlled magnetic anisotropy (VCMA) in an epitaxially grown $Fe/Fe_{1-x}Co_x/Pd/MgO$ system was investigated using spin-wave spectroscopy. The spin-wave resonant frequency linearly

depended on the bias voltage. The resonant-frequency shift increased with the Co fraction in $Fe_{1-x}Co_x$/Pd. We investigate the interfacial anisotropy field, the crystal anisotropy field; a voltage controlled magnetic anisotropy change and voltage controlled *interfacial* Dzyaloshinskii-Moriya interaction at single crystal $Fe_{1-x}Co_x$/Pd/MgO system. The voltage controlled magnetic anisotropy change and voltage controlled *interfacial* Dzyaloshinskii-Moriya interaction increased by approximately 300% with the increase of *x* from 0 (Fe/Pd/MgO) to 1 (Co/Pd/MgO); however, the interfacial anisotropy field varied throughout the sample up to approximately 30%. The crystal anisotropy field of the sample is 685 ±12 Oe that is similar to bulk iron. The VCMA value increases continuously with Co fraction (*x*), while VCDMI value is not continuously increasing with Co fraction (*x*). Therefore, the VCMA, the VCDMI and interfacial anisotropy energy were not directly correlated. A high VCMA of 250 fJ/Vm and VCDMI of 70 fJ/Vm were achieved in the Co/Pd/MgO region.

7.2 Conclusion

In the first part of my study, we studied voltage controlled magnetic anisotropy polycrystalline deposited system. We fabricated a magnetic tunnel junction on Ta/CoFeB/MgO/CoFeB system and annealed at different temperatures. We found that TMR and VCMA are increasing with increasing post-annealing temperature between 200 ˚C to 300 ˚C. The resistance of the MTJ layer is decreasing with increasing post-annealing temperature. The maximum VCMA and TMR of Ta/ CoFeB/ MgO sample are achieved 28 fJ/Vm and 62%, respectively with 300 ˚C annealed sample. Therefore, this work indicates that 300 ˚C annealing is a good candidate for better TMR and VCMA in Ta/CoFeB/MgO system between 200 ˚C to 300 ˚C annealing.

In the second part of my study, we studied voltage controlled magnetic anisotropy and voltage controlled *interfacial* Dzyaloshinskii-Moriya on the epitaxially deposited system. We fabricate FeCo alloy on bulk Fe that is having bcc-crystal structure. We obtained voltage controlled magnetic anisotropy and voltage controlled *interfacial* Dzyaloshinskii-Moriya interaction result that should reflect the occupancy of *d*-band electron. Such an experiment is useful not only for experimentalist but also for theoretician who needs a well-defined structure to characterize the microscopic origin of the VCMA effect. We achieved a high VCMA of 250 fJ/Vm and VCDMI of 70 fJ/Vm the Co/Pd/MgO region.

7.3 Social Impact of the Research Work

Spintronics is a rapidly emerging and immensely promising research field. It enables us to develop future technology devices by exploiting the spin of the electron. Magnetic random access memory is indispensable components of present spintronics society. A MgO-based magnetic tunnel junction (MTJ) is of great interest as a non-volatile memory because of their application in magnetic random memories and a magnetic sensor. Different successful approaches have been used to control the magnetization of MTJ, such as a current induced magnetic field and spin transfer torque. Although, these techniques still require Joule heating that remains too large to ignore. The energy consumption is a critical issue. Voltage control of magnetization direction can expect a further reduction in power consumption in MTJ. Our research is based on the development of spintronics oscillators. Here, we have observed voltage effect in poly and single-crystal 3*d* ferromagnetic metal/MgO systems using different measurement technique. It will help in designing the sputtered deposited magnetic tunnel junction with better tunnel magnetoresistance and voltage-controlled magnetic anisotropy. The epitaxially deposited Co/Pd/MgO system is providing a large value of VCMA. This result could be beneficial for the humankind.

7.4 Scope for the Future Work

A lot of possibilities are still left for the future work.

1) By changing Fe and Co composition, occupancy in *d*-band is alerted. In this study, we fabricate ultrathin Fe and Co layer at single crystalline Fe(001)/MgO(001) interface. Therefore, FeCo alloy always has bcc-structure and the obtained VCMA result should reflect the occupancy of *d*-band electron. Such an experiment is useful not only for experimentalist but also for theoretician who needs a well-defined structure to characterize the microscopic origin of the VCMA effect.

2) Proposal for practical application (Voltage controlled excitation of skyrmions)
The voltage can control perpendicular magnetic anisotropy and *interfacial*DMI. Finally, the nucleation and annihilation of skyrmion by applying an electric field in the sample is possible. It opens a way of research in spintronics society

8 Supplementary: Basic theory of magnetization dynamics

8.1 Magnetic moments

A current flowing in a loop constitutes a magnetic dipole. The magnetic dipole moment of the current in that loop is defined as the area of the loop multiplied by current flowing the loop as shown in Fig. 8.1. The direction of the magnetic dipole moment$\vec{\mu}$=I$\vec{A}$. is the perpendicular the loop plane. Its unit is Am^2. Similarly, the charge flowing in the circular path constitutes the magnetic dipole moment as shown in Fig. 8.1(b). Its magnetic dipole moment is $\vec{\mu}$=(q/T)$\vec{A}$, where T is periodic time.

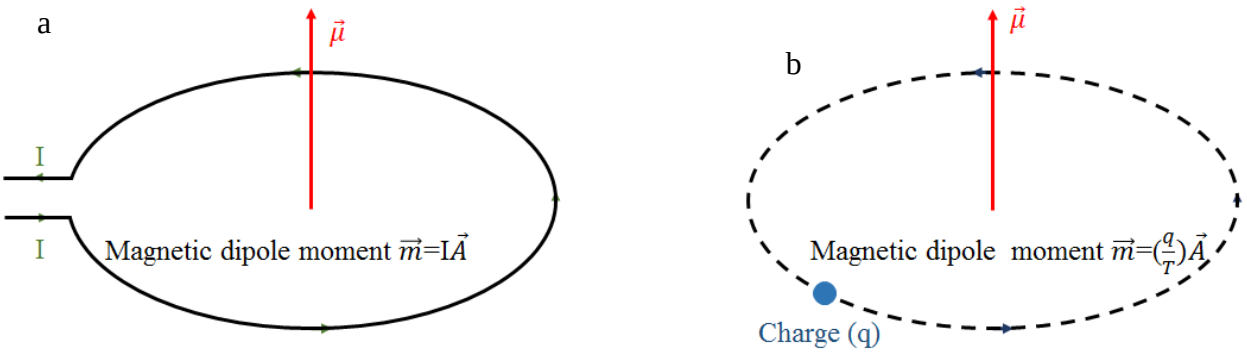

Figure 8.1. Magnetic dipole moment (a)current I in a loop. (b) circulation of charge q in a loop.

Let us consider an electron with charge *e* mass *m* revolving in a circular orbit in orbit n around the nucleus. The magnitude of the magnetic dipole moment will be given as:-$\mu = neh/4m\pi$, where *h* is plank's constant. This motion of electron is known as orbital motion and magnetic dipole moment associated with this motion is known as orbital magnetic moment. The Stern – Gerlach demonstrated that electron has another intrinsic discrete quantum mechanical magnetic moment. This discrete quantum mechanical magnetic moment is associated with electron's spin. It is analogous to spinning of rigid charge around its own central axis in classical mechanics. It is known as spin magnetic moment. Each electron is having orbital and spin magnetic moment. They

are interacting with each other that is known as spin-orbit interaction (SOI). The magnetic moment per unit volume is known as magnetization ($\overrightarrow{\mathrm{M}} = \vec{\mu}/\mathrm{V}$).

8.2 Magnetization dynamics

The magnetization of FM is a very important parameter of FM. It decides the different conductance state in MTJ. By applying voltage, we change the magnetization state of FM. The motion of magnetization fallows certain dynamics. That is called magnetization dynamics.

8.2.1 Motion equation of magnetic moment (Landau-Lifshitz equation)

According to Heisenberg equation, the time evolution of the mean value of the spin operator, $\hat{\mathrm{S}}$

$$i\hbar \frac{d}{dt}\left\langle \hat{\mathrm{S}} \right\rangle = \left\langle \left[\hat{\mathrm{S}}, \hat{\mathrm{H}}\right] \right\rangle \text{-----(1)}$$

where, $\hat{\mathrm{H}}$ represents the Hamiltonian operator of the spin system. The simplest Hamiltonian operator in a magnetic field is expressed as

$$\hat{\mathrm{H}} = -\frac{g\mu_{\mathrm{B}}}{\hbar}\hat{\mathrm{S}}.\mathrm{H}_{\mathrm{eff}} \text{ ------(2)}$$

where, g, μ_{B} and $\mathrm{H}_{\mathrm{eff}}$ are the gyromagnetic splitting factor of ferromagnetic material, Bohr magnetron and effective magnetic field of FM, respectively. We can express the right-hand side of eq$^{\mathrm{n}}$ (2.1) in the cartesian component.

$$\left[\hat{\mathrm{S}}_{\mathrm{x}}, \hat{\mathrm{H}}\right] = -\frac{g\mu_{\mathrm{B}}}{\hbar}\left[S_{\mathrm{x}}, S_{\mathrm{x}}H_{\mathrm{x}} + S_{\mathrm{y}}H_{\mathrm{y}} + S_{\mathrm{z}}H_{\mathrm{z}}\right] \text{-----(3)}$$

$$\left[\hat{\mathrm{S}}_{\mathrm{y}}, \hat{\mathrm{H}}\right] = -\frac{g\mu_{\mathrm{B}}}{\hbar}\left[S_{\mathrm{y}}, S_{\mathrm{x}}H_{\mathrm{x}} + S_{\mathrm{y}}H_{\mathrm{y}} + S_{\mathrm{z}}H_{\mathrm{z}}\right] \text{-----(4)}$$

$$\left[\hat{\mathrm{S}}_{\mathrm{z}}, \hat{\mathrm{H}}\right] = -\frac{g\mu_{\mathrm{B}}}{\hbar}\left[S_{\mathrm{z}}, S_{\mathrm{x}}H_{\mathrm{x}} + S_{\mathrm{y}}H_{\mathrm{y}} + S_{\mathrm{z}}H_{\mathrm{z}}\right] \text{-----(5)}$$

The spin operator $\hat{\mathrm{S}}$ can be expressed in the Pauli matrix. Spin operator $\mathrm{S}=\frac{\hbar}{2}\sigma$

where, ε_{abc} is the Levi-Civita symbol.

From above eq^{n} (2)−(6), eq^{n} (3)−(5) can be written as follows:

$$\left[\hat{\mathrm{S}}_{\mathrm{x}},\hat{\mathrm{H}}\right]=-\frac{g\mu_{\mathrm{B}}}{\hbar}i\hbar\left(S_{\mathrm{z}}H_{\mathrm{y}}-S_{\mathrm{y}}H_{\mathrm{z}}\right)\text{-----(7)}$$

$$\left[\hat{\mathrm{S}}_{\mathrm{y}},\hat{\mathrm{H}}\right]=-\frac{g\mu_{\mathrm{B}}}{\hbar}i\hbar\left(S_{\mathrm{x}}H_{\mathrm{z}}-S_{\mathrm{z}}H_{\mathrm{x}}\right)\text{-----(8)}$$

$$\left[\hat{\mathrm{S}}_{\mathrm{z}},\hat{\mathrm{H}}\right]=-\frac{g\mu_{\mathrm{B}}}{\hbar}i\hbar\left(S_{\mathrm{y}}H_{\mathrm{x}}-S_{\mathrm{y}}H_{\mathrm{x}}\right)\text{-----(9)}$$

From eq^{n} (3), (7), (8), and (9)

$$\frac{d}{dt}\left\langle\hat{\mathrm{S}}\right\rangle=-\frac{g\mu_{\mathrm{B}}}{\hbar}\left\langle\left[\hat{\mathrm{S}}\times\vec{\mathrm{H}}_{\mathrm{eff}}\right]\right\rangle\text{-----(10)}$$

The angular momentum by an electron is related to its magnetic momentum through its spin:

$$\vec{\mathrm{M}}=\gamma\left\langle\hat{\mathrm{S}}\right\rangle\text{-------(11)}$$

where $\gamma=\frac{g\mu_{\mathrm{B}}}{\hbar}$ is the gyromagnetic ratio. The eq^{n} (11) can be rewritten as

$$\frac{d}{dt}\vec{\mathrm{M}}=-\gamma\vec{\mathrm{M}}\times\vec{\mathrm{H}}_{\mathrm{eff}}\text{-----(12)}$$

This equation controls the precessional motion of magnetic moment around a magnetic field. It is called the Landau-Lifshitz equation.

8.2.2 Introduction of damping (Landau-Lifshitz-Gilbert equation)

The precession motion of magnetization $\vec{M}$ in the effective magnetic field $\vec{H}_{eff}$.

$$\frac{d}{dt}\vec{M} = -\gamma\vec{M}\times\vec{H}_{eff} + \alpha\frac{\vec{M}}{M_s}\times\frac{d}{dt}\vec{M} \text{-------(13)}$$

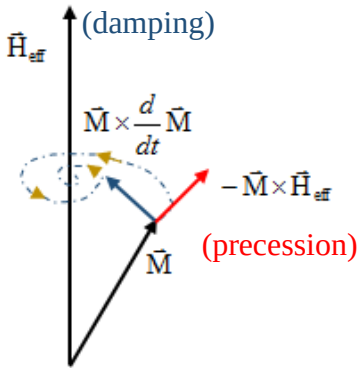

Figure 8.2. Damped precession motion

Where α and M_s are the damping and saturation magnetization, respectively. The second term provides damping term. The LLG equation indicates that when magnetization $\vec{M}$ appears the effective magnetic field $\vec{H}_{eff}$. The magnetization $\vec{M}$ starts precession around the effective magnetic field $\vec{H}_{eff}$ and a perpendicular gilbert damping term is applied perpendicular to precession path. It tries to align the magnetization $\vec{M}$ the with the effective magnetic field.

8.3 Ferromagnetic energies

The potential energy of ferromagnetic material magnetization is defined as $U=-\int_{ref}^{final}\vec{H}(r)\vec{M}(r)dV$. Where $\vec{H}$ represents the applied magnetic field. There are various parameters that influences the $\vec{M}$ inside the ferromagnetic material.

Initially, the magnetization of the domain in FM is aligned in a certain direction. It is called minimum energy state (stable state). When the FM appears in the magnetic field, the magnetization starts precession around the effective magnetic field and tries to align with the effective magnetic field. That is called the potential energy of FM. The potential energy of ferromagnetic material magnetization is defined as work done external magnetic force rotating the magnetization from the reference position to an arbitrary position. $U=\int_{ref}^{final}\vec{M}.\overrightarrow{dH}$. Where $\vec{H}$ represents the effective magnetic field. There are various parameters that influences the $\vec{M}$ inside the ferromagnetic material. Work done external agent for changing the magnetization from easy axis to hard axis

$$E = -\int\vec{M}(r)\vec{H}_{eff}(r)dV$$

$E=E_{zee}+E_{ex}+E_{DMI}+E_{an}+E_{dem}+\ldots\ldots$ ----------(14)

A ferromagnetic material can be understood at the different level of complexity. The ferromagnetic energy of thin film ferromagnetic material can be understood with the different component term, Zeeman energy, exchange interaction energy, Dzyaloshinskii-Moriya interaction(DMI), anisotropy energy and dipolar energy terms. The magnetic system tries to align the magnetization $\vec{M}(r)$ in effective magnetic field ($\vec{\mathrm{H}}_{\mathrm{eff}}$) direction.

$$\vec{\mathrm{H}}_{eff}(r) = -\frac{\delta E}{\delta \vec{\mathrm{M}}} \text{ ----------(15)}$$

The eq^{n} (2.15) can be written as

$$\vec{\mathrm{H}}_{eff} = \vec{\mathrm{H}}_{ext} + \vec{\mathrm{H}}_{ex} + \vec{\mathrm{H}}_{DMI} + \vec{\mathrm{H}}_{an} + \vec{\mathrm{H}}_{dem} + \text{.....----------(16)}$$

8.3.1 Zeeman Energy

The interaction between the magnetization $\vec{\mathrm{M}}$ & external magnetic field $\vec{\mathrm{H}}_{ext}$ is described as energy density $E_{zee} = -\vec{\mathrm{M}} \cdot \vec{\mathrm{H}}_{ext}$. It is helpful in aligning of magnetization parallel to the applied external field.

8.3.2 Exchange Energy

The exchange interaction is the basic phenomenon in ferromagnetic materials. Its origin is quantum mechanical, based on Coulomb interaction and the Pauli exclusion principle.

The interaction between spins: $\mathrm{U}(S_1, S_1) = (S_1^x, S_1^y, S_1^z)(A^{ij})\begin{pmatrix} S_1^x \\ S_1^y \\ S_1^z \end{pmatrix}$ ----------(17)

Matrix (A) can be described as the sum of symmetric and antisymmetric part.
$A = \frac{1}{2}(A + A^T) + \frac{1}{2}(A - A^T) = A_s + A_{as}$ ----------(18)

Symmetric part of eq^{n} (18), can be diagonalized by a certain rotation, then

$$A_s = \begin{pmatrix} J^x & 0 & 0 \\ 0 & J^y & 0 \\ 0 & 0 & J^z \end{pmatrix} \text{----------(19)}$$

If the medium is isotropic, then eq^n (19) can be written as,

$$A_s = J\begin{pmatrix} 1 & 0 & 0 \\ 0 & 1 & 0 \\ 0 & 0 & 1 \end{pmatrix} \text{----------(20)}$$

Often we can write symmetrical part of From eq^n (17), $E_{\text{ex}}(S_{1,}S_1) = -j\vec{S}_{1,}\cdot\vec{S}_2$ ----------(21)

The symmetric exchange energy (Eq^n (21) is generally called as exchange energy. Because of this, two electrons with spin vector S_1 and $S_{2.}$are having different energies in the parallel and antiparallel alignment of their spin and j>0 for a ferromagnetic material and j< 0 for an antiferromagnetic material. Therefore, the configuration with parallel spins is the lowest in energy.

If the eq^n (21) is applied to solids in the Heisenberg model having "N" atoms, the total energy of the system is defined as [25]

$$E_{\text{ex}} = -\sum_{l,m}^{N} j_{l,m}\vec{S}_{l,}\cdot\vec{S}_m \text{----------(22)}$$

This summation is sometimes limited to short-range. Despite this, it constituted of wide regions of uniform magnetization that is called magnetic domains in ferromagnetic material.

8.4 Dzyaloshinskii-Moriya energy

Asymmetric part of the eq^n (18) has a skew property; it can not have altered by the rotation as

$$A_{as} = \begin{pmatrix} 0 & D^x & -D^y \\ -D^z & 0 & D^x \\ D^y & -D^x & 0 \end{pmatrix} \text{----------(23)}$$

By inserting eq^n (23) in the eq^n (17), asymmetric part of exchange energy (eq^n (17)). It is the first time observed by Dzyaloshinskii and Moriya. It is Dzyaloshinskii−Moriya interaction (DMI).

$$\text{E}_{\text{DMI}} = (S_1^x, S_1^y, S_1^z)\begin{pmatrix} 0 & D^x & -D^y \\ -D^z & 0 & D^x \\ D^y & -D^x & 0 \end{pmatrix}\begin{pmatrix} S_1^x \\ S_1^y \\ S_1^z \end{pmatrix} = \vec{D}_{12}\cdot(\vec{S}_1\times\vec{S}_2) \text{----------(24)}$$

where, $\vec{D}_{12}$ is the Dzyalsinskii−Moriya vector. It is perpendicular to asymmetry direction and the vector $\vec{r}_{12}$ between the spins $\vec{S}_1$ and $\vec{S}_2$. The Dzyalsinskii−Moriya interaction (DMI) is induced because of the lack or breaking of inversion symmetry in lattices and at the interface of magnetic films, respectively For the ultrathin magnetic film, interfacial DMI have been predicted where two atomic the spins $\vec{S}_1$ and $\vec{S}_2$ with a neighboring atom having a large spin-orbit coupling.

8.5 Magnetic Anisotropy Energy

In magnetic material, the energy depends on the direction of magnetization. It is called magnetic anisotropy energy. There is the different origin of magnetic anisotropy such as crystal symmetry shape, stress, or directed atomic pair ordering.

8.5.1 Magnetic crystal anisotropy

However, in the long extended sample, the energy is not isotopic because of spin-orbit interaction: the spin is coupled to the orbital momentum, whose is connected with the electrostatic potential of the crystal lattice. Therefore, spin-orbit interaction tries to couple with the symmetry of the crystal lattice.

The magnetic crystal anisotropy energy density in a cubic crystal can be shown as

$$E = K_1(m_x^2 m_y^2 + m_y^2 m_z^2 + m_z^2 m_x^2) + K_2(m_x^2 m_y^2 m_z^2) \text{ ---------(25)}$$

where, the K_1 (K_2) is the volume anisotropy of first (second) order and m_i is the components of the normalized magnetization to the cubic axes of the lattice. The experimental anisotropy constants at room temperature for *iron* are

K_1=4.8×10^4 and K2=-1.0×10^4 J/m^3

The crystalline anisotropy field of Fe =2 K_1/ M_s =600 Oe.

and for *nikel*

K_1=-4.8×10^3 and K2=-2.3×10^3 J/m^3

The uniaxial crystalline anisotropy energy density is expressed as

$$E_{\text{uni}} = -K_{\text{u}}^{1} m_x^2 + K_{\text{u}}^{2} m_x^4 + ... \text{---------(26)}$$

where, the $K_{\text{u}}^{1}(K_{\text{u}}^{2})$ is the volume anisotropy of first (second) order and for *cobalt*

K_{u}^{1} =4.1×10^5 and 1.5×10^5 J/m^3

Translation symmetry along the film thickness is broken, generates the magnetic interfacial anisotropy in the thin ferromagnetic material. This anisotropy is different from bulk anisotropy. If the film thickness is lesser than the static exchange correlation length, the interfacial magnetization can be assumed to be homogeneous across the film. The interfacial magnetic anisotropy is described as $E_{\text{int}} = -\frac{K_{\text{s}}}{t_{\text{FM}}} m_z^2$ -------(27)

where, t_{FM} is the film thickness. The *z*-axis is defined as symmetry breaking direction. The perpendicular component of the electric field influences the *d*-band electron of interfacial FM. That *d*-band electron influences the interfacial magnetic anisotropy. That is called a voltage-controlled interfacial anisotropy change (VCMA).

8.5.2 Magnetic shape anisotropy

It is one of the most important sources of anisotropy in a thin film. The fringing magnetic field i.e., called demagnetization magnetic field is generated because of the shape of the ferromagnetic material. This demagnetization magnetic field interacts with a magnetic moment. This energy is called demagnetization field energy or magnetic shape anisotropy. It is defined as

$$E_{dem} = -\vec{M}.\vec{H}_{\text{dem}} \text{ ---------(28)}$$

The demagnetizing field $\vec{H}_{\text{dem}}$ created by the ferromagnetic film can be described by Maxwell's equation

$$\nabla\vec{B} = \nabla\mu_0(\vec{H}_{\text{dem}} + \vec{M}) = 0 \text{ ---------(29)}$$

$$\nabla\vec{H}_{\text{dem}} = -\nabla\vec{M} \text{ ---------(30)}$$

From eq$^{\text{n}}$ (30),

$$\vec{H}_{\text{dem}} = -\bar{N}\vec{M} \text{ ---------(31)}$$

Is the magnetic field that is generated by the divergence of magnetization, $\overline{N}$ is the demagnetization tensor. It is described as

$$\overline{N} = \begin{pmatrix} N_x & 0 & 0 \\ 0 & N_y & 0 \\ 0 & 0 & N_z \end{pmatrix} \text{---------(32)}$$

where, $N_x + N_y + N_z = 1$---------(33)

Generally, calculation of $\overline{N}$ is complicated, however, an ellipsoid of ultrathin film ferromagnetic material with z-axis pointing perpendicular to the film plane is having $N_x, N_y = 0, N_z = 1.$

Then demagnetization field from the eq^n (31) and Nz=1, $\vec{H}_{dem} = -M_s\hat{k}$ ---------(34)

The demagnetization energy density the eq^n (28) and the eq^n (34)

$E_{dem} = \vec{M}.\overline{N}\vec{M}$ ---------(35)

the eq^n (35) can be written as

$$E_{dem} = \frac{1}{2}\mu_0 M_s^2 \text{---------(36)}$$

.

References

1. M. N. Baibich, J. M. Broto, A. Fert, F. Nguyen Van Dau, F. Petroff, P. Eti- enne, G. Creuzet, A. Friederich and J. Chazelas, Giant magnetoresistance of Fe(001)/Cr(001) superlattices, Phys. Rev. Lett. 61, 2472-2475 (1988).
2. G. Binasch, P. Grunberg, F. Saurenbach and W. Zinn, Enhanced magnetore- sistance in layered magnetic structures with antiferromagnetic interlayer ex- change, Phys. Rev. B 39, 4828-4830 (1989).
3. M. Julliere, Tunneling between ferromagnetic films, Phys. Lett. A 54, 225-226 (1975).
4. D. Wang, C. Nordman, J. M. Daughton, Z. Qian, J. Fink, 70% TMR at room temperature for SDT sandwich junctions with CoFeB as free and reference lay- ers, IEEE Trans. Magn. 40, 2269–2271 (2004).
5. S. S. P. Parkin, K. P. Roche, M. G. Samant, P. M. Rice, R. B. Beyers, R. E. Scheuerlein, E. J. O'Sullivan, S. L. Brown, J. Bucchigano, D. W. Abraham, Y. Lu, M. Rooks, P. L. Trouilloud, R. A. Wanner, W. J. Gallagher, Exchange- biased magnetic tunnel junctions and application to nonvolatile magnetic ran- dom access memory, J. Appl. Phys. 85, 5828-5833 (1999).
6. Shinji Yuasa, Tunneling Magnetoresistance: Experiment (MgO Magnetic Tun- nel Junctions), Handbook of Spin Transport and Magnetism, Taylor and Francis (2012).
7. S. Maekawa and O. Gafvert, Electron tunneling between ferromagnetic films, IEEE Trans. Magn. Mag. 18, 707-708 (1982).
8. M. Johnson and R. H. Silsbee, Interfacial charge-spin coupling: Injection and detection of spin magnetization in metals, Phys. Rev. Lett. 55, 1790-1793 (1985).
9. S. Datta and B. Das, Electronics analog of the electro-optic modulator, Appl. Phy. Lett. 56, 665-667 (1990).
10. John Schliemann, J. Carlos Egues, and Daniel Loss, Nonballistic Spin-Field- Effect Transistor, Phys. Rev. Lett. 90, 146801-1- 4 (2003).
11. E. Johnston-Halperin, D. Lofgreen, R. K. Kawakami, D. K. Young, L. Col- dren, A. C. Gossard, D. D. Awschalom, Spin-polarized Zener tunneling in (Ga,Mn)As, Phys. Rev. B 65, 041306-1-4 (2002).
12. M. E. Flatt´e. and G. Vignale, Unipolar spin diodes and transistors, Appl. Phys. Lett. 78,

1273-1275 (2001).
13. Francesco Giazotto, Fabio Taddei, Rosario Fazio, Fabio Beltram, Ferromag- netic resonant tunneling diodes as spin polarimeters, Appl. Phys. Lett. 82, 2449- 2451 (2003).
14. T. Koga, J. Nitta, S. Datta, H. Takayanagi, Spin-filter device based on the Rashba Effect using a monmagnetic resonant tunneling diode, Phys. Rev. Lett. 88, 126601-1- 4 (2002).
15. A. Slobodskyy, C. Gould, T. Slobodskyy, C. R. Becker, G. Schmidt, L.W. Molenkamp, Voltage-controlled spin selection in a magnetic resonant tunnel- ing diode, Phys. Rev. Lett. 90, 246601-1- 4 (2003).
16. A. Fert, Historical Overview: From Electron Transport in Magnetic Materials to Spintronics, Handbook of Spin Transport and Magnetism, p. 1-14, Taylor and Francis (2011).
17. W. Wulfhekel, M. Klaua, D. Ullmann, F. Zavaliche, J. Kirschner, R. Urban, T. Monchesky, B. Heinrich, Single-crystal magnetotunnel junctions, Appl. Phys. Lett. 78, 509-511 (2001).
18. M. Bowen, V. Cros, F. Petroff, A. Fert, C. Martínez Boubeta, J. L. Costa- Krämer, J. V. Anguita, A. Cebollada, F. Briones, J. M. de Teresa, L. Morel- lón, M. R. Ibarra, F. Güell, F. Peiró, A. Cornet, Large magnetoresistance in Fe/MgO/FeCo(001) epitaxial tunnel junctions on GaAs(001), Appl. Phys. Lett. 79, 1655–1657 (2001).
19. S. Yuasa, T. Nagahama, K. Fukushima, Y. Suzuki, K. Ando, Giant room- temperature magnetoresistance in single-crystal Fe/MgO/Fe magnetic tunnel junctions, Nat. Mater. 3, 868–871 (2004).
20. S. S. P. Parkin, C. Kaiser, A. Panchula A. Panchula, P. M. Rice, B. Hughes, M. Sawant, S. -H. Yang, Giant tunnelling magnetoresistance at room temperature with MgO (100) tunnel barriers, Nat. Mater. 3, 862–867 (2004).
21. J.Hayakawa,S.Ikeda,Y.M.Lee,F.Matsukura,H.Ohno,Effectofhighanneal- ing temperature on giant tunnel magnetoresistance ratio of CoFeB/MgO/CoFeB magnetic tunnel junctions, Appl. Phys. Lett. 89, 232510-1-3 (2006).
22. H. Naganuma, L. Jiang, M. Oogane, Y. Ando, Retraction: “Large Tunnel Mag- netoresistance of 1056% at Room Temperature in MgO Based Double Barrier Magnetic Tunnel Junction”, Appl. Phys. Express 4, 019201 (2011) and Appl. Phys. Express 2, 083002-1-3 (2009).
23. D. D. Djayaprawira, K. Tsunekawa, M. Nagai, H. Maehara, S. Yamagata, N. Watanabe, 230% room-temperature magnetoresistance in CoFeB/MgO/CoFeB magnetic tunnel junctions, Appl. Phys. Lett. 86, 092502-1-3 (2005).
24. S. Ikeda, J. Hayakawa, Y. Ashizawa, Y. M. Lee, K. Miura, H. Hasegawa, M. Tsunoda, F. Matsukura, H. Ohno, Tunnel magnetoresistance of 604% at 300 K by suppression of Ta

diffusion in CoFeB/MgO/CoFeB pseudo-spin-valves annealed at high temperature, Appl. Phys. Lett. 93, 082508-1-3 (2008).
25. J. C. Slonczewski: J. Magn. Magn. Mater. 159 (1996) L1
26. L. Berger: Phys. Rev. B **54**, 9353 (1996).
27. K. Nakamura, R. Shimabukuro, Y. Fujiwara, T. Akiyama, T. Ito, and A. J. Freeman, Phys. Rev. Lett. **102**, 187201 (2009).
28. M. Weisheit, S. Fähler, A. Marty, Y. Souche, C. Poinsignon, and D. Givord, Science **315**, 349 (2007).
29. T. Maruyama, Y. Shiota, T. Nozaki, K. Ohta, N. Toda, M. Mizuguchi, A. Tulapurkar, T. Shinjo, M. Shiraishi, S. Mizukami, Y. Ando, Y. Suzuki, Nat. Nanotechnol. **4**, 158 (2009).
30. Uwe Bauer et al., Nat. Mater. 4134, (2014)
31. Kawabe, T *et al.* Electric-field-induced changes of magnetic moments and magnetocrystalline anisotropy in ultrathin cobalt films *Phys. Rev. B.* **96,** 220412 (2017).
32. 74Miwa, S. *et al.* Voltage controlled interfacial magnetism through platinum orbits. *Nat. Commun.* **8,** 15848 (2017).
33. S. Yuasa, T. Nagahama, A. Fukushima, Y. Suzuki, and K. Ando, Nature Mater. **3**, 868 (2004)
34. S. S. P. Parkin, C. Kaiser, A. Panchula, P. M. Rice, B. Hughes, M. Samant, and S.-H. Yang, Nat. Mater.**3**, 862 (2004).
35. C.-G. Duan, J. P. Velev, R. F. Sabirianov, Z. Zhu, J. Chu, S. S. Jaswal, and E. Y. Tsymbal, Phys. Rev. Lett. **101**, 137201 (2008).
36. M. Tsujilawa, and T. Oda, Phys. Rev. Lett. **102**, 247203 (2009).
37. Shiota, Y. *et al. Induction of coherent magnetization switching in a few atomic layers of FeCo using voltage pulses*. *Nat. Mater.* **11,** 39 (2012).
38. W. Skowroński , T. Nozaki , D. D. Lam , Y. Shiota , K. Yakushiji , H. Kubota , A. Fukushima , S. Yuasa , and Y. Suzuki , Phys. Rev. B **91**(18), 184410 (2015).
39. V. Novosad, Y. Otani, A. Ohsawa, S. G. Kim, K. Fukamichi, J. Koike, K.Maruyama, O. Kitakami, and Y. Shimada: J. Appl. Phys. **87,** 6400 (2000).
40. M. Overby, A. Chernyshov, L. P. Rokhinson, X. Liu, and J. K. Furdyna:Appl. Phys. Lett. **92**, 192501 (2008)

41. D. Chiba, M. Sawicki, Y. Nishitani, Y. Nakatani, F. Matsukura, and H.Ohno: Nature **455**, 515 (2008).
42. W. Eerenstein, N. D. Mathur, and J. F. Scott: Nature **442**, 759 (2006).
43. M. Saito, K. Ishikawa, S. Konno, K. Taniguchi, and T. Arima: Nat. Mater.8 (2009)z 634.
44. P. Borisov, A. Hochstrat, X. Chen, W. Kleemann, and C. Binek: Phys. Rev.Lett. **94**, 117203 (2005).
45. Y.-H. Chu, L. W. Martin, M. B. Holcomb, M. Gajek, S.-J. Han, Q. He, N.Balke, C.-H. Yang, D. Lee, W. Hu, Q. Zhan, P.-L. Yang, A. Fraile Rodriguez,A. Scholl, S. X. Wang, and R. Ramesh: Nat. Mater. **7**, 478 (2008).
46. C.-G. Duan, J. P. Velev, R. F. Sabirianov, W. N. Mei, S. S. Jaswal, andE. Y. Tsymbal: Appl. Phys. Lett. **92**, 122905 (2008)
47. S. Sahoo, S. Polisetty, C.-G. Duan, S. S. Jaswal, E. Y. Tsymbal, and C. Binek: Phys. Rev. B **76**, 092108 (2007).
48. L. Gerhard, T. K. Yamada, T. Balashov, A. F. Takacs, R. J. H. Wesselink, M. Dane, M. Fechner, S. Ostanin, A. Ernst, I. Mertig, and W. Wulfhekel:Nat. Nanotechnol. **5**, 792 (2010).
49. D. Chiba, S. Fukami, K. Shimamura, N. Ishiwata, K. Kobayashi, and T. Ono, Nat. Mater. **10**, 853 (2011).
50. M. Oba, K. Nakamura, T. Akiyama, T. Ito, M. Weinert, and A. J. Freeman, Phys. Rev. Lett. **114**, 107202 (2015).
51. P. Borisov, A. Hoschstrat, X. Chen, W. Kleemann, and C. Binek, Phys. Rev. Lett. **94**, 117203 (2005).
52. K. Nawaoka, S. Miwa, Y. Shiota, N. Mizuochi, and Y. Suzuki, Appl. Phys. Express **8**, 063004 (2015).
53. F. Ando, H. Kakizakai, T. Koyama, K. Yamada, M. Kawaguchi, S. Kim,K.-J. Kim, T. Moriyama, D. Chiba, and T. Ono, Appl. Phys. Lett. **109**, 022401 (2016).
54. T. Dohi, S. Kanai, A. Okada, F. Matsukura, and H. Ohno, AIP Adv. **6**, 075017 (2016).
55. T. Dohi, S. Kanai, F.Matsukura, and H. Ohno, Appl. Phys. Lett. **111**, 027403 (2017).
56. Y. Shiota, T. Nozaki, F. Bonell, S. Murakami, T. Shinjo, and Y. Suzuki, Nat. Mater. **11**, 39 (2012).

57. S. Kanai, M. Yamanouchi, S. Ikeda, Y. Nakatani, F. Matsukura, and H. Ohno, Appl. Phys. Lett. **101**, 122403 (2012).
58. C. Grezes, F. Ebrahimi, J. G. Alzate, X. Cai, J. A. Katine, J. Langer, B. Ocker, P. K. Amiri, and K. L. Wang, Appl. Phys. Lett. **108**, 012403 (2016).
59. Y. Shiota, T. Nozaki, S. Tamaru, K. Yakushiji, H. Kubota, A. Fukushima, S. Yuasa, and Y. Suzuki, Appl. Phys. Lett. **111**, 022408 (2017).
60. D. D. Djayaprawira, K. Tsunekawa, M. Nagai, H. Maehara, S. Yamagata, N. Watanabe, S. Yuasa, Y. Suzuki, and K. Ando, Appl. Phys. Lett.**86**, 092502 (2005).
61. Duan, C.-G. et al. Surface magnetoelectric effect in ferromagnetic metal films. Phys. Rev. Lett. **101,** 137201 (2008).
62. Tsujikawa, M. & Oda, T. Finite electric field effects in the large perpendicular magnetic anisotropy surface Pt/Fe/Pt(001): A first-principles study. Phys. Rev. Lett. **102,** 247203 (2009).
63. Nakamura, K. *et al.* Giant modification of the magnetocrystalline anisotropy in transition-metal monolayers by an external electric field. Phys. Rev. Lett. **102,** 187201 (2009).
64. Chiba, D. *et al.* Electrical control of the ferromagnetic phase transition in cobalt at room temperature. Nat. Mater. **10,** 853–856 (2011).
65. *Oba, M. et al.* Electric-field-induced modification of the magnon energy, exchange interaction, and Curie temperature of transition-metal thin films. Phys. Rev. Lett. **114,** 107202 (2015).
66. Borisov, P., Hochstrat, A., Chen, X., Kleemann, W. & Binek, Ch. Magnetoelectric switching of exchange bias. Phys. Rev. Lett. **94,** 117203 (2005).
67. Nawaoka, K., Miwa, S., Shiota, Y., Mizuochi, N. & Suzuki, Y. Voltage induction of interfacial Dzyaloshinskii–Moriya interaction in Au/Fe/MgO artificial multilayer. *Appl. Phys. Exp*. **8,** 063004 (2015).
68. Ando, F. *et al.* Modulation of the magnetic domain size induced by an electric field. *Appl. Phys. Lett.* **109,** 022401, (2016).
69. Dohi, T. Kanai, S. Okada, A. Matsukura, F. and Ohno, H. Effect of electric-field modulation of magnetic parameters on domain structure in MgO/CoFeB, *AIP Advances* **6,** 075017 (2016).

70. Dohi, T. Kanai, S. Matsukura, F. and Ohno, H. Electric-field effect on spin-wave resonance in a nanoscale CoFeB/MgO magnetic tunnel junction *Appl. Phys. Lett.* **111,** 027403 (2017).
71. Kanai, S. *et al*. Electric field-induced magnetization reversal in a perpendicular-anisotropy CoFeB-MgO magnetic tunnel junction. *Appl. Phys. Lett.* **101,** 122403, (2012).
72. Grezes, C. *et al.* Ultra-low switching energy and scaling in electric-field-controlled nanoscale magnetic tunnel junctions with high resistance-area product. *Appl. Phys. Lett.* **108,** 012403 (2016).
73. Shiota, Y *et al.* Reduction in write error rate of voltage-driven dynamic magnetization switching by improving thermal stability factor. *Appl. Phys. Lett.* **111,** 022408 (2017).
74. Bonell, F.*et al.* Large change in perpendicular magnetic anisotropy induced by an electric field in FePd ultrathin films. *Appl. Phys. Lett.* **98,** 232510 (2011).
75. Hibino, Y. *et al.* Electric-field modulation of magnetic anisotropy in perpendicularly magnetized Pt/Co structure with a Pd top layer. *Appl. Phys. Express* **8,** 113002 (2015).
76. Hibino, Y. *et al.* Peculiar temperature dependence of electric-field effect on magnetic anisotropy in Co/Pd/MgO system. *Appl. Phys. Lett.* **109,** 082403 (2016).
77. Bonell, F. et al. Reversible change in the oxidation state and magnetic circular dichroism of Fe driven by an electric field at the FeCo/MgO interface. Appl. Phys. Lett. **102,** 152401 (2013).
78. Bi, C. *et al*. Reversible control of Co magnetism by voltage-induced oxidation. Phys. Rev. Lett. **113,** 267202 (2014).
79. Bauer, U. *et al*. Magneto–ionic control of interfacial magnetism. Nat. Mater. **14,** 174–181 (2015).

Acknowledgment

My time at Osaka University has undoubtedly been a life-changing experience. Sure, I learned a lot about research and spintronics. Much of the work presented in this thesis would never have materialized but for the support, advice, contribution and companionship that I got from so many people. This thesis would not have been complete without a mention of all those who have affected my graduate life in so many ways.

First and foremost, I would like to heartily thanks Prof. Suzuki sensei for the opportunity to work with him and his group. His door was always comforting to me. He has also been a great source of knowledge and information when I encountered difficulties in my research. I would like thanks to Prof. Goto sensei. He helped in every aspect of my research life. I would like thanks Prof. Miwa who helped me with research. I would like thanks Prof. Tamura who taught me quantum mechanics and spintronics in the very easy way.

There is a long list of people that I am indebted. I started work with my group. I would like to thank my group Cho-san, Hatanaka san, Nawaoka-san and lab group members for their many insightful discussion, open attitudes fun times, support and encouragement. Many time cross question with Cho-san and Prof. Tamura-sensei made me go through the basic, which helped me a lot. I would like thanks Hasegawa san, Oda-san and Honke-san for continuous support in official documents support. I especially thank Prof. Suzuki and Prof. Goto, who patiently offered me help and guidance. Some of my thanks to my friends who always helped me in even and odd situations.

I can never say enough about how I appreciate the support from my family. They have brought so much love and happiness into my life and made it joyful and complete.

Thanks to all of you.

Publication and Conferences

List of Publications

Name written in bold letter represents thesis author

① Authors, ② Tittle, ③ Journal, ④ Vol., No.,pp-, and Years

1. ① Sourabh Jain, Himanshu Sharma, **Amit Kumar Shukla**, C. V. Tomy, Vaijayanti R. Palkar, Ashwin Tulapurkar.
   ② Optimization of La0.7Sr0.3MnO3 thin film by pulsed laser deposition for spin injection
   ③ Physica B
   ④ 448, 103 (2014).

2. ① Arnab Bose, **Amit Kumar Shukla**, Katsunori Konishi, Sourabh Jain, Nagarjuna Asam, Swapnil Bhuktare, Hanuman Singh, Duc Duong Lam2 , Yuya Fujii, Shinji Miwa, Yoshishige Suzuki, and Ashwin A. Tulapurkar**.**
   ② Observation of thermally driven field-like spin torque in magnetic tunnel junctions
   ③ Appl. Phys. Lett.
   ④ 109, 032406 (2016)

3. ① Bart F. Vermeulen, Jackson Wu, Johan Swerts, Sebastien Couet, Iuliana P Radu, Guido Groeseneken, Christophe Detavernier, Johanna Jochum, Margriet Van Bael, Kristiaan Temst, **Amit Shukla,** Shinji Miwa, Yoshishige Suzuki, and Koen Martens**.**
   ② Perpendicular Magnetic Anisotropy of CoFeB\Ta Bilayers on ALD HfO2
   ③ AIP Advances
   ④ 7, 055933 (2017).
4. ① **Amit Kumar Shukla**, Minori Goto, Xiandong Xu, Kohei Nawaoka, Joko Suwardy, Tadakatsu Ohkubo, Kazuhiro Hono, Shinji Miwa, and Yoshishige Suzuki.

② Voltage-Controlled Magnetic Anisotropy in $Fe_{1-x}Co_x$/Pd/MgO system

③ Scientific Reports

④ Published on 9th July 2018

Oral Presentation

(① Authors, ② Tittle, ③ Journal, ④ Place, Number, Date)

1. ① Amit Kumar Shukla, Minori Goto, Kohei Nawaoka, Joko Suwardy, Shinji Miwa, and Yoshishige Suzuki.

   ② Voltage Controlled Magnetic Anisotropy at Fe1-xCoxPd/MgO Interface

   ③ International Conference Solid State Devices and Materials"

   ④ on 22nd September 2017.

Poster Presentations

2. (① Authors, ② Tittle, ③ Journal, ④ Place, Number, Date)

5. ① **Amit Kumar Shukla**, Minori Goto , Shinji Miwa , Shohei Hatanaka, Kohei Nawaoka, Ashwin A.Tulapurkar, N. Mizuochii, and Yoshishige Suzuki, **,**

   ② Fabrication of MgO based Magnetic Tunnel Junctions (MTJ)

   ③ KoreaJapan Spin-orbit workshop

   ④ Dec-2015.

6. ① Arnab Bose, **Amit Kumar Shukla**, Katsunori Konishi, Sourabh Jain, Nagarjuna Asam, Swapnil Bhuktare, Hanuman Bana, Duong Duc Lam, Yuya Fujii, Shinji Miwa, Yoshishige Suzuki, Ashwin A. Tulapurkar,

   ② Thermally driven spin torque in magnetic tunnel junctions

   ③ Intermag conference

   ④ 2015

7. ① **Amit Kumar Shukla**, Minori Goto, Kohei Nawaoka , Shinji Miwa and Yoshishige Suzuki ,

② Voltage Controlled Magnetic Anisotropy (VCMA) Change in Different Temperature Annealed Magnetic Tunnel Junctions (MTJ)

③ Japan Society of Applied Physics (JSAP)

④ 13-16th September 2016.

8. ① **Amit Kumar Shukla**, Minori Goto, Shohei Hatanaka, Kohei Nawaoka, Shinji Miwa, and Yoshishige Suzuki,

   ② Voltage Controlled Magnetic Anisotropy (VCMA) in Ta/CoFeB/MgO at Different Annealing Temperatures

   ③ International Conference on Emerging Electronics (ICEE)

   ④ 27th Dec 2016.

9. ① **Amit Kumar Shukla**, Minori Goto, Kohei Nawaoka, Joko Suwardy, Shinji Miwa, and Yoshishige Suzuki,

   ② Electric field effect on magnetic anisotropy at Fe1−xCoxPd/MgO interface

   ③ The 3rd ImPACT International Symposium on Spintronics Memory, Circuit and Storage.

   ④ 23-25th September 2017.

   Best poster award